Advanced Materials for Water Treatment

Wu Yuchen

Thesis submitted to the University of Ottawa
in partial Fulfillment of the requirements for the
Doctorate in Philosophy in Chemical Engineering

Department of Chemical and Biological Engineering
Faculty of Engineering
University of Ottawa

Examining Committee Membership

The following served on the Examining Committee for this thesis. The decision of the Examining Committee is by majority vote.

External Examiner	Ajay Ray University of Western Ontario
Internal Examiners	André Tremblay
	Christopher Lan
	Benoit Lessard
Supervisors	Prof. Zisheng Zhang University of Ottawa
	Prof. Zhongwei Chen University of Waterloo

AUTHOR'S DECLARATION

This thesis consists of material all of which I authored or co-authored: see Statement of Contributions included in the thesis. This is a true copy of the thesis, including any required final revisions, as accepted by my examiners.

I understand that my thesis may be made electronically available to the public.

Statement of Contributions

This thesis comprises contents of published work.

Yuchen Wu, Gaopeng Jiang, Zachary P. Cano, Guihua Liu, Wenwen Liu, Kun Feng, Gregory Lui, Zisheng Zhang*, and Zhongwei Chen* *"Highly Efficient Removal of Suspended Solid Pollutants from Wastewater by Magnetic Fe_3O_4-Graphene Oxides Nanocomposite"*. ChemistrySelect 2018, 3, 11643– 11648.

Yuchen Wu, Gaopeng Jiang, Guihua Liu, Zachary P. Cano, Zhen Zhang, Qian Li, Zisheng Zhang*, Aiping Yu *and Zhongwei Chen* *"A 3D ordered hierarchically porous non-carbonelectrode for highly effective and efficient capacitive deionization"*. Journal of Materials Chemistry A, 2019, 7, 15633–15639.

Yuchen Wu, Gaopeng Jiang, Qian Li, Zisheng Zhang* and Zhongwei Chen*. "*N-doped reduced graphene oxide-TiO_xN_y electrode for highly and efficient capacitive deionization*" RSC Adv., 2019, 9, 28186-28193.

For the above papers, Yuchen Wu, the first author, contributed to all the experiments and manuscript writing. Gaopeng Jiang, and Zachary P. Cano contributed to manuscript revising and language editing. Other authors contributed to some experimental support and management. Zisheng Zhang and Zhongwei Chen contributed to the experiment and manuscript supervision.

Abstract

Access to fresh water has become one of the most urgent global issues because of growing fresh water consumption and wastewater emission. To treat this wastewater and increase the clean and sustainable water supply, there is a growing need for the development of advanced materials for water treatment. In this thesis, two research projects aimed at developing advanced materials for water treatment were conducted: i) the synthesis of an advanced magnetic flocculant for highly efficient solid suspension removal, and ii) the creation of advanced electrode materials for capacitive deionization (CDI).

An introduction to the global water crisis is presented in Chapter 1, along with the concepts of magnetic flocculant and CDI, the thesis objective, strategies, novelties, and the research outline. The literature review of magnetic flocculants and CDI electrode materials is discussed in Chapter 2. Several general material synthesis methods and characterization methods related to this thesis are discussed in Chapter 3. In Chapter 4, details regarding the synthesis and use of the magnetic Fe_3O_4-graphene oxide (Fe_3O_4-GO) nanocomposite for rapid flocculation of solid suspended particles in wastewater and natural water are presented. In Chapter 5, the development of a three-dimensional ordered mesoporous titanium nitride (3DOM-TiN) is presented as a next generation high-performance non-carbon CDI electrode material, with further in-depth studies revealing its novel dual adsorption

mechanism. In Chapter 6, a first-ever synthesis of a nanocomposite electrode of nitrogen-doped graphene-titanium oxynitride (NG-TiO_xN_y) for highly efficient CDI is presented. Detailed material synthesis methods, physiochemical and electrochemical characterization, adsorption analysis, electrosorption mechanism analysis, and CDI performance analysis can also be found in each chapter. Chapter 7 summarizes the work in Chapter 4-6. Additionally, several proposals and suggestions for future research are presented in Chapter 7. Supplemental information and preliminary experiments of Chapter 4-6 are given in the Appendix section.

Acknowledgment

First and foremost, I would like to express my sincere gratitude to my supervisor Professor Zisheng Zhang in University of Ottawa and co-supervisor Professor Zhongwei Chen in University of Waterloo for their help and instructions. Their patience, knowledge, and enthusiasm guided me throughout my Ph.D. study and research.

I would like to acknowledge to the China Scholarship Council for their continuous financial support to me throughout the past four years.

I also thank all the group members of the Applied Nanomaterials & Clean Energy Laboratory. Their help and support helped me complete my research and thesis writing.

I would also like to give my special acknowledgments to the following group members: Dr. Gaopeng Jiang, Dr. Guihua Liu, Dr. Wenwen Liu, Dr. Zachary P. Cano, Dr. Qian Li, Dr. Gregory Lui and Yan Liu, etc. They have given great effort and spent their personal time in helping the me for the research and thesis writing. I am not only cooperating with them but had sincere friendship with them.

I would also acknowledge the Wiley and the Royal Society of Chemistry for their publishing services.

Dedications

The thesis is dedicated to my loved parents.

Table of Contents

List of Figures

List of Tables

List of Abbreviations

AC	Activated Carbon
BET	Brunauer, Emmet, Teller Adsorption Isotherm
CDI	Capacitive Deionization
CV	Cyclic Voltammetry
EDX	Energy Dispersive X-ray Spectroscopy
EIS	Electrochemical impedance spectroscopy
FT-IR	Fourier-transform infrared spectroscopy
GCE	Glass carbon electrode
GO	Graphene Oxide
NG	Nitrogen-doped graphene
PTFE	Polytetrafluoroethylene
PS	Polystyrene
SAC	Salt adsorption capacity
SAR	Salt adsorption rate
SCE	Saturated calomel electrode
SEM	Scanning electron microscopy
TEM	Transmission electron microscopy
XPS	X-ray photoelectron spectroscopy
XRD	X-ray diffraction

Chapter 1: Introduction

1.1 Global Water Crisis

Access to clean water is one of the most urgent problems in the 21st century. Only 3% of the world's water is fresh, with the vast majority being seawater and non-potable water. Of the fresh water, humans can only access 0.5%; the rest is frozen and locked in remote areas and glaciers. Currently, over 650 million people lack safe drinking water. One-in-five deaths of children under five years old can be attributed to a water-borne illness.[1]

The clean water supply can be increased by purifying non-potable water. Two treatment steps are needed during the general wastewater treatment process: (i) removal of solid suspensions and, (ii) water desalination. Herein, two techniques for these treatment steps are introduced: magnetic flocculation for solid suspension removal and capacitive deionization for water desalination.

1.2 Magnetic Flocculation for Solid Suspension Removal

In general water treatment processes, the polluted water goes into a series of unit operations, whereby components are removed separately, The removal of suspended solid particles is typically a mandatory step during water processing.[2] The gravity settling method a well-established treatment technology for removing suspended solid particles. To accelerate the settling process, flocculants are often

added[3] The most common flocculants are polymer/ion composites with high-coordination capacities such as polyferric silicate sulfate (PFSS) and polyaluminum chloride (PAC). These compounds aggregate suspended components to form large particles that accelerate the gravity settling process. [4, 5] The magnetic flocculant is a kind of flocculants combining the magnetite core and the flocculants together to reach higher efficient in solid suspension removal under the presence of an external magnetic field.

In recent years, magnetic flocculants have been developed, based on polymer-magnetite flocculants.[6, 7] However, these compounds have low flocculation capacity and therefore require high dosing amounts to perform similarly to the traditional coagulating agents. Thus, the challenge of developing a novel magnetic flocculant was raised. The pollutants in wastewater can be solid suspended particles, heavy metal ions or organically soluble components.

1.3 Capacitive Deionization

Seawater and brackish water can be desalinated and treated to produce clean water.[8] Brackish water is a type of water with relatively low or moderate salt levels. It may result from the mixing of fresh water and seawater, or as a product of agricultural or industrial waste. Consequently, the development of desalination technologies has attracted considerable attention, and several methods have been developed and applied in large-scale industrial production of clean water, including

vacuum distillation, multi-stage flash distillation, multiple-effect distillation, vapor-compression distillation, and reverse osmosis. However, most of these technologies require a large energy input, and therefore have large operating costs. Moreover, these technologies require a separate heating or compression device to heat up or generate vacuum. Furthermore, they are usually performed under lower pressure, and thus are inapplicable in small-scale water desalination. Ghaffour analyzed the energy cost for a whole life capacitive deionization process and determined that the capacitive deionization process showed great advantages over conventional desalination technologies. [9]

Since the late 1960s, capacitive deionization (CDI) has become one of the most efficient methods for treating brackish water.[10] CDI is a form of electrodialysis technique, was introduced as a desalination method with considerable potential. CDI removes ions from water by applying voltage across two electrodes. Anions are removed from the water and stored in the anode, and vice versa. [11]CDI is primarily used in brackish water desalination and in wastewater treatment. In the 1970s, the mathematical model of CDI was studied,[12, 13] using the electrical double layer (EDL) model, which describes the ion ad/desorption on the surface of an electrode under an electrostatic field.

A typical CDI system pumps salty water from a reservoir and consists of a cell stack, a conductivity detector, and a computer for data processing. The CDI cell

stack is a two-electrode device with an ion absorption layer capacitor. It can be operated either in flow-by mode, i.e., the feedwater stream flows through the space between the electrodes, or in flow-through mode, i.e., the feedwater stream flows through the electrode. An ion-exchange membrane can be placed above the electrode film to enhance ion removal, which is the membrane CDI system. Several cells can be stacked together, with continuous salty water flowing between them. **Figure 1-1** demonstrates the schematic of a typical porous electrode flow-by CDI cell. CDI did not attract significant attention until 1995.[14] With the development of supercapacitor technology and electrode materials, it has become possible to use CDI to remove ions in water efficiently, and during the past two decades, a large amount of studies have been conducted on CDI electrode materials. The most important factor for enhancing CDI performance is a suitable material for the cell capacitor. Thus, most recent studies have focused on the development of porous carbon electrode materials.[15]

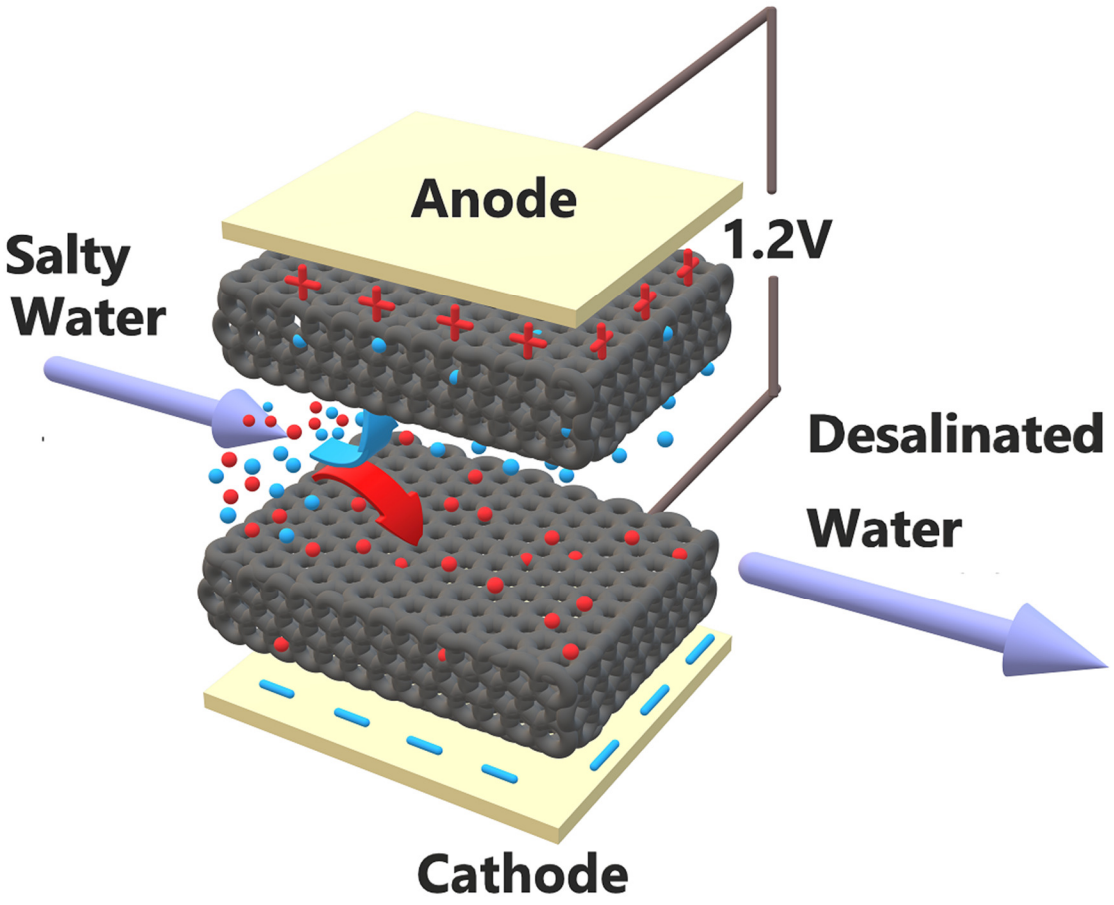

Figure 1-1 Schematic of a flow-by porous electrodes CDI cell.

1.4 Thesis Objectives and Approaches

The objectives of this study were to develop novel magnetic flocculants for solid suspension removal and novel CDI electrode materials with high salt removal rate, regeneration and cycling stability. To achieve these objectives, candidate materials were tested in preliminary studies (Appendices) and several materials were selected for further, in-depth analysis. The strategy and research process in this thesis are shown in **Figure 1-2**. The details of the approach for each material are discussed in the relevant chapters.

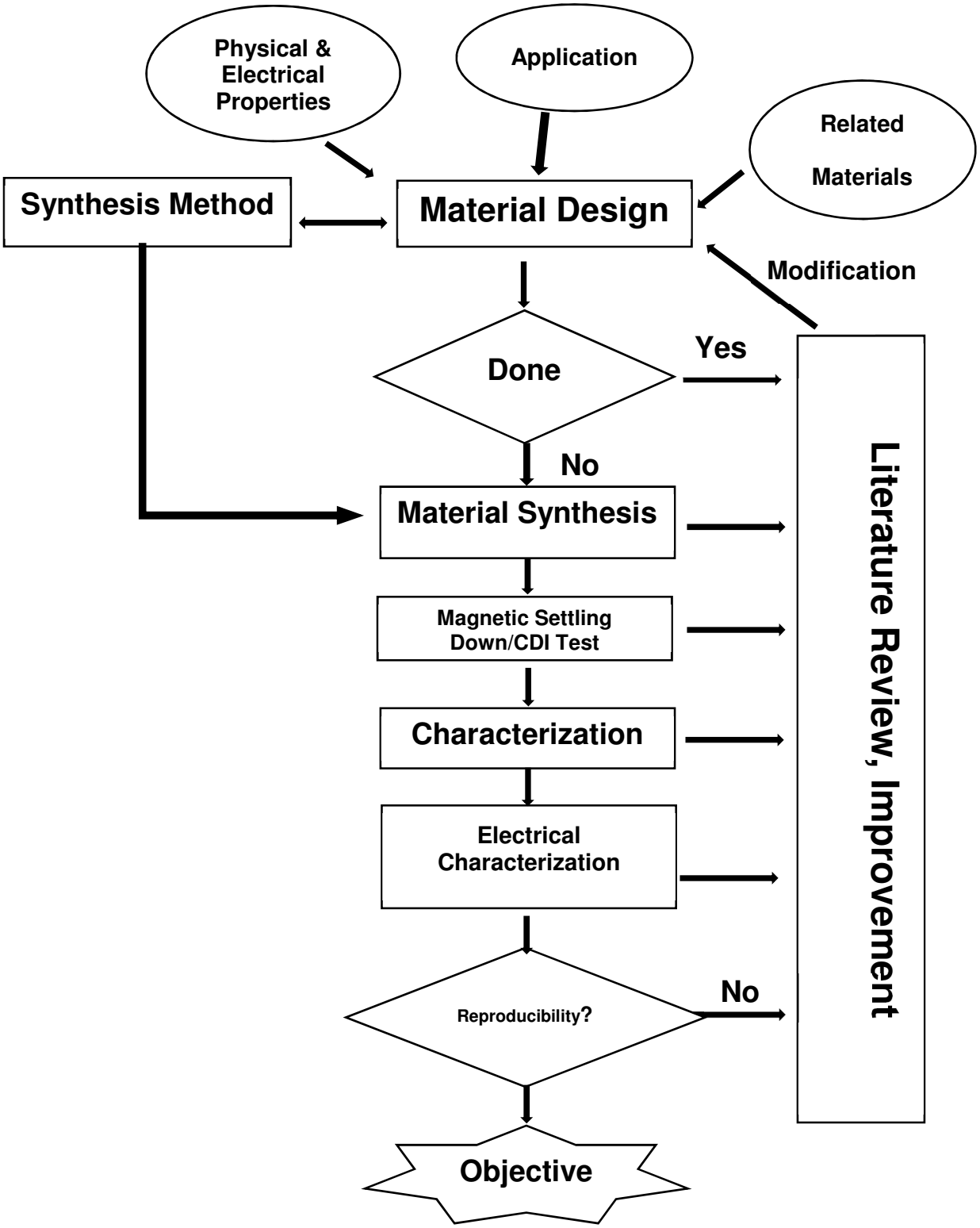

Figure 1-2 Research flowchart

The first phase of this study focused on the development of a magnetic flocculant for solid suspension removal. The strategy was to deploy an *in-situ* synthesis of magnetite incorporated onto absorbent material with a high surface area and adsorption capacity. The synthesized magnetic flocculant was tested in simulated kaolinite solid suspension water, and the removal rate was measured by visible-UV light adsorption on the upper liquid layer. The data were fitted with Langmuir and Freundlich models to explain the absorbing behavior of the synthesized magnetic flocculants.

The second phase of this study focused on the development a CDI electrode material. The desired material had a large surface area, high electrical performance and a high salt adsorption capacity. Several types of porous electrode materials that have been previously considered are studied (Appendix). Then a possible synthesis strategy was put forth, and the electrode material was tested on CDI cells in both batch and continuous mode. To increase the electrode performance, a porous titanium material was developed so that: i) its porous morphology was enhanced, ii) its surface area was increased, iii) its specific capacitance and another related electrical performance was improved, iv) its wettability in continuous-flow salty liquids was improved, v) its regeneration performance and long-term stability were improved.

Another advanced strategy was to develop dual-adsorption mechanism electrode materials with novel adsorption mechanism. The novel adsorption mechanism is the pseudo capacitance adsorption model beyond the conventional single-mechanism driven porous carbon electrode material. The study on the mechanism of the electrode materials would possibly achieve a breakthrough and foster new research in CDI electrode material studies

Accordingly, it is important to identify the advantages and disadvantages of the selected materials and modify their synthesis processes so that their intrinsic nanostructure characteristics may allow high salt retention capacity and so that the above requirements are met. An example is the porous titanium nitride (TiN), which has proven to provide improved salt retention capacity, higher surface area, and better electrical performance than most traditional carbon-based materials. However, porous TiN nanoparticles, such as porous titanium dioxide (TiO_2), suffer from low cycling stability and salt adsorption decay. The proposed approach for improving this material consists of nitrogen doping, forming an ordered structure, and incorporating graphene to assist nitrogen doping. These approaches bring about remarkable changes in the morphology and performance of the material. The synthesized electrode material was tested for regeneration capacity in over 10 cycles. Similar strategies were applied for the other materials investigated in this study.

To reiterate, the specific objectives of the thesis are as follows:

- The design and development of unique nanostructured magnetic materials capable of highly-efficient solid suspension removal;
- The solid suspension removal capacity should be no less than 50 mg mg^{-1} with rapid settling speed;
- The design and development of unique nanostructure materials capable of unit mass salt adsorption capacity higher than 15 mg g^{-1} NaCl in batch-mode CDI tests in 500 mg L^{-1} simulated brackish water at 1.2 V;
- Cycling stability, i.e., over 10 cycles for over 4 h, with at least 60% salt retention capacity to its initial salt adsorption capacity;
- The developed material should have good physical performance, for instance, high surface area and high mechanical stability;
- The developed electrode material should have good electrical performance, for instance, a high specific capacitance and good electrical conductivity;
- The synthesized material and methods should have the potential application for commercial and large-scale applications.

1.5 Research Outline

Chapter 4~6 introduced three works based on the above objectives and approaches.

In chapter 4, the magnetic Fe_3O_4-graphene oxide (Fe_3O_4-GO) nanocomposite was synthesized by a facile one-pot hydrothermal method and was used for settling and removing solid suspended particles in the wastewater. Physicochemical characterizations not only confirm the successful *in-situ* deposition of magnetic Fe_3O_4 nanoparticles on GO nanosheets but also demonstrate their strong interaction. The Fe_3O_4-GO nanocomposite can effectively accelerate the settling process in the presence of a magnetic field. It can reduce Kaolinite solid particle concentration by one order of magnitude within 30 min, which is twice the rate in the absence of a magnetic field. The solid suspension absorbing behavior of the Fe_3O_4-GO nanocomposite in the presence of a magnetic field is in good agreement with the Langmuir and Freundlich isotherm models and the pseudo-second-order kinetic model. The maximum calculated adsorption capacity is 58.46 mg g^{-1}, and that of the initial adsorption rate is 0.0275 mg^{-1} min^{-1}. The Fe_3O_4-GO nanocomposite is proven to be an effective, efficient, and a promising magnetic coagulant for the rapid treatment of solid suspended particles in wastewater and natural water.

In Chapter 5, a three-dimensional ordered mesoporous titanium nitride (3DOM-TiN) has been synthesized via a templating method as a novel high-performance non-carbon capacitive deionization (CDI) electrode material. The dual ion electrosorption mechanisms, fast ion diffusion and rapid charge transfer enabled by the multiple advantageous features of the 3DOM-TiN electrode boost an

outstanding CDI salt adsorption capacity (SAC) as high as 23.6 mg g^{-1} and a record-breaking maximum salt adsorption rate (SAR) of 3.2 mg g^{-1} min^{-1} when treating 500 mg L^{-1} NaCl solution at an applied voltage of 1.2 V. Such excellent CDI performance in addition to excellent cycling stability not only ranks the 3DOM-TiN electrode as one of the most promising electrodes for future CDI applications but also confirms the great potential of nanoengineered non-carbon electrodes for next-generation CDI cells.

In Chapter 6, a first-ever reported nanocomposite electrode of nitrogen-doped graphene-titanium oxynitride (NG-TiO_xN_y) for capacitive deionization (CDI) was synthesized via hydrothermal reaction and high-temperature nitridation process. The physiochemical characterizations revealed that the nitrogen was doped in the graphene structure mainly in the form of graphitic nitrogen and the TiO_xN_y was successfully formed via TiO_2 nitridation process. The layered NG nanosheets facilitated the diffusion of ions in saline water and formed electrical double layer on the surface of the electrode material, while the presence of TiO_xN_y enhanced the electrochemical performance by increasing surface area and generating surface vacancies via nitridation. The CDI cell employed NG-TiO_xN_y electrode delivered a breakthrough salt adsorption capacity of 26.1 mg g^{-1} in 500 mg L^{-1} saline water and retained over 90% of its initial salt removal efficacy after 12 regeneration cycles.

Such high CDI performance exhibits the promising application of NG-TiO_xN_y as a novel CDI electrode candidate.

Supplemental information and preliminary studies for Chapter 4-6 can be found in the Appendices.

Chapter 2: Literature Review

2.1 Magnetic Suspension Removal

Phase one of this study was focused on developing novel magnetic flocculants for magnetic-assisted solid suspension removal. Traditionally, magnetic flocculants are made from a magnetic-core and an outer layer. The magnetic core is usually made from magnetite (γ-Fe_3O_4), while the outer layer is typically made from polymer flocculants, such as polyferric silicate sulfate (PFSS), polyaluminum chloride (PAC), polyacrylamide, and chitosan etc. [4, 5] Graphene oxide (GO), a well-known absorbent material,[16]has not been substantially reported on in the literature as a solid suspension removal absorbent. In the following subsections, we will introduce graphene oxide and magnetite briefly.

2.1.1 Graphene Oxide as the Solid Suspension Adsorbent

Graphene oxide is a layered-structure compound of carbon, oxygen, and hydrogen in variable ratios. It is synthesized by treating graphite with strong oxidizers. GO sheets have high similarity to graphene single-atom sheets, with a C:O ratio from 2.1 to 2.9. GO is a one-atom-thick nanosheet of sp^2-bonded carbon atoms, with a high specific area, and high crystal and electronic quality. GO was first synthesized in 1859 (Brodie, 1859) by treating graphite with a mixture of potassium chlorate and fuming nitric acid. In 1957, Hummer and Offman developed the Hummer method using sulfuric acid, sodium nitrate, and potassium permanganate

to oxidize the graphite nanosheet.[17] It is currently the most widely used synthesis method.

GO is hygroscopic and has the potential advantages in absorbing wastes in water solution.[18] Further, with its 2D and 3D structure, it is an ideal pollutant-adsorbing and ion exchange material. Recent studies indicate that GO can be used for removing heavy metal ions, such as Pb^{2+}, Cu^{2+}, and Co^{2+}, from water.[19-21] GO has been studied for reverse osmosis in water treatment.[22] Owing to its ion-selective property, large ions can be filtered from the GO's membrane, and small ions can pass through the layered structure. O'Hern studied a single-layer GO membrane with selective ionic transport owing to its tunable sub-nanometer pores.[23] Motes-Navajas measured the surface area of GO in liquid.[24] It can reach a maximum of 736.6 $m^2 g^{-1}$ in a diluted solution. Due its large specific surface area, and good ad/desorption in both physical and electrosorption, GO has attracted considerable attention as an ideal material with wide application in water treatment, including toxic organic substance and dye adsorption[25, 26] However, none of this research has focused on using GO as a solid suspension adsorbent. Thus, the idea of using GO as the out-layer absorbent of magnetic flocculant was tested and verified in this work.

2.1.2 Fe_3O_4 as the Magnetic Core in Magnetic Flocculation

γ-Fe_3O_4 is one of the most commonly used materials in magnetic core synthesis.[27] Despite its wide application, conventional magnetic flocculants

generally loosely incorporated the Fe_3O_4 with liquid polymer-flocculants physically.[26] Sun et al. reported using Fe_3O_4 cored reduced GO nanocomposites as a platform for removal of dye pollutants. [28] Chandra et al. reported using Fe_3O_4 core/reduced GO for arsenic removal.[29] Other reports also suggested that magnetic Fe_3O_4 could be used as core in absorbent in magnetic-assist absorbing.[30-32] However, *in-situ* synthesized γ-Fe_3O_4 flocculant as the magnetite core in adsorbent materials for water solid suspension removal has not been reported in the literature

2.2 Capacitive Deionization

Phase two of this study was focused on developing novel electrode materials for capacitive deionization (CDI) technology. Currently, most porous carbon-based CDI electrodes are based on the electrical double layer (EDL) adsorption model, which is introduced below. Moreover, several important electrode materials related to this study are also introduced in this section.

2.2.1 Electrical Double Layer

EDLs are fundamental to modeling a CDI system. According to Paul et al.,[33] the EDL is a region at the interface between a solution and solid electrical materials where an excess charge may exist even though the electrodes are electrically neutral. Johnson et al. developed the first EDL model in the 1970s.[12, 34] They assumed that ion absorption in the CDI is approximately a capacitive process, whereas adsorption kinetics do not limit the charging rate, and faradaic reactions are negligible.

The double sides of the electrodes interfacing with an opposite electrical charge are termed as EDL, and the most widely accepted model for describing the EDL is the Gouy–Chapman–Stern model.[35] In the Gouy–Chapman–Stern model,[36] as shown in **Figure 2-1,** the double layers are assumed to be divided into an inner region on the electrode surface (the Helmholtz layer), and the diffusion region (the Gouy-Chapman layer). The Helmholtz layer is where ions of the electrode surface are transferred directly onto the electrode surface, while, the Gouy–Chapman layer is where the electric charge is diffused, and the charge distribution depends on the surface potential.

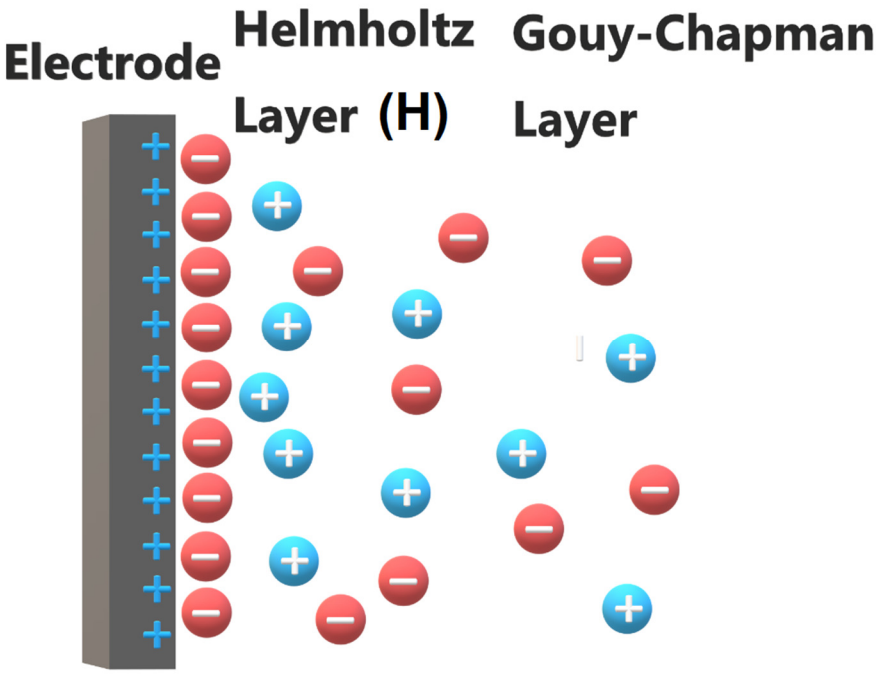

Figure 2-1 Distribution of Charges in a Gouy-Chapman-Stern model.

The capacitance of the Helmholtz and Gouy–Chapman layers contributes to the total capacitance. **Equation 2-1** can be used to calculate the total capacitance by considering the Helmholtz and Gouy–Chapman layers:

$$\frac{1}{C_T} = \frac{1}{C_{M-H}} + \frac{1}{C_{H-S}} \quad \textbf{(2-1)}$$

where C_T is the total capacitance of the two capacitors in series; $C_{M\text{-}H}$ is the capacitance of the double layer between the electrode surface *M* and the plane of closest approach *H* for the ions; $C_{M\text{-}H}$ is the capacitance of the diffuse double layer from *H* into the solution; and C_{H-S} is the capacitance of the Gouy–Chapman layer.

In an ideal parallel capacitor model, charge separation is electrostatic. The capacitance is proportional to the area of the electrode plates and the inverse distance of separation, as shown in **Equation 2-2**:

$$C_{M-H} = \varepsilon_r \varepsilon_0 \frac{A}{D} \quad \textbf{(2-2)}$$

where *A* is the area of each capacitor plate; ε_r is the relative electrostatic permittivity (dielectric constant) of the material between the plates; ε_0 is the permittivity of free space (8.854×10^{-12} F m^{-1}); and *D* is the separation between the plates (m).

Gouy and Chapman developed an ideal model, where ions are treated as point charges, and the electrodes are ideally polarized, [37, 38] as shown in **Equation 2-3**.

$$q = \left(\frac{2RT\varepsilon C_s}{\pi}\right)^{\frac{1}{2}} sinh\left(\frac{|z|\Im\Phi_H}{2RT}\right) \quad \textbf{(2-3)}$$

Where $|z|$ is the electrical valence; q is the excess charge; R is the ideal gas constant; T is the absolute temperature; Φ_H is the electrical capacitance; C_s is the bulk concentration; and ε is the electrostatic permittivity of the electric field.

The electrical capacitance of the diffuse double layer is then obtained by differentiating **Equation 2-3** with respect to Φ_H.

$$C_{H-S} = |z|\Im\left(\frac{\varepsilon C_S}{2RT\pi}\right)^{\frac{1}{2}} \cosh(\frac{|z|\Im\phi_H}{2RT}) \quad \textbf{(2-4)}$$

Figure 2-2 shows the excess charge distribution at the interface between a charged electrode-electrolyte solution according to the Gouy–Chapman–Stern model.

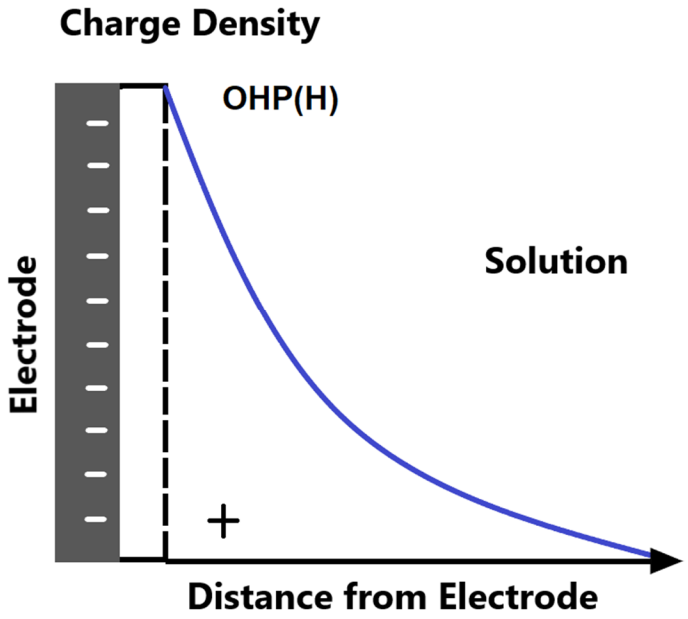

Figure 2- 2 Schematic representation of charge distribution in an electrolyte. The outer Helmholtz plane is indicated by OHP(H).

Biesheuvel et al.[39-41] further investigated the EDL model in CDI, as shown in **Figure 2-3**. The figure demonstrates that when two oppositely-charged electrodes are in equilibrium with the same electrolyte solution, excess charge is built up at the interface near each electrode.

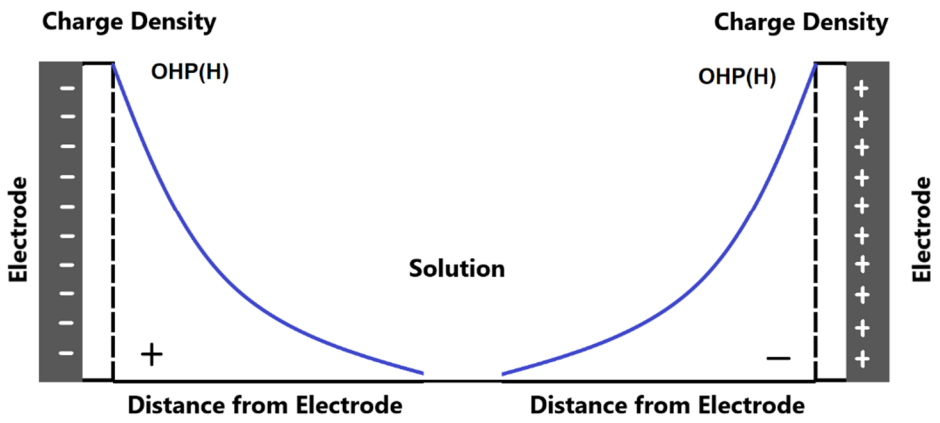

Figure 2-3 Excess charge distribution in a two-electrode system.

Biesheuvel et al. examined the prediction model using NaCl salty water as the simulated feed water in a CDI system. [39-41] The experimental data were fitted to the prediction results successfully, thereby introducing attractive forces in the micropore electrode model. Schocron and Suss observed certain model conditions in which surface transport enhances cell charging rates, and counter-intuitively, this additional transport pathway was found to slow down cell charging in other model conditions.[42]

2.2.2 Adsorption Model

The ion adsorption on the surface of the electrode can be explained by the Langmuir and Freundlich adsorption isotherms model.[43] In this model, the concentration gradient driving the ions to be adsorbed on the surface of the electrode is treated as the electrical force. In both the Langmuir and Freundlich models, equilibrium is reached as a result of surface saturation on the carbon material. Gabelich et al. used Langmuir, Freundlich and BET isotherms in their study on electrosorption of ions onto carbon aerogels.[44] In their study, the Langmuir adsorption isotherm is given using **Equation 2-5**:

$$\mathrm{X} = \frac{X_m b C_e}{1 + b C_e} \qquad (\mathbf{2\text{-}5})$$

Where X is the per unit weight of adsorbent; C_e is the equilibrium concentration of the solution; and b is the stoichiometric concentration of the solution.

The Freundlich isotherm can also be used to describe the adsorption in solution:

$$x/m = KC_e^{(1/n)} \quad \textbf{(2-6)}$$

Where x is the amount of solution adsorbed; M is the weight of adsorbent; C_e is the equilibrium concentration of the solution; and K and n are empirical constants depending on the system.

2.2.3 Analysis of a CDI Cycle in a Two-Electrode Model

A typical CDI design uses two porous carbon electrodes whose thickness is between 100 and 500 μm. The brackish water flows through the gap between the two parallel electrodes, as shown in **Figure 2-4**. A typical "flow-by" electrode at laboratory scale ranges from 5×5 to 10×10 cm^2. The electrode can either be a thin film attached to the metal mesh or be coated on the collectors. The system can be tested as a single pair (supercapacitors) or a stack of multiple cell pairs.

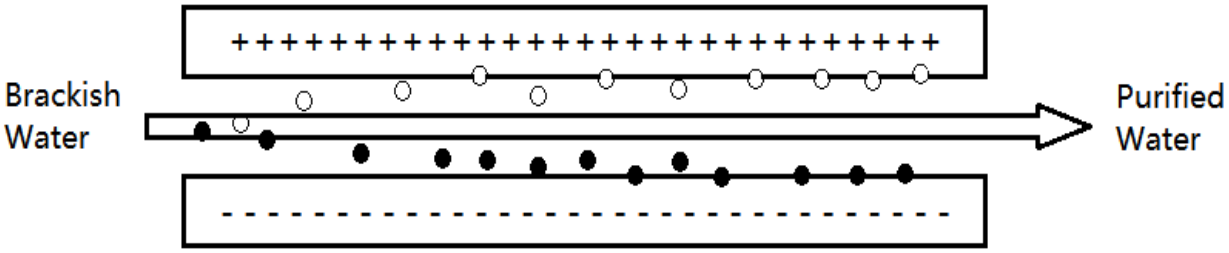

Figure 2- 4 Schematic of a flow-by CDI cell.

2.2.4 Operation of CDI

Several factors influence the performance of a CDI system. with the most important being the electrode material. Properties such as surface area, pore size and pore size distribution have a great effect on the performance of the system. Thus, carefully manufacturing the electrode material for efficient CDI operation is the main concern.

The CDI cell is connected with a peristaltic pump to pump feed in salt water. By combining single CDI cells together, CDI cells can gain much higher desalination performance to meet the requirements of industrial water desalination standards. The salinity of desalinated water is measured by a conductivity meter at the out flow. The schematic of a whole CDI stack system is shown in **Figure 2-5**.

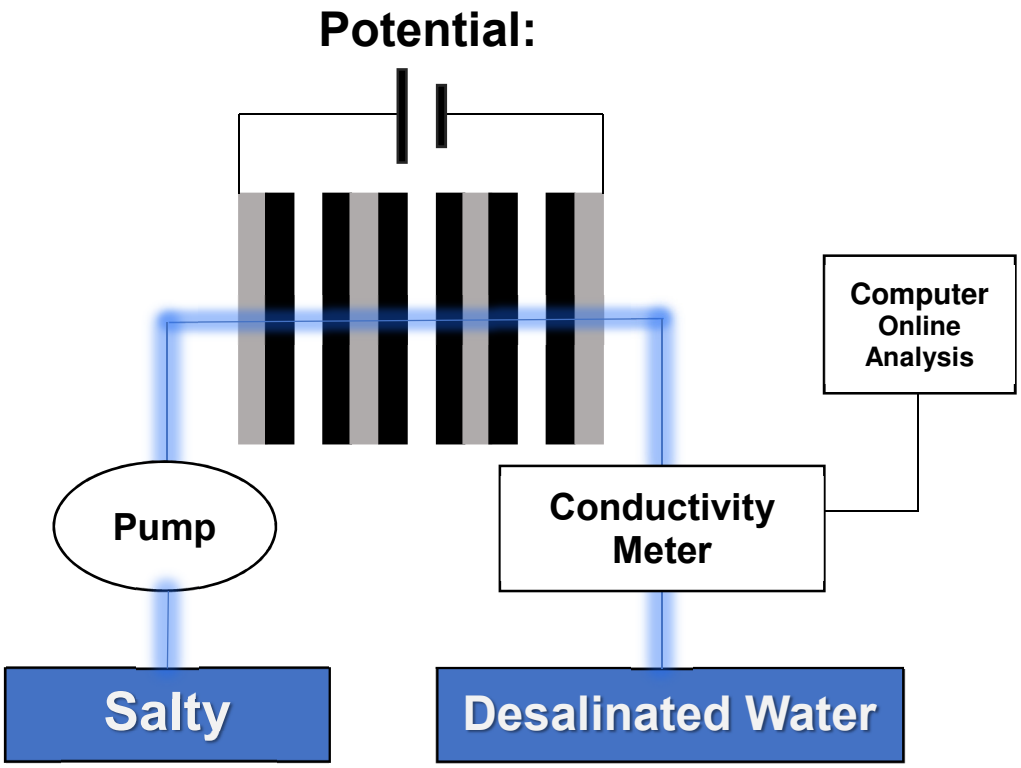

Figure 2-5 Schematic of a CDI analysis system.

2.2.5 Feed Water Composition and Concentration

Currently, the CDI technique is mainly used to desalinate brackish water and industrial waste water with salinity similar to brackish water. The brackish water is water having more salinity than freshwater, but not as much as seawater, which contains between 0.5 and 30 grams of salt per liter water. The brackish water habitats are estuaries, mangroves, brackish seas and lakes. [45]

The composition of the feed in salty water may vary depending on if simulated brackish water, real brackish water or simulated industrial waste water is used. Water containing a single component, such as NaCl or KCl, is the most commonly-used simulated brackish water at the lab-scale. Water containing multiple components is used to simulate natural brackish water or industrial wastewater with heavy metal ions. It may also be real-waste or brackish water. However, real water should be pre-treated to remove large particles and biological or organic matter to avoid destroying the porous electrodes, if real brackish water is chosen to be the feed water.

The feed and purified waters can be analyzed using chromatography or inductively coupled plasma optical emission spectroscopy to determine their compositions and assess the composition changes due to treatment. Such a test is usually conducted off-line. For single- or multiple-component simulated water, the composition of feed water is fixed, and the out-flow water can be detected online to

analyze the composition changes after the flow through the cell. The test can also be combined with a conductivity meter.

2.2.6 Electrical Potential

In the EDL model, higher capacitor voltage implies freer electric charge on the electrode surfaces, and hence (in theory) better ion adsorption performance. However, the applied voltage has an upper limit, which is 1.23 V of the water electrolysis voltage.[35] Thus, the cell voltage of the CDI system is usually 1.2 V.

2.2.7 Electrode Material

One of the most important factors in performance of the CDI system is the electrode material. An ideal CDI electrode material should meet the following requirements:

1. Large specific surface area, which implies high electrosorption capacity.
2. Uniform morphology, which results in a positive effect on electrical conductivity.
3. High electrical conductivity.
4. Rapid response of the entire surface area to electrosorption–electrode sorption changes.
5. Stability to wide pH variations and to the presence of non-ionic components such as oxidants and colloids.
6. Stability to wide voltage variations.

7. Cycling stability, retaining at least 50% of its initial desalination capacity after multiple cycles.

The earliest and most commonly-used material is porous carbon, which has low cost, large surface area, and good electrical properties. Since 1995, various types of electrode materials have been developed, such as activated carbon (AC), carbon aerogel, ordered mesoporous carbon, inorganic additives in carbon-based materials, carbon nanotubes, and polymer-coated carbon materials.[8] Developing an electrode material with high salt removal efficiency and high regeneration capacity has been the main concern of the research on CDI in the past two decades.

2.3 Electrode Materials Related to this Thesis

Even though the concept of CDI appeared in the 1960s, limited research was conducted between the 1960s and 1990s. During the past two decades, several types of electrode materials were developed[14]. The most commercially-available and well-known electrode materials related to this thesis are presented in the following subsections with brief introduction to their physical and chemical properties.

2.3.1 Activated Carbon

Activated carbon (AC) is a low-cost absorbent used in industrial applications and can be the base material in preparing CDI electrodes that support other functional additives. AC is primarily produced by the pyrolysis of carbonaceous

source materials such as nut shells and wood at temperatures under 1000 °C.[46] Alternatively, the raw material can also be activated by acid, strong base, or salt prior to carbonization, which is performed at a lower temperature.[47]

AC has been used as an electrode material by Murphy and Caudle et al. at the early stages of CDI research.[11, 48] Since 1995, numerous works have been concerned with using AC as the CDI electrode material or by incorporating various additive species during fabrication, tuning the pore size, the specific surface area and conductivity to enhance ad/desorption performance.[10] Until now, AC is still among the cheapest, most accessible and least commercialized CDI electrode materials. Thus, AC is often used as the standard reference CDI electrode materials in CDI tests.

2.3.2 Titanium

Titanium (mostly TiO_2) is a widely-used functional material in water pollution treatment. It is reported that the conversion of the electric properties of titanium atoms in the presence of an electric field is responsible for the significant increase in the electric field adsorption of TiO_2-modified AC.[49] Ryoo et al. studied the role of incorporating TiO_2 in AC electrodes.[50] AC cloth was modified by adding metal alkoxides of titanium, silicon, aluminum, and zirconium to enhance its CDI performance. The presence of titanium atoms increases the adsorption sites for ions under an electric field. The authors also observed a similar phenomenon with the

modification of silica-, alumina-, and zirconia-AC. Liu et al.[51] used a microwave-assisted method to synthesize an anatase/titanium dioxide/AC composite. The single-direction polarity of TiO_2 particles enhanced the reversal of the adsorption of AC. The authors used both direct blend and a microwave-assisted method to synthesize the TiO_2–AC cloth. Kim et al. used a TiO_2 sol-gel spray method for carbon electrodes.[52] The presence of TiO_2 and SiO_2 additives attracted high water content and increased the wettability of the electrode, the inhibition of physical adsorption of ion species affecting electrochemical ad/desorption during CDI, and the alteration of the surface zeta-potential on the carbon electrode to increase the ion removal rate. The previous studies revealed that titanium and its derivatives could be a useful additive in porous carbon-based CDI electrode materials or even candidates for non-carbon CDI electrode materials.

2.3.3 Graphene Oxide and its Derivatives

Graphene oxide (GO) has long attracted considerable attention and is used as an electrical material in various applications, including supercapacitor electrodes, which shares several similarities with CDI. However, limited research has been conducted on its use as a CDI electrode material.

By oxygen reduction (rGO), the conductivity of graphene oxide can reach approximately 1000 S/m [53]. GO has a strong interaction with water owing to its large specific area,[54] and is an ideal material for water treatment with high wettability.

Electronic properties such as conductivity depend on the chemical composition and structure of the GO nanosheet. Conductivity is closely related to the degree of structural disorder. Several studies have been conducted on the electrochemical applications of GO and rGO.[55–56] It has been demonstrated that these materials have a strong potential in several electrochemical applications.[75–57] Shao exposed graphene to nitrogen plasma and obtained nitrogen N-doped graphene (NG), [58] which exhibited significantly higher electrocatalytic activity toward oxygen reduction and H_2O_2 reduction than graphene due to the nitrogen functional groups and the specific properties of graphene. Inhwa et al.[59] used a step-by-step thermal reduction process to synthesize GO, and successfully strengthened the external electrical field, the density of the transport current, and temperature. Thus, it is reasonable to consider using GO and its derivatives as novel functional materials for capacitive deionization.

For comparison, recent electrode material developments and recent studies on CDI electrode materials are listed in **Table 2-1**.[10–15]

Table 2-1 CDI performance of various electrode materials

Electrode Material	Initial Salt Concentration (mg L^{-1})	Cell Voltage (V)	Salt Adsorption (mg g^{-1})
Carbon Aerogel[60]	50	1.2	1.4
Carbon Aerogel	500	1.2	2.9
AC powder[61]	100	1.2	6.1
	200		8
	500		9.72
	1000		10.8
	1500		11
	2000		11.76
Ti-Active Carbon Cloth [50]	5844	1.2	4.3
Multi-walled CNTs [62]	3000	1.2	1.7
CNTs-Carbon nanofibers [63]	110	1.2	3.3
OMC[64]	25	1.2	0.68
OMC[65]	50	1.2	0.93
AC[66]	200	1.5	3.7
AC	200	1.5	5.3

Electrode Material	Initial Salt Concentration (mg L^{-1})	Cell Voltage (V)	Salt Adsorption (mg g^{-1})
Commercial AC electrode[67]	292	1.4	10.9
	1170		13.0
Graphene-like nanoflake[68]	25	2.0	1.3
Single-walled CNTs[69]	23	2.0	0.75
Commercial AC electrode[70]	292	1.2	10.5
MnO_2-AC[71]	25	1.2	1.0
Carbon nanofiber webs[72]	95	1.6	4.6
Sulphonated graphite nanosheet[73]	250	2.0	8.6
Graphene-CNT[74]	29	2.0	1.4
Reduced graphene oxide-AC[74]	50	1.2	2.9
Ordered OMC/CNTs[74]	46	1.2	0.63
Carbon aerogel monoliths[74]	2922	1.5	9.6
Reduced graphite oxide-resol[75]	65	2.0	3.2
AC[75]	292	1.4	12.4
Carbide-derived carbon[75]	292	1.2	14.9

Electrode Material	Initial Salt Concentration (mg L^{-1})	Cell Voltage (V)	Salt Adsorption (mg g^{-1})
AC powder[76]	1170	1.0	10
AC/ion-exchange resin[77]	2000	1.4	18
Polyrrole/graphene[78]	1000	1.4	15
AC cloth[79]	100	1.2	7
Three-dimensional hierarchical[80] porous carbon[80]	30	2	80
Carbon cloth[81]	550	1.2	100
	5500	1.1	
CNT sponge[82]	60	1.6	90
CNT/polyacrylic acid[83]	50	1.2	350

Chapter 3: Experimental Methods and Characterization Techniques

3.1 Material Synthesis

The general experimental methods of synthesizing two major materials, the GO and TiN are described below, detailed experimental methods are discussed in each chapter.

3.1.1 Synthesis of Graphene Oxide

The GO was synthesized by a modified Hummer method.[84, 85] More specifically, 3.0g of graphene powder and 1.5g sodium nitrite (Sigma Aldrich) were mixed in a flask with 200 mL of 98% sulfuric acid and stirred for approximately one hour at 90 °C. Then, the flask was transferred into an ice bath, and 9.0g potassium permanganate was slowly added and vigorously stirred for 24 hours. Then, 500mL of deionized water was added into the flask to avoid boiling while adding the water. Then the solution was heated to 35°C, stirring for another 24 hours. During the stirring, the color of the aqueous solution turned to a dark brown color. 30 mL of hydrogen peroxide was then added to the solution, causing the color to change to a light shade of yellow. After two hours of continued stirring, the solid product was washed with 5% hydrochloric acid and deionized water several times. The final product's color was dark brown. For characterization of the synthesized GO, the wet

product was centrifuged, frozen with liquid nitrogen and finally freeze-dried for three days until the GO turned into a light brown powder.

3.1.2 Polystyrene (PS) Template Synthesis

The PS template synthesis method in this thesis is based on previous work where the templates were used in the preparation of order TiO_2 nanoparticles. [86, 87] In detail, 200mL boiled distilled deionized water (oxygen-free DDI) was added into a three-neck flask. Then, 2.5g polyvinylpyrrolidone (PVP, M.W. 10,000) was added under magnetic stirring until the PVP fully dissolved in the oxygen-free water. The flask was then put into an oil bath purged with nitrogen gas to expel oxygen and heated to 70°C for 15 mins. 24 mL of styrene monomer was added to the flask and stirred for 20 min. Subsequently, 40 mL of 5g ml^{-1} potassium persulfate solution was added using a funnel with a drop rate lower than 15 drops per minute. The flask was continuously stirred and maintained at 70°C in an air-free atmosphere for 24 hours. After the reaction stopped, filtration was used to remove particles from the solution. Then, the solution was centrifuged at 3000 rpm for 12 hours to form ordered PS template nanoballs. The PS template was dried at a temperature <40°C overnight.

3.2 Characterization Techniques

Physicochemical characterization is important to understand the relationship between electrochemical performance and the characteristics of the developed

materials (*i.e.*, chemical composition, physical morphology, and structure). The physicochemical investigation is a crucial step in the strategic loop used in this thesis. Understanding the effect of material structure and chemical composition on the electrochemical performance is essential to identify the shortcomings of the material. This can help in refining the design of the synthesis procedures. The following sections will introduce the theory and the importance of the selected characterization techniques.

3.2.1 Scanning Electron Microscopy

Scanning electron microscopy (SEM) is a high-resolution imaging technique used to examine the morphology of materials at the micro/nano- scales. The working principle of SEM involves directing a beam of short-waved electrons onto the surface of the inspected sample. The electron beam is generated from an electron gun (wires connected to a high voltage source, 15-30 kVA), the beam is focused on the sample by a set of electromagnetic lenses. When the electron beam hits the sample's surface, secondary and backscattered electrons will be captured by detectors fixed above the sample. The electron beam is raster scanned over the inspection area, and the detected electrons will be converted into electrical signals which are processed by a data acquisition system to generate the final image of the inspected area.

3.2.2 Transmission Electron Microscopy

Transmission electron microscopy (TEM) is a powerful imaging technique that provides in-depth information about the physical characteristics of the investigated sample at the nano and atomic scales. The working principle is based on directing electrons that are generated by a field emission beam onto the sample. When the electrons reach the sample, they will be transmitted through the sample and captured by detectors. The captured electrons will be transformed into electrical signals and converted into high-resolution images that can help visualize the material morphology and crystal orientation at the atomic level.

3.2.3 Elemental Mapping

Elemental mapping is the image obtained from SEM and TEM scanning, showing the spatial distribution of elements in a sample. Since the sample requires polishing prior to elemental mapping, the result is a 2D image showing the compositional zonation of the material.

3.2.4 Energy Dispersive X-ray Spectroscopy

Energy dispersive x-ray spectroscopy (EDS) is a quantitative and qualitative analysis technique that is used for the identification of the sample's chemical composition through elementals analysis. EDS is usually coupled with SEM and TEM and can be done simultaneously with imaging. The collision of the electrons with the sample will emit X-rays which can be captured by a detector. The analysis

of the binding energy of the emitted X-rays versus reference fingerprints for different elements enables the identification and quantification of the material's chemical composition.

3.2.5 X-ray Diffraction

X-ray diffraction (XRD) is an important and fast analytical technique that is used to identify the crystal structure of the investigated sample and provide information about unit cell dimensions. X-rays with specific wavelengths are emitted from a beam source at a specific angle toward the inspected sample. When the X-rays bombard the sample, they will interact with the material atoms before being reflected with different intensities and creating a pattern. The diffracted X-rays will be collected by a detector and processed to generate a spectrum which will be compared versus well-known fingerprints for materials to identify the investigated material. The lattice spacing can be found using the relationship between the angle of diffraction and the specific crystal orientation using Bragg's law shown in the following **Equation 3-1**:

$$2d\sin\theta = n\lambda \quad (\mathbf{3\text{-}1})$$

Where n is the order of the spectrum (integer number), λ is the X-ray wavelength, d is the distance between the sample plane, and θ is the introduced X-ray angle to the surface of the material.

3.2.6 X-ray Photoelectron Spectroscopy

X-ray photoelectron spectroscopy (XPS), also known as electron spectroscopy for chemical analysis (ESCA), is a powerful analysis technique that can provide qualitative and quantitative information about the investigated materials. XPS is a surface-sensitive technique capable of measuring the elemental composition at very high precision for the atoms existing at 0.5 to 10 nm from the surface of the sample. XPS provides detailed information about the chemical formula and chemical state of the materials. The working principle is based on sending an X-ray with known energy to bombard the surface of the examined material causing vibrations in the atomic bonding and emissions of electrons. The emitted electrons are counted, and their kinetic energy is measured. By calculating the change in total energy between the sent beam and the emitted electrons, the energy needed to excite and emit these electrons can be calculated, which will be equal to the binding energy of these electrons. The binding energy is characteristic of the atom type and chemical state.

3.2.7 Thermogravimetric Analysis

Thermogravimetric analysis (TGA) is an analysis technique that measures the change in the weight of the investigated sample versus temperature increase at a fixed rate or versus time at a fixed temperature. TGA can provide useful information about the composition of the tested sample as a function of mass loss or mass gain.

3.2.8 Brunauer–Emmett–Teller

Brunauer–Emmett–Teller (BET) is a useful analysis theory that provides information about the specific surface area of the investigated materials. BET is based on measuring the physical adsorption of a nitrogen multilayer as a function of relative pressure. BET instruments are usually equipped with a Barrett-Joyner-Halenda (BJH) pore size and volume analyzer that can provide information about the pore area and pore volume from the adsorption-desorption measurement.

3.2.9 Raman Spectroscopy

Raman spectroscopy is an analytical technique that can provide qualitative and quantitative information about the chemical composition of the investigated materials based on vibrational spectroscopy. The measurement theory is based on sending a monochromatic laser light at a known frequency onto the material and analyzing the intensity of the scattered light. When the laser beam hits molecules in the material, a shift in energy will happen due to the interaction of light with the molecule causing a shift in the vibrational energy levels of the excited molecules. Plotting the intensity of the shifted energies versus the frequency of the inbound light yields a characteristic plot often referred to as a “fingerprint” that can be matched to a known plot from a chemical database. Raman plots are also used to study chemical bonds or verify the addition of attachments to substrates.

3.2.10 Fourier-transform infrared spectroscopy (FTIR)

Fourier-transform infrared spectroscopy (FTIR) is a technique used to obtain an infrared spectrum of absorption or emission of a solid, liquid or gas sample. An FTIR spectrometer simultaneously collects high-spectral-resolution data over a wide spectral range. This confers a significant advantage over a dispersive spectrometer, which measures intensity over a narrow range of wavelengths at a time.

3.3 Electrochemical Characterization

3.3.1 Cyclic voltammetry (CV)

Cyclic voltammetry measurement was carried out using NaCl solution with the concentration of 0.1, 0.5 and 1M; the sweeping potential ranged from 0 to 1 V in an electrochemical cell with a three-electrode system: carbon electrode as the counter electrode, SCE as the reference electrode and the prepared materials as the working electrode. The system works with a VeraStat 4 potentiated device. The specific capacity was calculated by integrating the area of the CV curve to determine the average value using the following **Equation 3-2**:

$$C_s = \frac{\int I \, dV}{2v\Delta V m} \qquad \textbf{(3-2)}$$

Where C_s is the specific capacitance (F g^{-1}), I is the current (A), v is the scan rate (V s^{-1}), ΔV is the applied potential windows (V), and m is the electrode material

mass (g). Electrochemical impedance spectroscopy (EIS) measurements was carried out at frequency ranging from 10 to 0.01 Hz. The amplitude of the alternating voltage was 10 mV and the potential was 0V.

The electrosorption capacity is shown in **Equation 3-3**:

$$\Gamma = \frac{(\mathrm{C_0} - \mathrm{C_e}) \times \mathrm{V}}{\mathrm{m}} \quad (\mathbf{3\text{-}3})$$

Where C_0 and C_e are initial and equilibrium NaCl concentrations (mg L^{-1}), V is the volume of NaCl solution (L) and m is the total mass of the electrodes (g).

Charge efficiency (Λ), a useful tool for evaluating the total charge, defined as the ratio of the amount of electro-adsorbed ions to the equivalent total charge, was calculated using the following **Equation 3-4**:

$$\Lambda = \frac{(C_0 - C_t)V}{\sum / \mathrm{F}} \quad (\mathbf{3\text{-}4})$$

Where Σ is the charge obtained by integrating the corresponding current and F is the Faraday constant (96485 C mol^{-1} e^-).

3.3.2 Galvanostatic Charge-Discharge

Galvanostatic charge-discharge (CD) is a well-established measurement technique that can provide useful information about the electrochemical characteristics of the cell. The test protocol is based on charging and discharging the working electrode at a fixed current density within a specific voltage window. In a

typical CD experiment, when the working electrode is charged or discharged at fixed current density, the amount of charge transferred between the electrodes will remain constant. The change in potential and time are measured and varied based on the current density that is applied. The analysis of the voltage and time dynamics with current density can provide useful information about electrochemical characteristics of the investigated materials. The specific capacitance can be calculated from the charge-discharge curve as per the below **Equation 3-5**:

$$C_s = I/(m\,\Delta V/\Delta t) \quad (\mathbf{3\text{-}5})$$

Where C_s is the specific capacitance (F g^{-1}), *I* is the discharge current (A), m is the mass of the active material (g), and $\Delta V/\Delta t$ is the discharge curve slope (mV s^{-1}) obtained after the voltage drop.

3.3.3 Electrochemical Impedance Spectroscopy

The impedance can be defined as the opposition to current flow or voltage change.[52] Electrochemical impedance spectroscopy (EIS) provides information about the resistance of electrodes and electrolyte, as well as the charge transfer process. EIS measures the impedance of the cell over a range of frequencies.

Chapter 4: Highly Efficient Removal of Suspended Solid Pollutants from Wastewater by Magnetic Fe_3O_4-Graphene Oxides Nanocomposite

This section is published on *Chemistry Select* and reprinted for this chapter with the permission from Wiley. Supplemental information, preliminary experiments and cost-effective analysis can be found in **Appendix A**.

4.1 Chapter Introduction

Obtaining clean water is one of the biggest issues to be solved in the 21st century,[88] with water purification being an effective way to increase clean and drinkable water supplies. The water sources that need to be purified include industrial wastewater, urban life wastewater, and agricultural wastewater. Natural water such as seawater, underground water, and river water also contains various components that need to be removed before drinking and industrial utilization.[89] The pollutants in wastewater can be solid suspended particles, heavy metal ions or organic soluble components. Generally, the polluted water goes into a series of treating units, and these components are removed separately, in which removing suspended solid particles is usually a mandatory step during water processing.[2] The gravity settling down method is one of the oldest and most mature technologies for removing suspended solid particles. To accelerate the settling process, coagulants is

added to the suspension solution, and suspended particles flocculate and form large particles to accelerate the gravity settling.[3] The most common coagulants are polymer bound with ions with high-coordination capacity such as polyferric silicate sulfate (PFSS) and polyaluminum chloride (PAC) to combine suspended components in the water together and form large particles and settle down. [4] [5] To increase the settling efficiency, coagulant agents can also be prepared with magnetic nucleus such as Fe_3O_4 and used with a magnetic field to further accelerate the settling process. This kind of magnetic flocculation has been used in mineral refinement since last 1980s[90, 91] and has attracted lots of research interest.[92] However, traditional polymer-based magnetic coagulants usually require several hours or days to fully settle down a batch of industrial wastewater,[93] while the remaining trace amount of residual aluminum, SO_4^{2-} or other ions from the coagulant can be a significant pollutant in purified water. [29, 93]Therefore, a novel magnetic coagulant with high settling-down performance and the low residue is needed.

Graphene oxide (GO) is a multifunctional material with large surface area,[94] which is now widely studied and used in waste, polluted, or natural water treatment as the filtration and settling material. With these functions, GO is an excellent adsorbent for removing ions and dyes in liquid[25, 95]. The GO nanosheets also have intense interaction with nano- and micro-particles in the aqueous solution due to its large surface, which foresees its potential use for the removal of insoluble suspended

solid.[18, 96] It was also reported that when GO was combined with the magnetic nanoparticles, the removal of the dye pollutants and arsenic ions can be significantly accelerated and improved in an external magnetic field.[28, 29] Thus, the nanocomposite of magnetic nanoparticles and GO nanosheets could possibly be used as a highly efficient magnetic coagulant in absorbing and removing solid suspension particles in the solution.[31, 97]

Herein, for the first time, we design and synthesize magnetic Fe_3O_4-GO and use it to remove suspended solid particles in the wastewater. The prepared Fe_3O_4-GO successfully shows a cohesive capacity for settling down suspended solids in water. With the existence of the external magnetic field, the suspended solids in water can be removed fast and efficiently with the addition of Fe_3O_4-GO nanocomposite, showing 90% removal efficiency within 30 minutes. The kinetic studies indicate the adsorption model can be fitted in both Langmuir and Freundlich equations and follows the pseudo-second-order kinetic model. These simulations prove the strong interaction between the nanocomposite and suspended particles and show a high initial adsorption rate reaching 0.0275 mg mg^{-1} min^{-1}. Thus, this work revealed that Fe_3O_4-GO has a great potential application in the rapid treatment of suspended solid particles in wastewater and natural water.

4.2 Experimental Section

Materials

The graphite powder (microcrystal grade) was obtained from Alfa Aesar. Sodium nitrite, sulfuric acid (98%), potassium permanganate, hydrogen peroxide and Kaolinite were obtained from Sigma Aldrich.

4.2.1 Synthesis of GO

The GO was synthesized by a modified Hummer method.[84, 85] To expand, 3.0 g of graphene powder and 1.5 g sodium nitrite (Sigma Aldrich) were mixed in the flask with 200 mL of 98 % sulfuric acid and stirred for approximately hour. Then, the flask was transferred into an ice bath and 9.0 g potassium permanganate was slowly added and vigorously stirred for 24 hours. Then, 500 mL of deionized water was added into the flask to avoid boiling while adding the water. Then the solution was heated to 35 °C, stirring for another 24 hours. During the stirring, the color of the aqueous solution turned to a dark brown color. 30 mL of hydrogen peroxide was then added to the solution, causing the color to change to a light shade of yellow. After two hours of continued stirring, the solid product was washed with 5 % hydrochloric acid, and deionized water for several times. The final product's color was dark brown. For characterization of the synthesized GO, the wet product was centrifuged, frozen with liquid nitrogen and finally freeze-dried for three days until the GO turned into light brown powder.

4.2.2 Synthesis of the Fe_3O_4-GO

The ratio of Fe_3O_4 to GO is determined by a series of experiment and listed in the Appendix. 1 g of the synthesized GO was ultrasonicated for 30 minutes and dispersed in 200 mL of distilled deionized (DDI) water. Ammonia solution (14 mL, 17%) was then added to the GO suspension solution stirred for two hours. In a separate beaker, 2.0g of $FeCl_2$ $4H_2O$ and 5.4g $FeCl_3$ $6H_2O$ were dissolved in 10 mL of DDI water and stirred until fully dissolved. The latter solution was added dropwise into the former solution, and the mixture was ultrasonicated for to avoid using any steel or magnetic stir bars. The homogenous solution was transferred into a Teflon-lined stainless-steel autoclave and heated at 80°C for 10 hours to form the Fe_3O_4 nanoparticles on the GO sheets. The final Fe_3O_4-GO suspension solution was washed with DDI, and centrifuge. Then the product was re-dispersed in DDI and used as the settling agent. To characterize the synthesized Fe_3O_4-GO, the product was centrifuged and freeze-dried. Following this step, a dark brown color powder was obtained.

4.2.3 Characterization

X-ray diffraction (XRD) patterns were obtained using a MiniFlex 600 diffractometer (Rigaku, Japan) equipped with Cu-Kα radiation ($\lambda = 0.154$nm) source at scanning speed of 2° min^{-1} in the range of 5 - 85°. The Raman spectroscopy was conducted with a Senterra Raman Microscopes (Bruker, US). X-ray photoelectron

spectroscopy (XPS) was measured using a Thermo Scientific K-Alpha spectrometer. The Fourier transform infrared (FT-IR) was obtained using Thermo scientific Nicolet 6700 spectroscopy. The morphology of the obtained samples was characterized by a LEO 1350 field emission scanning electron microscope (SEM). The nitrogen isothermal adsorption was carried out using a ASAP 2020 Plus accelerated surface area and porosimetry system. The visible light absorption was obtained by a Genesys 10s UV-Vis spectrophotometer.

4.2.4 Adsorption Experiments

Adsorption experiment were performed with 1 mL of 100 mg ml^{-1} Fe_3O_4-GO suspensions dropped into 20 mL of 40 mg ml^{-1} kaolinite suspension solution. After Fe_3O_4-GO was dropped into the kaolinite solution, the solution was ultrasonicated for ten minutes and then moved on to a magnet (20 mT) to begin the setting process in Vial 1. For comparison, Vial 2 with the same concentration of kaolinite and Fe_3O_4-GO nanocomposite and Vial 3 solely with kaolinite suspension were placed in a non-magnetic environment. Photos were taken throughout the settling process, and quantified adsorption analysis was performed by taking 0.5 mL of the solution from the upper portion of the vial after a series of settling times to analyze in a spectrophotometer. In each curve, the peak at 307 nm, which is the strongest peak, was used to measure the relative light absorption. The data of light adsorption was corrected and calibrated with the light adsorption data of standard solution to obtain

the concentration of each sample. The standard light adsorption-concentration line can be found in the appendix.

4.3 Results and Discussion

4.3.1 Materials and Characterization

To confirm the successful synthesis of Fe_3O_4-GO nanocomposite, its chemical composition and structure were investigated via X-ray photoelectron spectroscopy (XPS) and Fourier transform infrared spectroscopy (FTIR) in comparison with those of the GO powder. The appearance of iron peak at 710 eV in XPS survey (**Figure A1-1a**) discloses the existence of iron in the nanocomposite. The FT-IR spectrum and XPS O 1s spectrum of the nanocomposite in **Figure A1-1 a & b** both confirm the existence of Fe-O peak at 620 cm^{-1} and 530.4 eV, respectively.[98-100] This indicates the oxidized nature of iron within the nanocomposite. Moreover, the high-resolution XPS spectrum of Fe 2p in **Figure A1-1c** shows typical peaks for Fe $2p_{3/2}$ and Fe $2p_{1/2}$, located at 711.5 and 725.0 eV, respectively. The Fe $2p_{3/2}$ peak can be deconvoluted into four characteristic peaks, namely Fe^{2+} at 710.1 eV, Fe^{3+} at 711.2 eV, satellite peaks at 716.2 eV and 719.8 eV. [101] The co-existence of both oxidation states and an integrated area ratio of 2.14:1 for Fe^{3+} to Fe^{2+} indicate the formation of Fe_3O_4 in Fe_3O_4-GO.[27, 102]

On the other hand, the oxygen-contained functional groups on GO after the synthesis were also investigated via FTIR and XPS. According to the FTIR spectrum in **Figure 4-1a**, the peaks assigned to O-H stretch vibration (3150 cm^{-1}), C=O stretch vibration (1600 cm^{-1}), O-H bending vibration (1400 cm^{-1}) and C-O

stretch vibration (1080 cm^{-1}) are preserved in the nanocomposite after the hydrothermal reaction.[103] A new peak emerged at 1700 cm^{-1} in the spectrum of the nanocomposite is assigned to the ketone structure that was originated from the oxidation reaction of phenol and/or alcohol groups during the hydrothermal reaction in the presence of Fe^{3+}. Similarly, the high-resolution XPS spectrum of O 1s for the nanocomposite (**Figure 4-1b**) shows the increase of C=O species in comparison with that of GO in **Figure 4-1b**. Besides, the significant decrease of C-O-C peak and the increase of C-OH peak in the spectrum for the nanocomposite as opposed to those of GO imply the ring opening reaction of epoxide with water molecules during the hydrothermal reaction. The high-resolution C 1s XPS spectra of both the nanocomposite and GO powder (**Figure 4-1d & A1c**) also show the noted decrease of C-O-C species on the GO nanosheets.[104-106] Those C-OH and C=O groups generated on the GO nanosheets during the hydrothermal reaction (**Figure A1-1d**) could function as the extra anchor sites for iron ions via coordination and non-covalent interactions. This further enhances the *in-situ* deposition of Fe_3O_4 nanoparticles on the GO nanosheets.

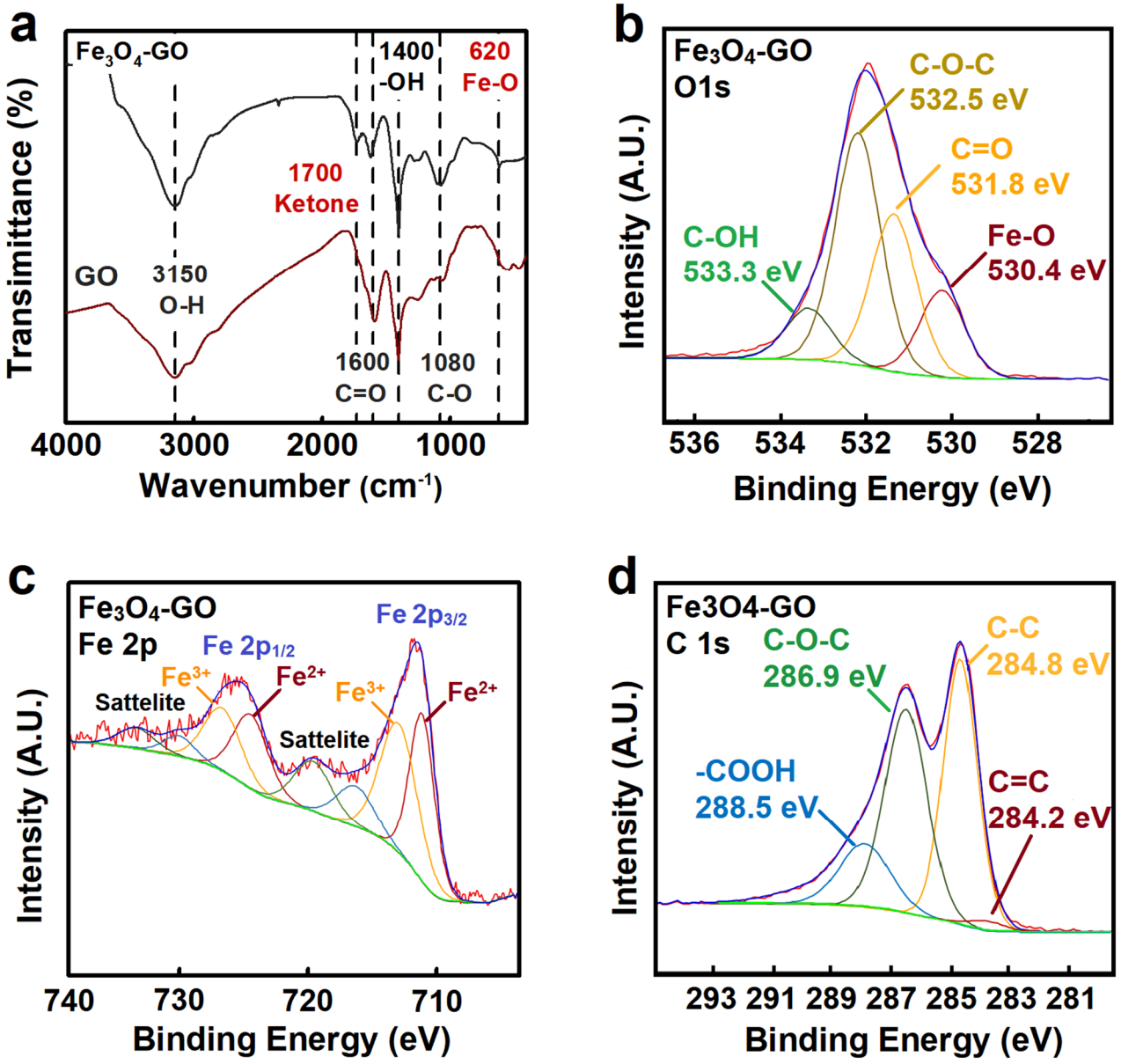

Figure 4-1 XPS spectra of Fe_3O_4-GO: (a) FTIR; (b) Fe 2p spectra of Fe_3O_4-GO; (c) C 1s spectra of Fe_3O_4-GO; (d) O1s spectra of Fe_3O_4-GO.

The crystal structures of Fe_3O_4-GO nanocomposite and GO powder were investigated by XRD patterns (**Figure 4-2a**) and Raman spectra (**Figure 4-2b**). As shown in **Figure 4-2a**, the typical peaks at 12° and 43° are assigned as (002) and (100) for GO powder.[107, 108] After the deposition of Fe_3O_4 nanoparticles, the (002) peak starts to diminish as the intense peaks for Fe_3O_4 appear. The XRD pattern of 10% Fe_3O_4-GO shows typical intense peaks at (220), (311), (422), (511) and (440), which are in agreement with XRD peaks for Fe_3O_4 in the literature.[109, 110] The crystal size of Fe_3O_4 can be estimated by the Scherrer **Equation 4-1**:

$$\tau = K\lambda/(\beta cos\,\theta) \qquad (\mathbf{4\text{-}1})$$

Where τ is the crystal size, K is the dimension factor, here is 0.89, λ is the wavelength of X-ray, β is the full width at half maximum (FWHM), and θ is the Bragg angle. Accordingly, the calculated average crystal size of the Fe_3O_4 nanoparticles in the nanocomposite of 10% Fe_3O_4-GO is 30 nm. The SEM images in **Figure 4-2c & 2d** present the morphologies of typical layered structure for GO powder and Fe_3O_4 nanoparticles decorated nanosheets structure for the nanocomposite, respectively. The average size of the observed Fe_3O_4 nanoparticles is also around 30 nm.

The Raman spectra of GO and Fe_3O_4-GO in **Figure 4-2b** both show the characteristic peaks for the structure of GO at 1346 cm^{-1} and 1585 cm^{-1}. They are assigned as the D-band for the disordered carbon in the graphene structure and the

G-band for the stretching vibration of sp^2 carbon domain in the GO.[111-113] The intensity ratio of D-band and G-band (I_D/I_G) indicates the degree of defects in the graphene structure.[114, 115] According to **Figure 4-2b**, with the deposition of Fe_3O_4 nanoparticles on the GO nanosheets, the value of I_D/I_G significantly increased, indicating more defects were introduced to the GO nanosheets after the hydrothermal reaction.[116, 117] This is in line with the increased oxygenated groups based on XPS analysis, telling that GO nanosheets were not reduced during the hydrothermal reaction. Additionally, a series of peaks ranging from 250 cm^{-1} to 700 cm^{-1} are the characteristic peaks of Fe_3O_4.[118] For instance, the peaks around 290 cm^{-1}, 540 cm^{-1}, and 670 cm^{-1} can be assigned to the E_g, T_{2g}, and A_{1g} vibrational modes for crystal lattice of Fe_3O_4, respectively.[119]

Both XRD pattern and Raman spectrum of the nanocomposite confirm the formation of Fe_3O_4 nanoparticles.

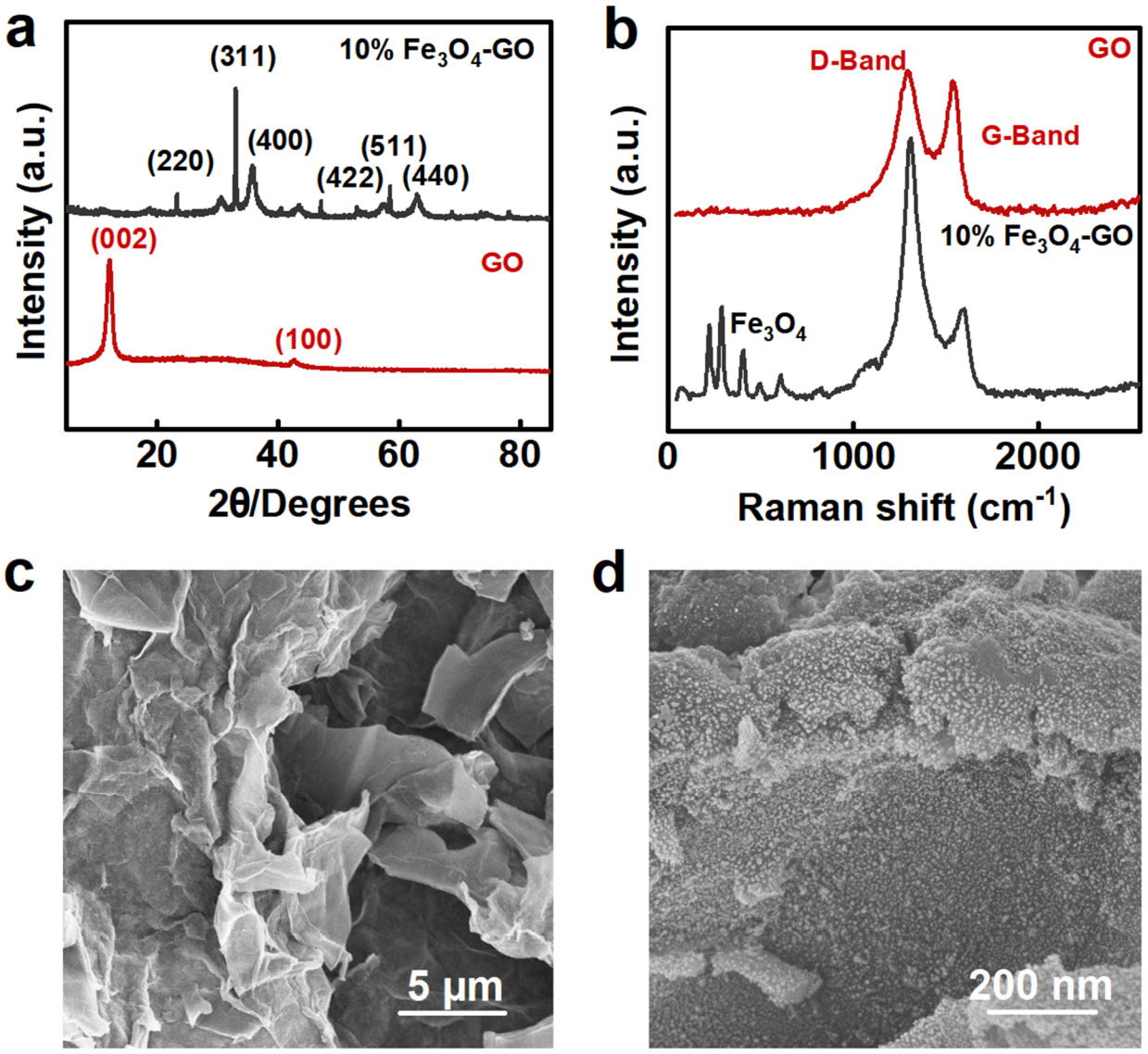

Figure 4-2 (a) XRD patterns of 10%Fe_3O_4-GO, 1% Fe_3O_4-GO and GO; SEM images of Fe_3O_4

-GO under (b) Raman spectrum of GO and Fe_3O_4-GO; SEM images of Fe_3O_4-GO at (c) lower magnification, and (d) higher magnification.

4.3.2 Adsorption Properties

To evaluate the capability of Fe_3O_4-GO nanocomposite as the coagulant agent, the kaolinite aqueous suspension is used to simulate the solid-suspended real wastewater in the settling experiments. As displayed in photos in **Figure 4-3a**, it can be clearly observed that kaolinite particles precipitated the fastest in the presence of Fe_3O_4-GO nanocomposite and the magnetic field. It only took 5 min to allow most solid particles, including kaolinite particles and the nanocomposite, settle on the bottom of the vial. After 60 minutes' experiment, the suspension solutions were nearly clear and transparent for Vial 1, still turbid it many suspended particles for Vial 2 and as milky as the initial suspension for Vial 3. Clearly, in the absence of a magnetic field, the co-settling capability of Fe_3O_4-GO with kaolinite suspension is insufficient. In other words, both Fe_3O_4-GO nanocomposite and magnetic field are necessary for efficiently and effectively coagulating solid suspension particles in the wastewater.

To further understand and quantify the settling process, the UV-Vis spectra of the suspension at different time were extracted and analyzed. As presented in **Figure 4-3b & c,** both suspensions with the Fe_3O_4-GO nanocomposites with or without the magnetic field show the distinct absorption peak at 307 nm for kaolinite particles. The peak intensity dramatically drops just after the addition of the Fe_3O_4-GO nanocomposite and continues decreasing in the presence of the magnetic field

(**Figure 4-3b**), which is in accordance with the color changes in the photos. Interestingly, in the absence of the magnetic field, the peak intensity also greatly decreased after the introduction of nanocomposite (**Figure 4-3c**). The contradiction between the UV-Vis spectra and the digital photos can be attributed to the strong absorption capability of Fe_3O_4-GO nanocomposite towards kaolinite particles. The kaolinite concentration could be further calculated according to the standard curve in **Figure A1-2** and the solid particle removal efficiency can be calculated using the following **Equation 4-2**:

$$\text{Removal Efficiency} = (C_0 - C_n)/C_0 \times 100\% \qquad (\mathbf{4\text{-}2})$$

Where c_0 is the initial concentration of kaolinite and c_n is the concentration of kaolinite after settling for the different time. Then, the kaolinite concentration and removal efficiency as functions of settling time are depicted in **Figure 4-3d & e**. The initial concentration and 0% removal efficiency at 0 minutes were added on each graph manually. The initial concentration and 0% removal efficiency at 0 minutes were added on each graph manually. At the initial stage (0-5 minutes), the plots show the quickly absorbing and settling down processes. Then, the absorbing process slows down and approaches to the equilibrium according to the insert plot of **Figure 4-3d**. As shown in the insert plot of **Figure 4-3e**, when 90% of the kaolinite particles were removed from the suspension in the presence of magnetic field, Fe_3O_4-GO nanocomposites took only one half of time that it required in the

absence of magnetic field (27 min *vs.* 55 min). Compared with several related magnetic flocculants and their removal rates listed in **Table A1-1,** the Fe_3O_4-GO reached a higher removal efficiency than most other magnetic flocculants.

Optimized mass ratio of Fe_3O_4 (10%) nanoparticles to GO is chosen for further kinetic study based on the removal efficiencies in **Figure A1-3**.

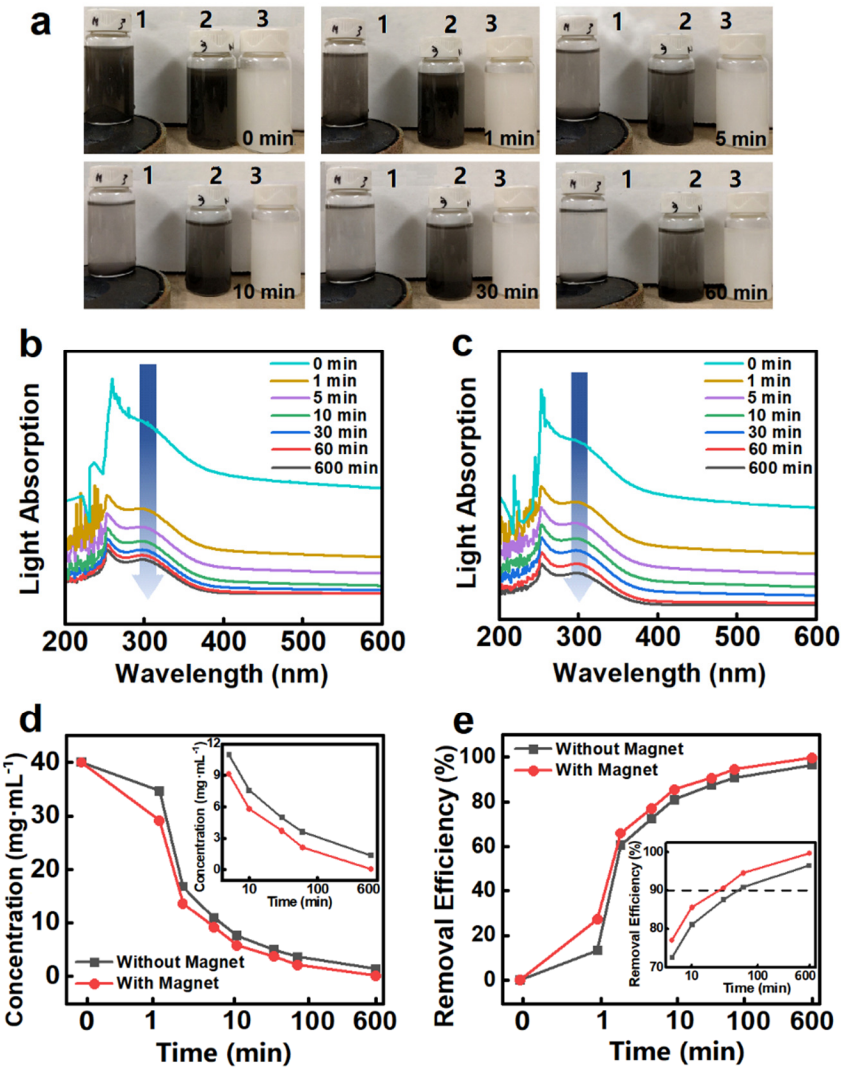

Figure 4-3 (a) Photos of vials containing 40 mg mL-1 kaolinite suspension taken after a settling time of 0 min, 1 min, 5 min, 10 min, 30 min, 60 min. (b) Light absorption of the upper-portion liquid from the 40 mg mL^{-1} kaolinite solution mixed with Fe_3O_4-GO after various settling times (b) with a magnet and (c) without a magnet. (d) The time-concentration and (e) removal efficiencies of kaolinite settling with Fe_3O_4-GO with/without a magnetic field, the inserted figure in each graph is the plot of 5-600 minute.

The kinetic behavior of the adsorption model in the presence of magnetic field is further analyzed by the Langmuir adsorption model and Freundlich's adsorption isotherm. The Langmuir adsorption model describes the adsorption happened on the surface site of absorbent in an ideal situation while Freundlich's adsorption isotherm describes the adsorption happened between the direct contact of the absorbent and adsorbate in a non-ideal situation.[43, 120] To determine the model parameters, the same amount of Fe_3O_4-GO (100 mg) was added to various concentrations (from 2.5 mg ml^{-1} to 40 mg ml^{-1}) of 20 ml kaolinite simulated solid suspensions, and the final equilibrium concentration was measured after 3 hours of settling until they reached near equilibrium, the upper layer of solution was used for analysis. The Langmuir model can be expressed as **Equation 4-3** and fitted in **Figure 4-4a**.

$$q_e = (abC_e)/(1 + bC_e) \quad \textbf{(4-3)}$$

The Freundlich equation can be expressed as **Equation 4-4**:

$$q_e = k(C_e)^{1/n} \quad \textbf{(4-4)}$$

Where the parameters in **Equation 4-3 & 4** are as follows: q_e is the amount of adsorbate absorbed by unit weight of absorbent (mg mg^{-1}), C_e is the equilibrium concentration of the adsorbate (mg ml^{-1}) when the upper layer reached near equilibrium after a long settling time, a is the maximum adsorption capacity (mg mg^{-1}) of absorbent, b is the Langmuir constant, which implies the interaction between the nanocomposite and suspended solids. k is the relative adsorption capacity of the

adsorbent (mg mg^{-1}) and *1/n* is the adsorption intensity. The Freundlich equation is fitted in **Figure 4-4b** and the fitted parameters are listed in the following **Table 4-1**.

Table 4-1 Fitting data of Langmuir and Freundlich Equation

Langmuir Equation		Freundlich Equation	
a (mg mg^{-1})	58.46	*k*	1.99617
b (ml mg^{-1})	20.29	*n*	0.02029
R^2	0.9998	R^2	0.99721

The fitted curve proved that the adsorption model can be fitted both with Langmuir and Freundlich Model, in which the Langmuir model fitted with a better R^2 value close to 1, the result indicates that the adsorbate interacted and bind on the surface sites of the absorbent. [28a] The Langmuir coO4nstant *b* is large enough to tell that the interaction between GO and the kaolinite particles are moderately strong, which is much stronger than reported weak interaction between absorbent and adsorbate.[24, 120, 121] Therefore, based to the above adsorption models, the Kaolinite particles were first absorbed on the surface of the F_3O_4-GO nanosheets, then the coagulated composites accelerate its settling down process driven by the magnetic field as shown in **Figure 4-4d**.

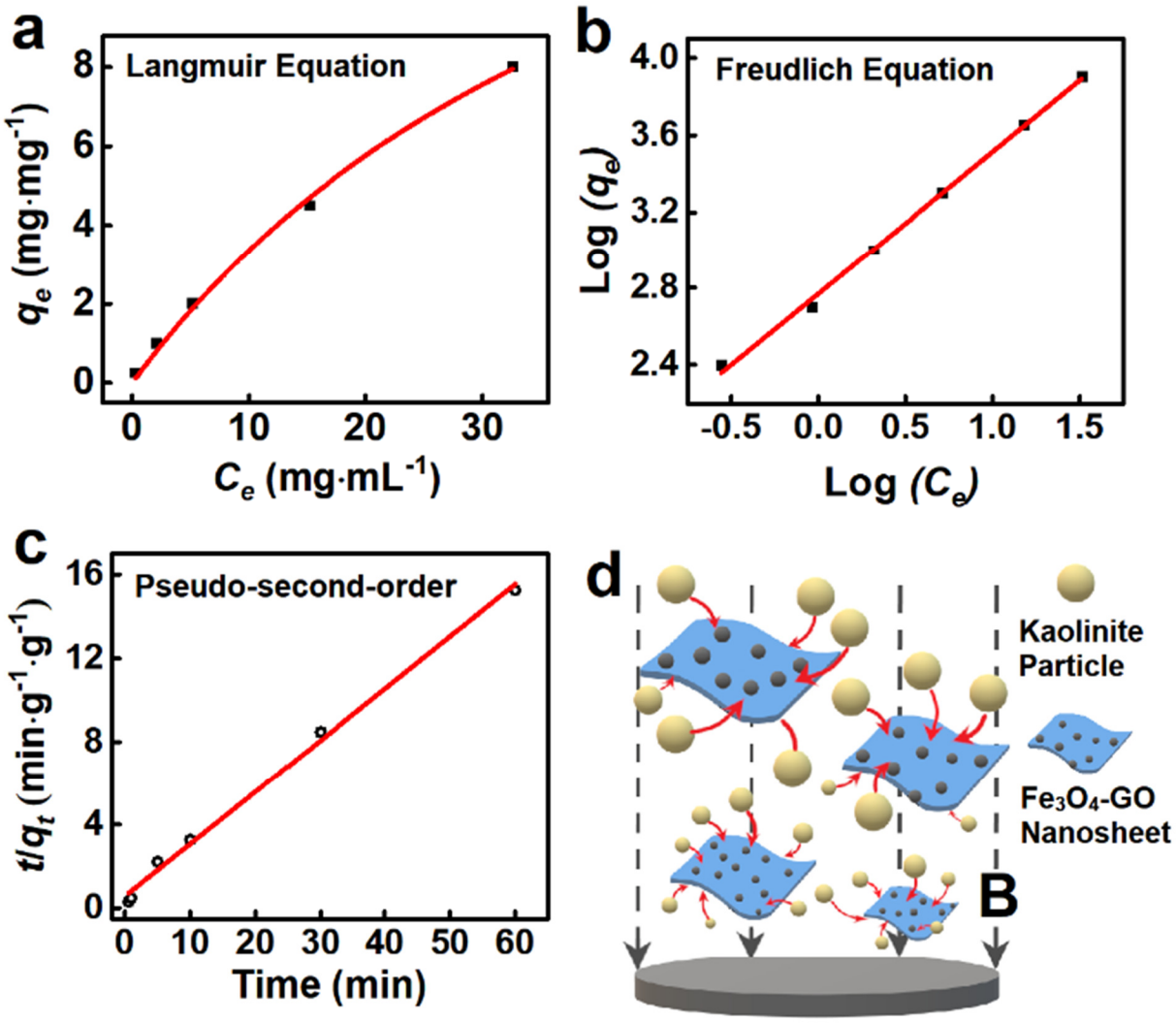

Figure 4-4 Plot of (a) C_e vs. q_e and the non-linear fitting using Langmuir equation; (b) Log(C_e) vs Log(q_e) and the linear fitting using Freundlich equation, (c) t/q_t vs. time and the linear fitting using pseudo-second-order kinetic model,(d) Interaction between absorbent and adsorbate.

The kinetics of adsorption was investigated by fitting the q_e parameter plotted against adsorption time with the samples taken during the settling down process of 40 mg ml^{-1} kaolinite solution, as shown in **Figure 4-4d**.[122, 123] Assuming chemisorption is the rate determining step, the kinetics were fitted into pseudo-second-order kinetic model using **Equation 4-5**, by integrating, the equation can be rearranged into linear equation as **Equation 4-6**:

$$(\mathrm{d}q_t)/\mathrm{d}t = k_2(q_e - q_t)^2 \qquad \textbf{(4-5)}$$

$$\mathrm{t/q}_t = k^2/{q_e}^2 + (1/q_e)t \qquad \textbf{(4-6)}$$

Where q_e is the adsorption capacity at equilibrium, q_t is the solid-phase loading of kaolinite and t is the time corresponding to q_t. The k_2 (ml mg^{-1} min^{-1}) is the rate constant for the kinetic model. V_0 (mg mg^{-1} min^{-1}) is the initial adsorption rate, which can be obtained from **Equation 4-7**:

$$V_0 = k_2{q_e}^2 \qquad \textbf{(4-7)}$$

The pseudo-second-order was linearly fitted with **Equation 4-7** with the obtained parameters listed in **Table 4-2**. The value of k_2=1.7111 indicates the kinetics of the adsorption process is more likely to follow the pseudo-second-order kinetic model.[122] The initial rate, V_0 =0.0275 mg mg^{-1} min^{-1} for the large particle absorbing is significantly faster compared to the reported initial rates for large particles absorbing.[124, 125]

Table 4- 2 Kinetics data of kaolinite adsorption with Fe_3O_4-GO in a magnetic field.

Kinetics Adsorption	
k_2	1.7111
q_e	0.3415
R^2	0.9959
V_0 (mg mg^{-1} min^{-1})	0.0275

4.4 Chapter Conclusions

This work reveals that the synthesized magnetic Fe_3O_4-GO can be used as a high-efficiency agent in rapid removing and settling down the solid suspensions in treating wastewater with an external magnetic field. The synthesized magnetic Fe_3O_4-GO requires a small amount added into the solid suspension solution and can reach nearly 90% removal rate within 30 minutes, with little residue in the treated water. The characterization and adsorption experiment indicate that the magnetic Fe_3O_4 components interacted with the external magnetic field while the GO attract the solid suspension particles in the solution, and finally accelerated the settling down process compared to the gravity settling process without magnetic. The adsorption test suggests the adsorption behavior follow both Langmuir and Freundlich model, with the adsorption capacity of 58.46 $mg \cdot mg^{-1}$. The test also suggests the kinetics of adsorption process follows the pseudo-second-order kinetic model with the initial rate V_0=0.0275 mg mg^{-1} min^{-1}. Overall, the results show a small amount of Fe_3O_4-GO exhibits a potential application in treating polluted water containing solid suspended particles.

Chapter 5: A 3D Ordered Hierarchical Porous Non-Carbon Electrode for Highly Effective and Efficient Capacitive Deionization

This section is published on *Journal of Material Chemistry A* and reprinted for this chapter with the permission from Royal Society of Chemistry. Supplemental information and unpublished preliminary experiments can be found in **Appendix B**.

5.1 Chapter Introduction

The freshwater crisis has become one of the most challenging and urgent global issues due to the growing human population and pollution levels.[1] The ideal solution to this issue is the development of sustainable desalination technology, which can treat abundant saline and brackish water.[126-128] Current technologies include distillation, reverse osmosis, and electrodialysis. However, these technologies suffer major drawbacks such as high energy consumption, high capital cost, and secondary pollution.[128] Alternatively, a highly efficient, low-cost, low energy-consumption, scalable and environmentally-benign desalination technology known as capacitive deionization (CDI) has emerged as a viable and promising solution over the last two decades. [129-132] CDI applies the principle of ion electrosorption to remove charged ions in low salinity solutions such as brackish water.[133] Due to its similarity to a supercapacitor,[16, 134] CDI electrode materials play

a pivotal role in the CDI performance. The majority of reported CDI electrodes are carbonaceous materials, from the earliest activated carbon (AC) electrode to the most recent carbon nanomaterial electrodes. [135-141] However, these carbonaceous CDI electrodes still suffer from low CDI performance, especially low salt adsorption capacity (SAC) and low salt adsorption rate (SAR).[133] Due to the strong dependence on electrostatic double-layer capacitance (EDLC) to remove ions from solution, the improvement of SAC for carbonaceous CDI electrodes will be limited. The lack of tuning pore structure for these hydrophobic carbonaceous electrodes causes inaccessible surfaces and unfavorable tortuous microporous channels for ions to diffuse, leading to the decrease of both SAC and SAR. Therefore, to further enhance the CDI performance for practical application, new ion adsorption mechanisms and fine tuning of the pore structure must be considered in a new strategy for the fabrication of the CDI electrodes.

In this work, a strategy of using a nanoengineered porous non-carbon electrode for CDI cell is proposed for the first time. As shown in **Figure 5-1,** the as-prepared 3D ordered mesoporous titanium nitride (3DOM-TiN) functions as the nanoengineered non-carbon electrode for high-performance CDI. Such a novel and rational design adapts the following advantages to maximize CDI performance (**Figure 5-1**): (i) the application of dual ion electrosorption mechanisms, namely EDLC and pseudocapacitance (PC), which significantly enhances SAC and SAR;

(ii) a well-designed ordered hierarchical porous structure together with high surface area and high pore volume, which effectively boosts the ion adsorption and decreases the ion diffusion resistance, hence maximizing both SAC and SAR; and, (iii) an interconnected nanoframework and nitrogen-doped carbon residual coating, which ensure high electric conductivity and fast charge transfer, hence further improving CDI performance. As a result, in a batch mode flow-by CDI cell, the 3DOM-TiN electrode delivers a high SAC of 23.6 mg g^{-1} and maximum SAR of 3.2 mg g^{-1} min^{-1} in 500 mg L^{-1} NaCl solution at an applied voltage of 1.2 V. Furthermore, it demonstrates a superior regeneration and cycling stability to that of AC electrode. The superior CDI performance of the 3DOM-TiN electrode not only provides a promising application in CDI but also highlights the effective strategy of employing nanoengineered non-carbon electrode designs for next-generation CDI devices.

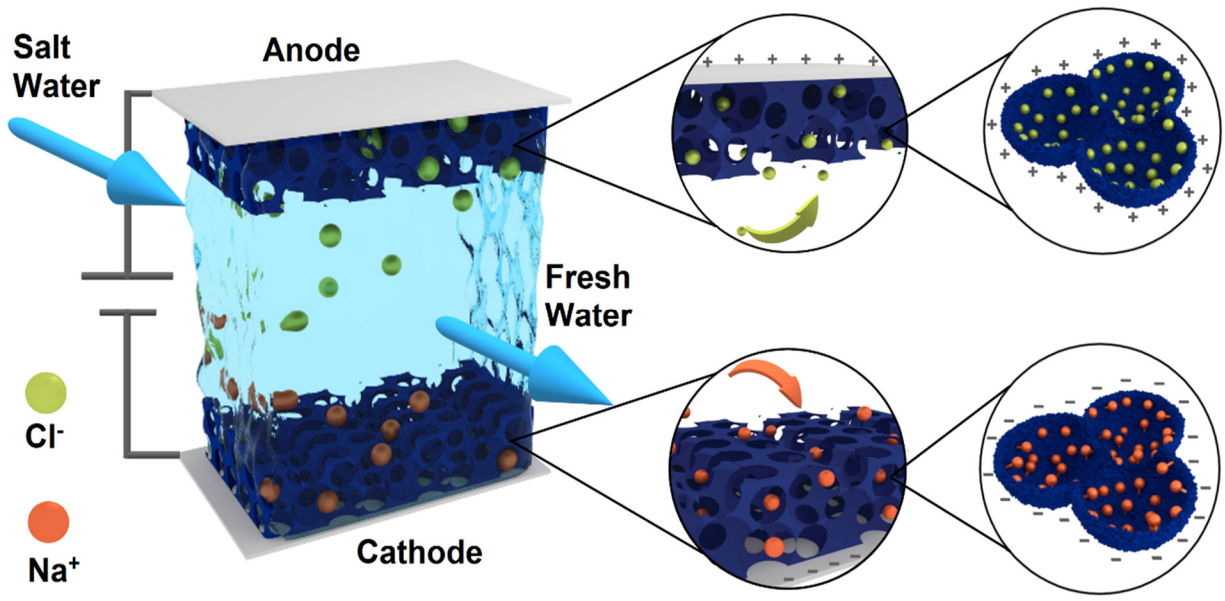

Figure 5-1 Schematic of 3D hierarchical ordered mesoporous titanium nitride as the electrode for capacitive deionization.

5.2 Experimental Section

5.2.1 Synthesis of polystyrene (PS) template

The synthesis procedure of the PS template is adapted from the literature.[86, 87] First, 2.5g polyvinylpyrrolidone (PVP, M.W. 10,000) was charged in a three-neck flask that contains 200 mL boiled distilled deionized water (oxygen-free DDI). After PVP was fully dissolved, the flask was placed in an oil bath with N_2 gas purging under the surface of the solution to expel the oxygen in the system. As the temperature was elevated to 70 °C for 15 min, styrene monomer (24 mL) was gradually added into the flask for 20 min with vigorous stirring and refluxing. Then, the potassium persulfate (40 mL, 5 mg mL^{-1}) was added dropwise into the mixture, and the emulsion polymerization was continued under an air-free atmosphere at 70°C for 24 h. The obtained PS template solution was centrifuged at 3000 rpm for 12 h to form ordered micro PS spheres and washed with DDI water. The ordered PS template was obtained after fully drying at 40°C overnight.

5.2.2 Synthesis of 3D Ordered Mesoporous Titanium Nitride (3DOM-TiN)

Titanium (IV) butoxide (TBOT, 97%, 10 mL), ethanol (>99%, 10 mL), and hydrochloric acid (37%, 2 mL) were mixed with a volume ratio of 5:5:1-and stirred for at least 30 mins. The PS templates (2 g) were then immersed in the solution for 1 hour, and the excess solution was filtered out through vacuum filtration. After

drying in ambient conditions overnight, the composite sample was loaded into a Lindberg tube furnace and subjected to sequential heat treatments at 300°C for 1 h and 540°C for 30 min under Ar atmosphere followed by 800°C for 1.5 h under NH_3 atmosphere. The ramp rate in between each stage was 1 °C min^{-1}. The 3DOM-TiN was obtained after the sample was cooled down to room temperature in Ar gas. For comparison, bulk-TiN was also synthesized following the above procedure without the addition of the PS template. The detailed synthesizing steps are listed in **Figure 5-2**.

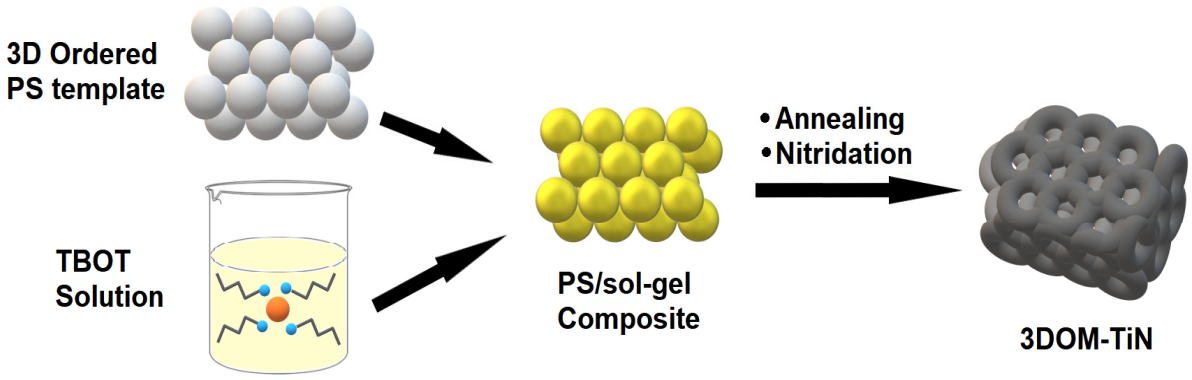

Figure 5-2 Synthesis process of 3DOM-TiN.

5.2.3 Physicochemical Characterization

X-ray diffraction (XRD) patterns were obtained using a MiniFlex600 diffractometer (Rigaku, Japan) equipped with Cu-Kα radiation (λ = 0.154nm) source at a scanning speed of 2° min^{-1} in the range of 5-90°. X-ray photoelectron spectroscopy (XPS) was measured using a Thermo Scientific K-Alpha spectrometer. The morphologies of the obtained samples was characterized by a LEO 1350 field emission scanning electron microscope (SEM). Transmission electron microscopy (TEM) images were obtained by a Philips CM10 Electron Microscope (60 to 100kV). The nitrogen adsorption-desorption isotherm was obtained using an ASAP 2020 accelerated surface area and porosity system to analyze the surface area and pore structure.

5.2.4 Electrochemical Characterization

Cyclic voltammetry measurements were carried out using NaCl solutions with concentrations of 0.1, 0.5, 0.8 and 1M. The sweep potential ranged from -0.6 to 0.6 V and the sweep rate ranged from 5 to 50 mV s^{-1} in an electrochemical cell with a three-electrode system including a graphite rod counter electrode, a saturated calomel reference electrode (SCE) and a glass carbon electrode coated with active materials as the working electrode. To further study and simulate the cathode and anode ion adsorption, the sweep potential range of -0.6 - 0 V and 0 - 0.6 V were adapted respectively, under the sweep rate range of 5 - 50 mV s^{-1} in 1 mol L^{-1} NaCl

solution. The experiment was conducted using an EC-lab SP-300 working station. The specific capacity of the prepared materials was calculated by integrating the area of the CV curve to determine the value using the following **Equation 5-1**:

$$C_s = \frac{\int IdV}{2v\Delta Vm} \qquad (\mathbf{5\text{-}1})$$

Where *Cs* is the specific capacitance (F g^{-1}), I is the current (A), v is the scan rate (mV s^{-1}), ΔV is the applied potential window (mV), and m is the electrode material mass (g). Electrochemical impedance spectroscopy (EIS) measurements were carried out at frequencies ranging from 100kHz to 1Hz. The amplitude of the alternating voltage was 10 mV and the direct current potential was 0 V vs open circuit potential.

5.2.5 CDI Cell Assembly and Electrosorption Experiment

The TiN electrode slurry was prepared with the following mass ratio, 3DOM-TiN: carbon (super P): polytetrafluoroethylene (PTFE) = 8:1:1. The working electrode was prepared by pressing the dried slurry into a 4 cm diameter, 3.0 mm thick round electrode and pressed onto the same size round stainless-steel metal mesh. For each piece electrode, the obtained mass was approximately 0.4 g on each side, and the surface area was 12.66 cm^2. The electrode attached on the stainless metal mesh was then attached to copper foil as the current collector, and the two electrodes were separated by glass fibers (Whatman, binder-free, Grade GF/C) to

assemble a CDI cell. The CDI performance of the batch mode test (**Figure 5-5a & b**) was obtained by measuring the conductivity of desalinated water using an Oakton CON 6+ conductivity meter. The calibration curve of conductivity to real-time salinity can be found in **Figure A2-11**. During the continuous mode of CDI testing (**Figure 5-5c, d & e**), the working conditions including potential voltages applied on the CDI cell, the concentration of the salt water, and flowrate were adjusted to reveal detailed desalination performance and behavior. The continuous salt concentration was measured by a VeraStat 3 electrochemical workstation and recalibrated with the results obtained by the Oakton CON 6+ conductivity meter.

The Salt Adsorption Capacity (SAC) is defined as the following **Equation 5-2**:

$$\mathrm{SAC} = \frac{(C_0 - C_e) \times V}{m} \qquad (\mathbf{5\text{-}2})$$

Where the C_0 is the initial concentration of the pumped in salt water, and C_e is the real-time concentration of the desalinated water. The maximum salt adsorption capacity is defined as the C_e at the lowest salt retention rate. m is the mass of active material in each electrode. The salt adsorption rate, SAR, is calculated using the following **Equation 5-3**:

$$\mathrm{SAR} = \mathrm{SAC}/t \qquad (\mathbf{5\text{-}3})$$

Where t is the time corresponding to the SAC during the CDI desalination process.

5.3 Result and Discussion

5.3.1 Physiochemical Characterization

As demonstrated by scanning electron microscopy (SEM) and transmission electron microscopy (TEM) images in **Figure 5-3a, b & A2-1**, the interconnected ordered hierarchical porous 3D nanostructure is obtained through such synthesis procedure. These images match with the BET analysis in **Figure 5-3c**, showing the ordered hollow macropores with a size of approximately 100 nm and the connecting mesopores with a size of 12.7 nm. The scattered nanoparticles and the rough pore walls in the magnified TEM images are related to the sol-gel and nitridation process. This process creates small mesopores of less than 10 nm for both 3DOM-TiN and bulk-TiN (**Figure 5-3c & A2-2**). The hierarchical macro-/mesoporous structure provides 3DOM-TiN with a high surface area of 141.6 $m^2 g^{-1}$, over four times larger than that of bulk-TiN (31.65 $m^2 g^{-1}$, **Table A2-1**) and significantly larger than the surface areas of previously reported TiN materials.[142, 143] This maximizes the electrolyte-electrode interfaces and improves the electrosorption capacity of Na^+ and Cl^- onto the electrode during the CDI process. Moreover, according to **Table A2-1**, the interconnected macro-pores also provide 3DOM-TiN with nearly ten times higher pore volume in comparison with that of bulk-TiN (0.291 $cm^3 g^{-1}$ vs. 0.030 $cm^3 g^{-1}$). This allows the absorption of bulk saline electrolyte into its structure, which will extend the electrolyte-electrode interface into 3DOM-TiN and minimize the ion

diffusion distance from bulk saline water to the electrode surface during the CDI process.

The successful nitridation of both 3DOM-TiN and bulk-TiN is confirmed in the X-ray diffraction (XRD) patterns (**Figure 5-3d**). The major peaks at 36°, 42°, 62°, 75°, and 80° are assigned to TiN crystal planes (111), (200), (220), (311), and (420), respectively. Despite the existence of the two minor rutile TiO_2 peaks, 3DOM-TiN shows much higher purity in comparison with bulk-TiN. The slight downshift of XRD peaks in the 3DOM-TiN as opposed to bulk-TiN further proves the higher degree of nitridation in 3DOM-TiN according to the calculation in **Table A2-2**.[144, 145] Such high purity and degree of nitridation are attributed to the 3D interconnected porous structure which allows high diffusion and thorough reaction with NH_3 during the nitridation process.

Both the energy-dispersive X-ray spectroscopy (EDX) results in **Figure A2-3**, and the X-ray photoelectron spectroscopy (XPS) survey in **Figure A2-4a** reveal the existence of O and C on the surface of 3DOM-TiN. In addition, according to the EDX map in **Figure A2-3c-e**, they are well distributed together with Ti and N. This indicates that surface oxidization and residual carbon coating from the removal of PS templates occur at the surface of 3DOM-TiN.[146] The surface oxidation of 3DOM-TiN occurs when it is exposed to air,[147] generating high oxidation state Ti species such as TiO_xN_y and TiO_2 on its surfaces according to the high-resolution Ti 2p, N

1s, and O 1s XPS spectra in **Figure 5-3e, f & A2-4b**. These Ti species with various oxidation states on the high surface area 3DOM-TiN potentially allow fast surface faradic reactions through the oxidation/reduction of these Ti species during the electrochemical charge and discharge processes.[148, 149] Also, these species can facilitate fast surface intercalation/deintercalation of sodium ions to enhance ion electrosorption capacity further .[150-152] The residual carbon coating from the PS template is found to be doped.

With nitrogen, mainly forming pyridinic nitrogen in the carbon structure (**Figure 5-3f & A2-4c**). Such nitrogen-doped carbon (NCR) coating can not only enhance the electronic conductivity of 3DOM-TiN to indirectly improve CDI performance, but also directly contribute potential extra SAC for 3DOM-TiN during the CDI process.[153, 154] Additionally, these oxygenated polar species on the surface of 3DOM-TiN shown in **Figure A2-4b** can form hydrogen bonds with water and hence enhance the wettability of the electrode and benefit the ion storage process in 3DOM-TiN.[155, 156]

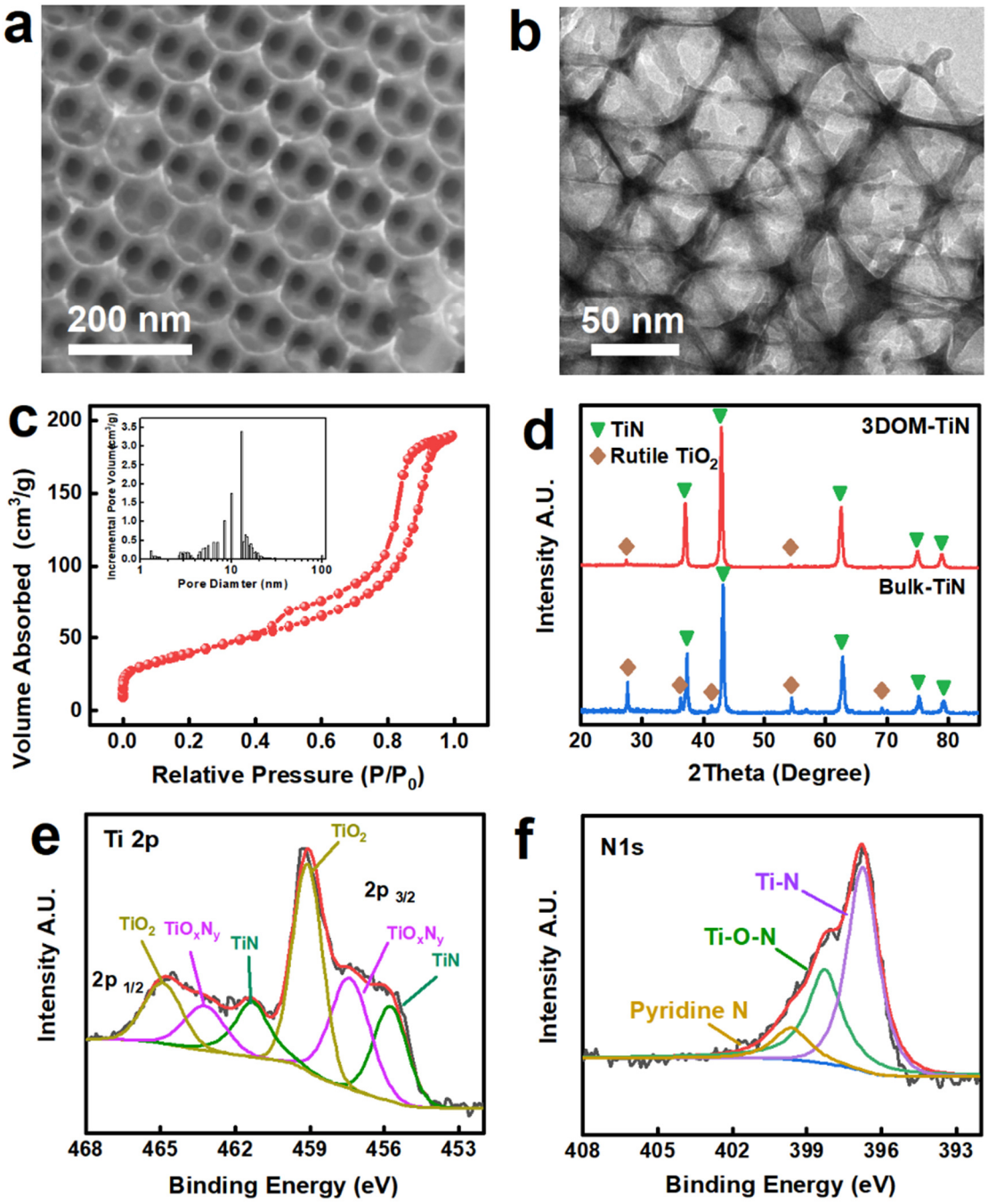

Figure 5-3 (a) SEM and (b) TEM images of 3DOM-TiN; (c) N_2 adsorption-desorption isotherm and associated pore size distribution of 3DOM-TiN; (d) XRD patterns of 3DOM-TiN and bulk-TiN; high resolution XPS spectra of (e) Ti 2p and (f) N1s.

5.3.2 Electrochemical Characterization

The electrosorption performance of the electrodes was firstly investigated via cyclic voltammetry (CV) in a typical three-electrode system in 1 mol L^{-1} NaCl aqueous solution, employing a saturated calomel electrode (SCE) and graphite rod as the reference electrode and the counter electrode, respectively. The CV curves of 3DOM-TiN, bulk-TiN, and AC electrodes in **Figure 5-4a** are all quasi-rectangular in shape, showing the considerable contribution of EDLC in all three electrodes. The additional distinct redox peaks located at –0.23 V vs. SCE in the CV curves of both 3DOM-TiN and bulk-TiN show the existence of pseudo-capacitance. Overall, the specific capacitance of the 3DOM-TiN electrode (142.9 $F \cdot g^{-1}$) is larger than that of the AC electrode (88.9 $F \cdot g^{-1}$) and the bulk-TiN electrode (45.4 $F \cdot g^{-1}$) at a scan rate of 50 mV s^{-1} (**Figure 5-4a**). The dramatic enhancement of the specific capacity of 3DOM-TiN electrode is strongly related to the increase of surface area brought by the 3D hierarchically-porous interconnected nanostructure, which increased the efficiency of utilizing the active sites and enhanced the ion diffusion from the electrolyte to the internal porous structure of the 3DOM-TiN [157, 158]. When varying scan rates are applied to the 3DOM-TiN electrode, the CV curves maintain the quasi-rectangular shape (**Figure 5-4b**), and the obtained specific capacitance can reach as high as 171.1 $F \cdot g^{-1}$ at 5 mV s^{-1} (**Figure 5-4c**). At every scan rate, the 3DOM-TiN electrode outperforms the AC and bulk-TiN electrodes with approximately 50% and

200% larger specific capacitance, respectively (**Figure 5-4c & A2-5**), thus predicting its superior electrosorption performance during the CDI process. The specific capacitance of 3DOM-TiN also increases with the concentration of NaCl (**Figure A2-6**) in the low electrolyte concentration range (0.1 – 1.0 mol L^{-1}). Furthermore, the 3DOM-TiN electrode demonstrates excellent stability, showing over 90% retention of its initial capacitance after 5000 cycles at a scan rate of 50 mV s^{-1} in 1.0 mol L^{-1} NaCl solution (**Figure 5-4d**), predicting its excellent stability in the CDI cell. Additionally, the high-resolution C1s XPS of 3DOM-TiN after cycling shows insignificant decease of sp^2 hybridized carbon (~ 4 %) and slightly increase of oxygenated carbon species and sp^2 hybridized carbon (**Figure A2-7**), indicating sufficient stability and resistivity to oxidation of the NCR-coating for CDI application.

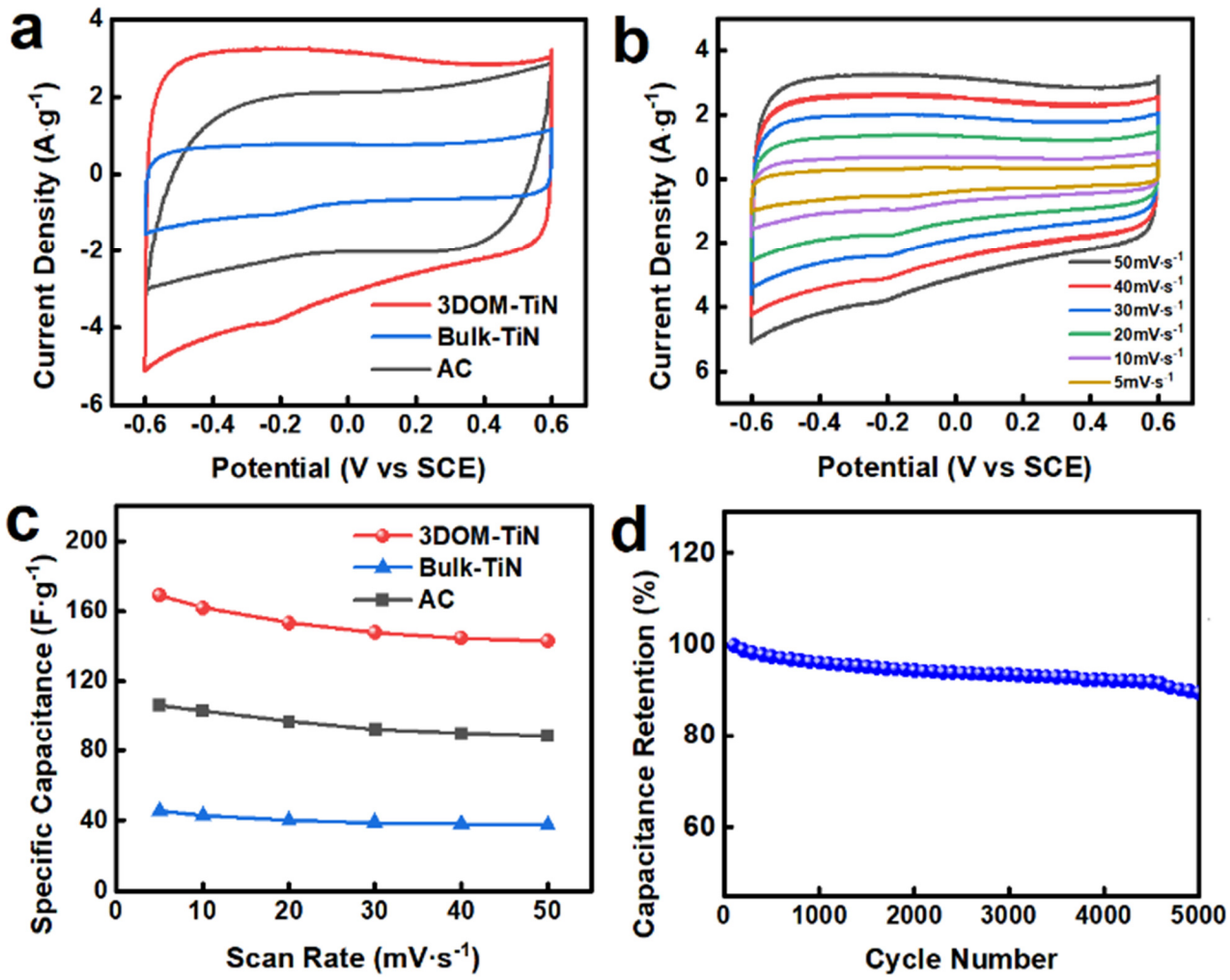

Figure 5-4 (a) CV curves of 3DOM-TiN, AC and bulk-TiN electrodes in 1.0 mol L^{-1} NaCl solution with a scan rate of 50 mV s^{-1}; (b) CV curves of 3DOM-TiN electrodes in 1.0 mol L^{-1} NaCl solution with various scan rates; (c) Specific capacitance of 3DOM-TiN, AC and bulk-TiN electrodes in 1.0 mol L^{-1} NaCl solution under different scan rates; (d) Cycling stability of the 3DOM-TiN electrode up to 5000 cycles.

To further understand the electrochemical properties and electrosorption behavior of the electrodes, electrochemical impedance spectroscopy (EIS) was conducted for both 3DOM-TiN and bulk-TiN electrodes. The Nyquist plots of both electrodes in **Figure 5-5a** show an incomplete semicircle in the high-frequency region and a steep straight line in the low-frequency region. The associated equivalent circuit model inserted in **Figure 5-5a** successfully accounted for the resistive and capacitive features of the electrodes.[159, 160] Both the smaller equivalent series resistance (R_s) as shown in **Figure A2-8a** (4.07 Ω) and the larger electronic conductivity (562.7 S m^{-1}) of 3DOM-TiN as shown in **Figure 5-5b** relative to bulk-TiN (8.69 Ω, 317.5 S m^{-1}) suggest an enhanced electronic transfer due to the interconnected 3D nanostructure and nitrogen-doped carbon residual coating within the 3DOM-TiN electrode. This inevitable NCR-coating will contribute to the CDI performance indirectly via the enhancement of electric conductivity. According to literature,[156, 159, 160] the two constant phase elements (CPEs), namely CPE1 and CPE2 are assigned to EDLC and PC, respectively. The charge transfer resistance (R_{ct}) is connected in series with CPE2 and mainly indicates the resistive behavior at the electrode-electrolyte interface occurring during the pseudocapacitive charge storage process. The observed lower R_{ct} of the 3DOM-TiN electrode as opposed to that of the bulk-TiN electrode (9.62 Ω vs. 17.61 Ω) (**Figure A2-8a**) reveals the fast kinetics of the Faradic reactions occurring at the highly-exposed accessible active sites on

the high surface area of the interconnected hierarchically-porous 3DOM-TiN electrode. It is also observed in **Figure 5-5a** that the linear straight line exhibited by 3DOM-TiN at the low-frequency region is steeper than that of the bulk-TiN electrode, implying faster ion diffusion in the 3DOM-TiN electrode. The calculated Warburg coefficient σ (Ω $s^{-0.5}$) in **Figure A2-8b** demonstrates that the ion diffusion resistance of 3DOM-TiN is only 12% of the value of that in the bulk-TiN electrode. These results prove that the 3D interconnected hierarchically-porous nanostructure enables fast ion diffusion from the electrolyte to the electrode, fast pseudocapacitive charge storage as well as the high electronic conductivity, thus giving the 3DOM-TiN electrode with high specific capacitance and great potential as a CDI electrode.

Investigations of the electrochemical behavior of 3DOM-TiN as both the anode and cathode were also conducted via CV measurement. As illustrated in **Figure 5-5c,** the 3DOM-TiN cathode delivers slightly higher specific capacity than the 3DOM-TiN anode at a scan rate of 10 mV s^{-1} (90.2 F g^{-1} *vs.* 66.5 F g^{-1}). Such difference between electrosorption towards the cation (Na^+) and anion (Cl^-) lies in the difference in sorption mechanisms of each specific ion.[161, 162] Nevertheless, **Figure 5-5c** indicates the 3DOM-TiN electrode has high electrosorption capacity towards both cations and anions, which is a desirable property for electrodes used in the symmetric design of CDI. To quantify the contribution of capacitive ion sorption mechanisms, Dunn's method is employed for the 3DOM-TiN electrode in the anodic

and cathodic ranges as well as the full potential range.[133, 159, 160] The calculation in **Figure A2-9** and the shaded areas in **Figure 5-5d** reveal that EDLC and PC contribute equally in the 3DOM-TiN cathode while EDLC dominates the electrosorption in the 3DOM-TiN anode (81.8%). Therefore, Cl^- is mainly adsorbed to the hierarchically-porous 3DOM-TiN electrode via the formation of EDL, which is in line with the literature.[148] Given the highly oxygen-deficient and reductive atmosphere during the nitridation process, large amount of oxygen vacancies (OVs) must be generated on the surface of 3DOM-TiN during ammonia heat treatment.[163] These OVs on TiN or hydrogenated TiO_2 have been reported to be responsible to their excellent pseudocapacitance via the oxidation/reduction of surface hydroxyl groups and OH^- ion adsorption in the chloride-free aqueous electrolyte.[150, 164-166] Therefore, it is assumed that the OVs on the surface of 3DOM-TiN can act as non-selective adsorbing sites towards anions in NaCl solution (Cl^-, OH^-, etc.) to contribute to the pseudocapacitance at the anode. On the other hand, Na^+ tends to be electro-adsorbed to the 3DOM-TiN electrode via the fast surface Faradaic reaction in addition to the EDL formation. This Faradaic Na^+ storage mechanism takes place at the interface between partially oxidized TiO_xN_y moieties and electrolyte via the oxidation/reduction of Ti during chemisorption or intercalation/deintercalation in the form of the following reaction.[148-150]

$$(TiO_xN_y)_{surface} + Na^+ + e^- \rightleftharpoons (TiO_xN_y^-Na^+)_{surface}$$

Therefore, the pseudocapacitive electrosorption of Na^+ accounts for the majority of PC in the 3DOM-TiN electrode in the full range (**Figure 5-5d**). As a result, the 3DOM-TiN electrode is proved to apply dual ion electrosorption mechanisms to store NaCl simultaneously, thus enabling efficient desalination in the CDI process. Such mechanism resembles the working principle of a hybrid system of battery and supercapacitor, such as lithium or sodium ion supercapacitor.[167, 168] In this case, Na^+ ions are stored at the electrode-electrolyte interface at the cathode via EDLC and PC, while the counter ions, Cl^- ions are mainly stored in the EDL to balance the charges and extra transferred electrons at the anode. The novel machanism will enable efficient desalination in the CDI process.

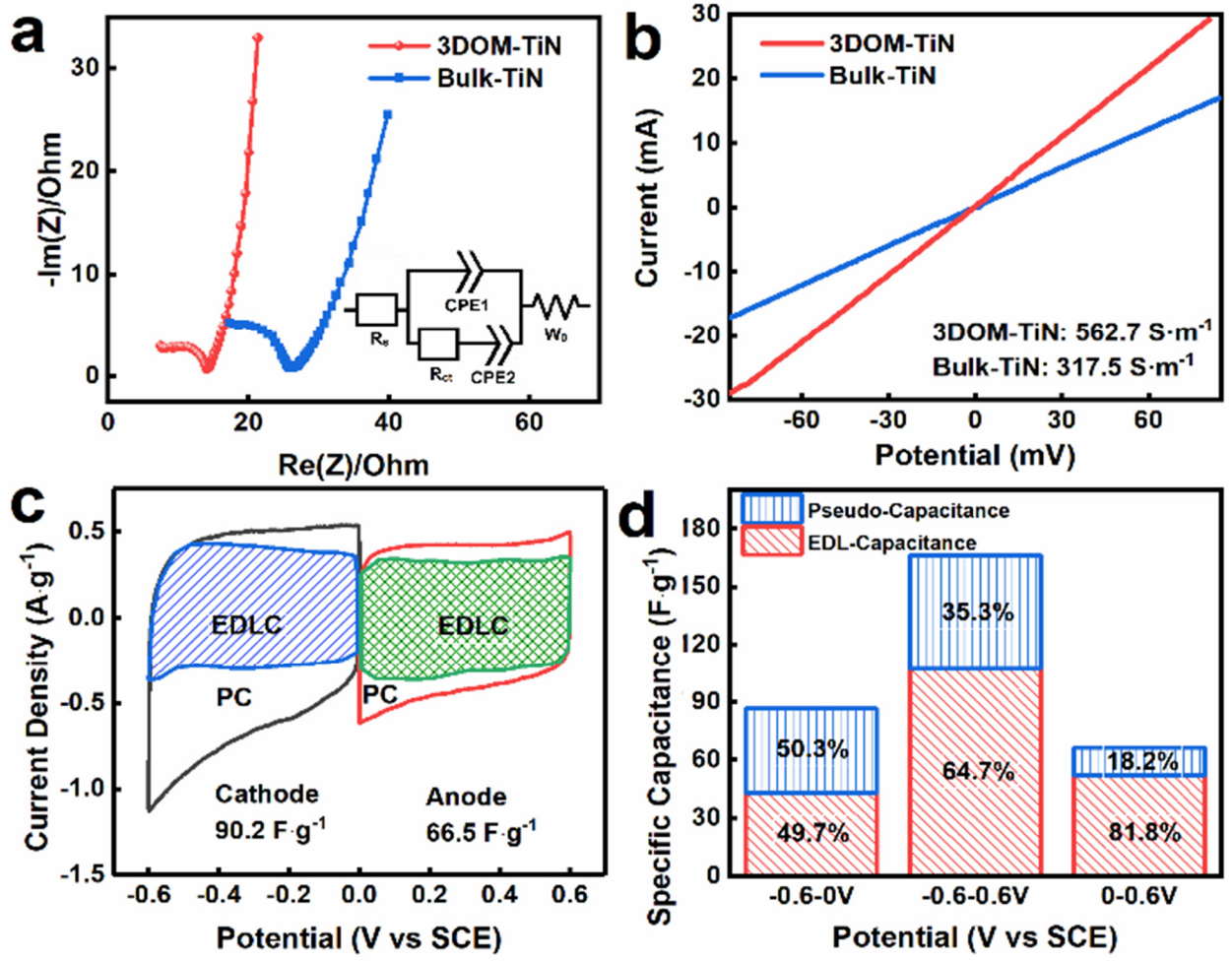

Figure 5-5 (a) Nyquist plot and the associated equivalent circuit derived for 3DOM-TiN and bulk-TiN; (b) Powder conductivity test of 3DOM-TiN and bulk-TiN; (c) Dunn method analysis of capacitance contribution of 3DOM-TiN anode and cathode at scan rate of 10 mV s^{-1} in 1 mol L^{-1}NaCl solution. The shaded regions show the current contributions from the electrical double-layer capacitive processes; and associate (d) EDLC and PC contribution to specific capacitance of the 3DOM-TiN electrode in cathodic, anodic and full range.

5.3.3 CDI Performance

The evaluation of CDI performance was conducted in a flow-by mode symmetrical CDI cell equipped with 3DOM-TiN, bulk-TiN or AC electrode. **Figure A2-10** compares the conductivity profiles of desalinated water against operation time for three electrodes in a full batch-mode CDI process under an applied voltage of 1.2 V with 100 mg g^{-1} NaCl solution pumped through the cell at a flow rate of 5ml min^{-1}. This shows that all three electrodes took roughly 25 minutes to reduce the solution conductivity to its minimum and then gradually reached a saturated adsorption state around 60 minutes. Correspondingly, the SAC of each electrode at different desalination times was calculated according to **Figure A2-10** and were plotted as a function of time in **Figure 5-6a**. 3DOM-TiN achieves the highest SAC among these three electrodes, specifically 22.1 mg g^{-1} at 60 min, which is roughly 4 times and 40% higher than the SAC of bulk-TiN and AC electrodes, respectively. Most importantly, such high SAC at low salinity ranks the 3DOM-TiN electrode at the top of the best previously reported titanium-based CDI electrodes (**Table A2-4**). To compare the desalination efficiency of the CDI electrodes, the SARs of three electrodes were calculated and plotted against SAC in the CDI Ragone plot in **Figure 5-6b**. The SAR increases quickly within the initial 10 min due to the rapid infusion of salt water and then decreases due to the gradual saturation of ion adsorption. Clearly, the 3DOM-TiN electrode shows the highest SAR among these three

samples, reaching a maximum SAR of 0.81 mg g^{-1} min^{-1} which is 2 times and 4 times higher than that of AC and bulk-TiN electrodes, respectively. Such effective and efficient CDI performance of the 3DOM-TiN electrode, showing both high capacity and high rate, is ideal for the CDI process.[169] The dramatic increase of CDI performance with respect to bulk-TiN is strongly related to the nanoengineered features of 3DOM-TiN. First, the high surface area of 3DOM-TiN exposes a large amount of accessible active sites at the electrode-electrolyte interface for dual capacitive deionization mechanisms,[141, 161] which greatly increases the SAC. Second, the 3D hierarchical porous structure and high pore volume reduce the ion diffusion resistance, which enhances the SAC and SAR simultaneously. Third, the interconnected nanoframework and nitrogen-doped carbon residual coating ensures the high electronic conductivity and efficient charge transfer, which further improves the total CDI performance. All these features together make the 3DOM-TiN a superior electrode material for CDI.

To further assess the potential of the 3DOM-TiN electrode for practical application to CDI, different operational parameters, namely cell voltage, salinity, and flow rate were conducted in the continuous CDI cell, with all desalination processes lasting until the lowest conductivity was reached. The obtained Ragone plots are displayed in **Figure 5-6c, d & A2-12**. Both SAC and SAR increase together with the applied voltage (**Figure 5-6c**), resulting from the thicker electrical double

layer and the stronger coulombic force under the more intense electric field.[170, 171] Similarly, the curve in **Figure 5-6d** shifts to the top-right of the CDI Ragone plot as the salinity of the solution increases, indicating the increase of both SAC and SAR at high salt concentration. When the continuous CDI cell is fed with a solution of 500 mg L^{-1} NaCl, the SAC further reached 23.6 mg g^{-1} at the saturated adsorption moment, with a maximum SAR of 3.2 mg g^{-1} min^{-1}. Such maximum SAR is the highest-ever reported value among all those obtained from carbon and non-carbon-based CDI electrodes (**Table A2-5 & A2-6**). The 3DOM-TiN electrode outperforms all recent reported titanium-containing CDI electrodes in terms of the combined performance of SAC and SAR in **Figure 5-6e**.[45, 51, 139, 156, 172-179] This excellent performance is attributed to two factors, the first being that a higher concentration of ions can enable the formation of a more coherent and denser EDL, and thus more pseudocapacitive ion adsorption and storage at the electrode-electrolyte interfaces.[141] Secondly, the interconnected hierarchical porous structure and high electronic conductivity of the 3DOM-TiN electrode lower the ion diffusion and charge transfer resistances even at high salinity, hence maximizing the SAR. When the flow rate is adjusted up to 15 ml min^{-1}, both the SAC and SAR of the 3DOM-TiN electrode are inferior to those obtained at lower flow rates as shown in **Figure A2-12**. This decrease could be attributed to the insufficient residence time of the ions in the CDI cell stemming from the high flow rate.[141]

Finally, salt adsorption-desorption cycling tests of the 3DOM-TiN electrode in the CDI cell were conducted to evaluate its stability during the CDI process. The regeneration curve in **Figure 5-6f** demonstrates the continuous and stable performance of over 600 minutes (10 cycles) under an applied potential of 1.2 V and feeding saline water of 100 mg L^{-1} NaCl at a flow rate of 5 mL min^{-1}. The SAC of the 3DOM-TiN electrode after cycling remains 15.3 mg g^{-1}, representing over 91% retention. It is significantly higher than the retention rate of the AC electrode (73.4%) after 600 minutes cycling (**Figure A2-13**). Therefore, the 3DOM-TiN electrode exhibited good and stable cycling and regeneration abilities. Such high CDI performance of the 3DOM-TiN electrode, especially its high SAC and SAR, demonstrates its promising application as a novel non-carbon CDI electrode for future large-scale desalination treatment of brackish water and seawater.

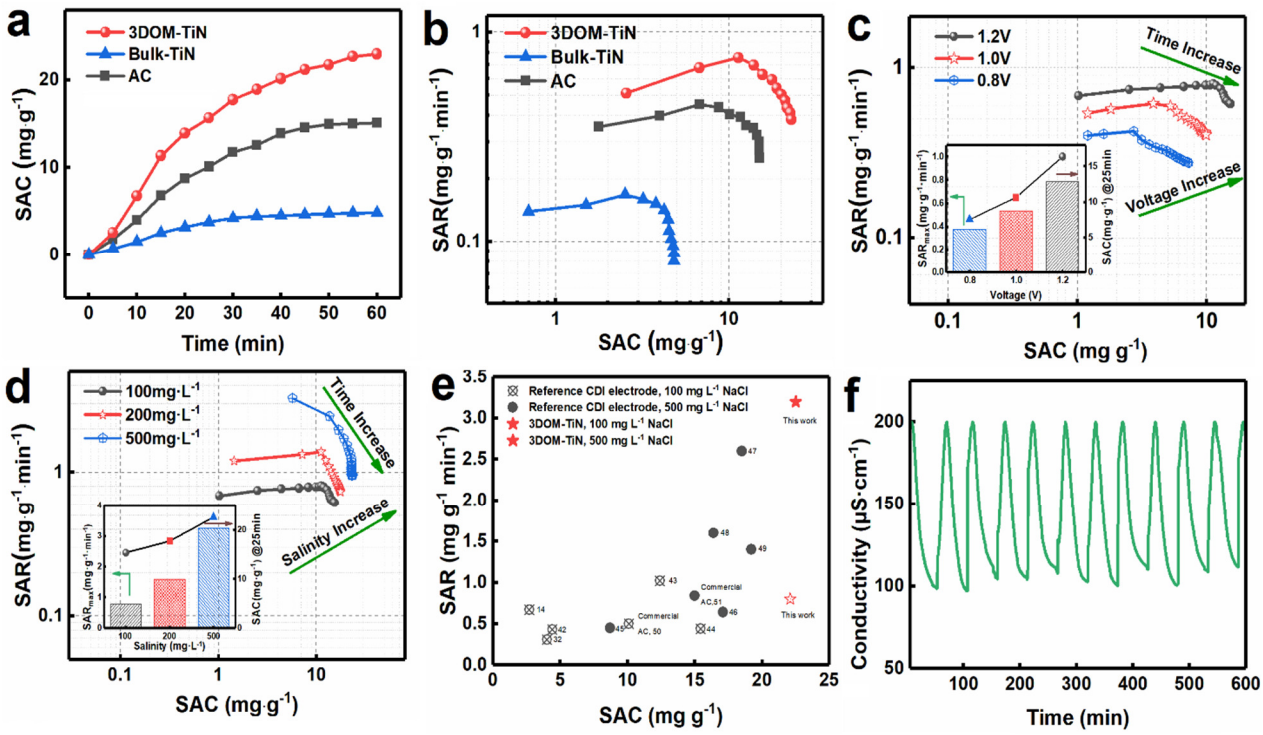

Figure 5-6 (a) SAC vs. time and (b) Ragone plot of SAR vs. SAC for 3DOM-TiN, bulk-TiN and AC electrodes obtained from batch-mode symmetric CDI cell; Ragone plots of SAR vs. SAC for 3DOM-TiN electrode in continuous symmetric CDI cell obtained under different operational parameters: (c) cell potential and (d) water salinity, the insert plots illustrate the maximum SAR and SAC at 25 min; (e) SAC and SAR comparison of 3DOM-TiN with recently-reported titanium-contained CDI electrodes; (f) Regeneration cycling stability test of 3DOM-TiN electrode in continuous symmetric CDI cell with saline water (100 mg L^{-1} NaCl) flow through at 5 ml min^{-1} at the applied voltage of 1.2 V.

5.4 Chapter Conclusions

In this work, we successfully synthesized 3DOM-TiN using a facile template method and fabricated it into electrodes for batch-mode symmetric CDI cells. The following distinct advantageous features were characterized: (i) The high specific capacitance as both anode and cathode, owing to both the cohesive electrical double layer formed at large accessible electrolyte-electrode interfaces and the fast surface pseudocapacitive reactions involving the bonding of Na^+; (ii) the well-designed hierarchical 3DOM structure together with high pore volume dramatically decreased the ion diffusion resistances from saline solution to the electrode; and, (iii) the interconnected nanoframework and nitrogen-doped carbon residue coating ensured the high electron conductivity and the low charge transfer resistance. All these features shaped 3DOM-TiN as promising electrode material in the CDI cell. The 3DOM-TiN electrode delivered an outstanding SAC as high as 23.6 mg g^{-1} and a record of high maximum SAR of 3.2 mg min^{-1} g^{-1} in a symmetric CDI cell fed by 500 mg L^{-1} NaCl solution. The superior CDI performance not only demonstrates the great potential of the 3DOM-TiN electrode for future CDI applications but also proposes a feasible and effective strategy of using nanoengineered porous non-carbon electrodes for next-generation CDI cells.

Chapter 6: Nitrogen-Doped Graphene-TiO_xN_y Nanocomposite Electrode for Highly Efficient Capacitive Deionization

This section is published on RSC Advances and reprinted. Supplemental information can be found in **Appendix C**.

6.1 Chapter Introduction

Obtaining fresh and clean water is one of the most urgent environmental problems in the 21st century.[1] An effective solution for increasing the fresh water supply is to develop sustainable desalination technology, which can treat brackish and saline water.[8] However, traditional water desalination techniques including distillation, reverse osmosis, and vacuum evaporation are approaching their limitations as they require high operating temperature, huge energy consumption, and large capital cost.[128] Alternatively, capacitive deionization (CDI) method has become as one of the most promising solutions for water desalination,[180] which works by separating and adsorbing ions on each electrode. It has the advantageous nature of high efficiency, low cost, low energy-consumption, ambient atmosphere operation, and environmental-benignity.[10] The electrode material in a CDI cell plays a pivotal role in determining the desalination performance.[181] Currently, most reported and commercialized CDI electrode materials are based on various kinds of novel porous carbon electrodes. [182-189]

Graphene, as the novel two-dimensional carbon nanomaterials, has been widely used as the electrode materials in batteries and supercapacitors due to its high electrochemical performance and large surface area.[190-195] Its heteroatom-doped derivative, especially nitrogen-doped graphene (NG), has also been investigated as electrode materials to achieve even better electrochemical performance in batteries and supercapacitors as opposed to graphene due to nitrogen-doped active sites and enhanced electrical conductivity.[196, 197] It is also worth to notice that it is reported that by nitrogen doping, the NG achieved significantly high adsorption capacity in CDI test.[198-203] On the other hand, TiO_xN_y and/or TiN can be fabricated into nanomaterials and used as electrodes materials in batteries and supercapacitors with enhanced electrochemical performance and wettability.[146, 204, 205] Additionally, with various morphologies, various Ti species and excellent electrical performance, TiN and/or TiO_xN_y can be used as additives to enhance the performance of graphene nanosheets by forming nanocomposites.[156, 206] Moreover, our previous research disclosed that the porous TiN/TiO_xN_y had shown excellent performance as the CDI electrode material.[207] However, there is no reported nanocomposites of NG and TiO_xN_y that have been synthesized and used as CDI electrode materials. Therefore, it is highly promising to prepare this kind of hybrid material and investigate its potential performance in CDI devices for water desalination.

In this study, a first-ever reported nanocomposite electrode of nitrogen-doped graphene-titanium oxynitride (NG-TiO_xN_y) was synthesized via the hydrothermal reaction and high-temperature nitridation process and then tested for CDI. The physiochemical characterization results demonstrated the successful formation of nitrogen-doped-sites on the graphene nanosheets and the TiO_xN_y nanoparticles embedded on the graphene nanosheets. The multi-layered graphene structure and TiO_xN_y nanoparticles allowed the saline water stream to pass through and facilitates a fast ion diffusion process to form the electrical double layer (EDL) at the electrolyte-electrode interface of both the graphene layers and TiO_xN_y nanoparticles. As a result, the NG-TiO_xN_y electrode delivered a significantly higher salt removal efficiency than the commercial AC, pure rGO and rGO-TiO_2 electrodes in single-pass CDI test. (**Figure 6-1**) Furthermore, the electrode reached a maximum salt adsorption capacity of 26.1 mg g^{-1} in 500 mg L^{-1} feed in saline water. The electrode material also exhibited great regeneration capacity and long-life cycling stability. The overall superior results demonstrated that the NG-TiO_xN_y could be an ideal CDI electrode material candidate. [156]

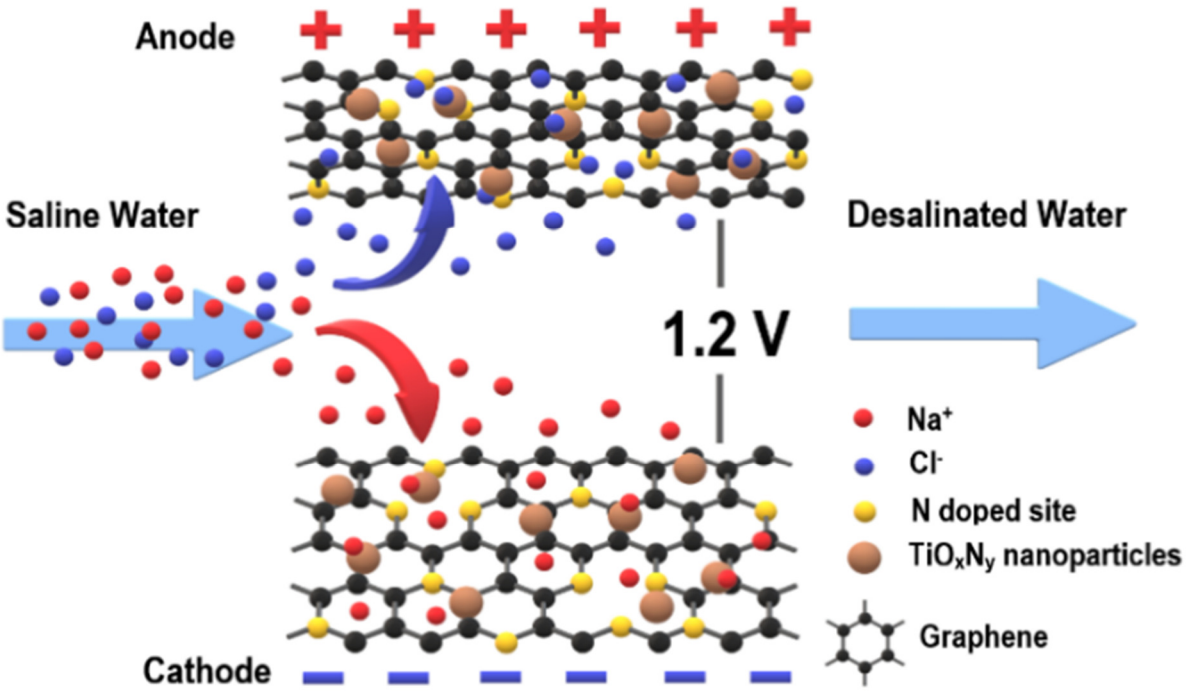

Figure 6-1 Schematic of a flow-by CDI cell using NG-TiO_xN_y electrodes.

6.2 Experiment Section

6.2.1 Synthesis of TiO_2 nanoparticles

The synthesis procedure of the polystyrene (PS) nanosphere is adapted from the literature.[86] First, 2.5g polyvinylpyrrolidone (PVP, M.W. 10,000) was charged in a three-neck flask that contains 200 mL boiled distilled deionized water (oxygen-free DDI). After PVP was fully dissolved, the flask was placed in an oil bath with N_2 gas purging under the surface of the solution to expel the oxygen in the system. As the temperature was elevated to 70 °C for 15 min, styrene monomer (24 mL) was gradually added into the flask for 20 min with vigorous stirring and refluxing. Then, the potassium persulfate (40 mL, 5 mg mL^{-1}) was dropwise added into the mixture, and the emulsion polymerization was continued under an air-free atmosphere at 70°C for 24 h. The PS emulsion was centrifuged and washed with DDI water for several times. Then, after 3 days' freeze-drying, the PS nanospheres were obtained.

Titanium (IV) butoxide (TBOT, 97%, 10 mL), ethanol (>99%, 10 mL), and hydrochloric acid (37%, 2 mL) were mixed with a volume ratio of 5:5:1 and stirred for at least 30 mins. Meanwhile, 2 grams of the PS nanosphere was sonicated and re-dispersed in 20 mL ethanol. The PS nanosphere ethanol dispersion was then added into the TBOT solution and the mixture was sonicated until it turns light yellow after 30 mins.[52, 208, 209] After drying the sol-gel in ambient conditions overnight, the composite sample was loaded into a tube furnace and subjected to

sequential heat treatments at 300ºC for 1 h and 540ºC for 30 min under Ar atmosphere to form the TiO_2 nanoparticles.

6.2.2 Synthesis of NG-TiO_xN_y

The graphene oxide (GO) was synthesized via a typical modified Hummer's method.[210] Based on a series of preliminary experiment with a different initial mass ratio of rGO: TiO_2 before the ammonia treatment, see in the CDI performance section, GO and TiO_2 powders with a mass ratio of 2:1 were mixed for further characterization. In this study, the specific masses of GO and TiO_2 were 1.0 and 0.5 g, respectively. GO, and TiO_2 were mixed in a beaker with 400 mL DDI water and thoroughly stirred for over 24 hours. Then, the mixed solution was sealed in an autoclave and hydrothermally treated for 12 h at 180 °C. The hydrotreated product was then centrifuged at 2500 rpm and separated from the solution. Subsequently, the product was washed by DDI water and centrifuged several times. The obtained product was then oven dried at 60 °C for 12 h, and then transferred to a vacuum oven and fully dried. Thus, in this step, GO was reduced to rGO.[211] For comparison, the rGO-TiO_2 was synthesized with the same procedure without ammonia annealing.

The dried composite was transferred to a ceramic boat and was subjected to heat treatment from room temperature to 800 °C for 10 h, under argon flow, after reaching 800 °C, the argon flow was switched to ammonia, and the temperature was

kept at 800 °C for 1 h for nitrogen doping and TiO_2 nitridation. Then, the sample was cooled down until room temperature in argon.

6.2.3 Physicochemical and Electrochemical Characterization

The crystal structure property of the electrode material was characterized by X-ray diffraction (XRD, RIETVELDXRG 3000) and the chemical composition was characterized by X-ray photoelectron spectroscopy (XPS, Thermo Scientific K-Alpha spectrometer) at University of Waterloo. Sample morphology was examined using scanning electron microscopy (SEM, ZEISS ULTRA PLUS), and transmission electron microscopy (TEM, Carl Zeiss Libra 200MC STEM).

The crystallite size was calculated according to the Scherrer equation, given in **Equation 6-1**:

$$\tau = \frac{K\lambda}{\beta cos\theta} \qquad (\mathbf{6\text{-}1})$$

Where, τ is the dimension of the crystallites, which is smaller or equal to the grain size; K is a dimensionless shape factor, approximately 0.89; λ = is the wavelength of X-ray, which is 1.54060 Å and K is 0.9. β is the line broadening at half the maximum intensity; and θ is the Bragg angle.

Cyclic voltammetry (CV) measurements were employed for evaluating the electrochemical performance of the CDI electrode and its adsorption/desorption capacity. The CV experiment was performed in a three-electrode system, which

employed a carbon electrode as the counter electrode and a saturated calomel electrode (SCE) as the reference electrode in the NaCl electrolyte solution. Reversible Hydrogen Electrode (RHE) were used to calibrate the SCE electrode in a pH=7 NaCl solution, as shown in **Figure A3-1** in the supplementary information. The actual potential was calibrated by +0.5V to the original value, where the potential range from -1 V to 0 V is corresponded to the actual potential range of -0.5 V to 0.5 V, representing both the cathode and anode adsorption processes. The experiment was conducted using an EC-lab SP-300 working station under the sweep rate range of 5 - 50 mV s^{-1} in 1 mol L^{-1} NaCl solution. The value of specific capacity of the prepared materials was calculated by integrating the area of the CV curve, using **Equation 6-2**:

$$C_s = \frac{\int IdV}{2v\Delta Vm} \qquad (\mathbf{6\text{-}2})$$

Where *Cs* is the specific capacitance (F g^{-1}), *I* is the current (A), *v* is the scan rate (mV s^{-1}), Δv is the applied potential window (mV), and *m* is the electrode material mass (g). Electrochemical impedance spectroscopy (EIS) measurements were carried out at frequencies ranging from 100kHz to 1Hz. The amplitude of the alternating voltage was 10 mV, and the direct current potential was 0 V vs. open circuit potential.

6.2.4 CDI Test

The synthesized NG-TiO_xN_y electrode material was mixed with PTFE and conductivity carbon (super P) with a mass ratio of 8:1:1. The electrode material was dried in a vacuum oven and pressed on metal mesh with copper current collectors. Each plate had an effective surface area of 4 cm^2 and was separated by glass fiber with 5 mm space. Saline water with the salinity of 100~500 mg L^{-1} was fed into the cell by a peristaltic pump (Baoding Lange) and passed between two electrodes under the flowrate from 10~30 ml min^{-1}, and the potential from 0.8~1.2 V applied on each side. The salinity of the outflow water was measured by a CON6+ conductivity meter, and the raw data was converted into salinity using the calibration curve in **Figure A3-2**. The salt removal efficiency is calculated using the following **Equation 6-3**:

$$\eta = \frac{C_e}{C_{out}} \times 100\% \qquad (\mathbf{6\text{-}3})$$

The salt adsorption capacity (SAC) was obtained using **Equation 6-4**:

$$\mathrm{SAC} = \frac{(C_0 - C_e) \times V}{m} \qquad (\mathbf{6\text{-}4})$$

Where the C_0 is the initial concentration of the saline water, and C_e is the real-time concentration of the desalinated water. The maximum salt adsorption capacity

is defined as the C_e at the lowest salt removal efficiency, m is the total mass of the electrodes and V is the real-time total saline water volume.

The salt adsorption rate (SAR) was calculated using **Equation 6-5**:

$$\mathrm{SAR} = \mathrm{SAC}/t \qquad (\mathbf{6\text{-}5})$$

Where t is the time corresponding to the SAC during the CDI desalination process.

6.3 Results and Discussion

6.3.1 Physiochemical Characterization

The XRD patterns of the synthesized NG-TiO_xN_y, rGO-TiO_2, and rGO are shown in **Figure 6-2a**. For both NG-TiO_xN_y and rGO-TiO_2, the main (101) peak at 25° and minor (200), (215) peaks at 48° and 75° can be assigned to the anatase-phase TiO_2 (JCPDS no. 21-1272), respectively. The peaks at 31°, 54°, 56°, can be assigned crystal planes (121), (211), (123) to the rutile-phase TiO_2 (JCPDS no.46-1238). Both the presence of anatase-TiO_2 and rutile-TiO_2 are confirmed in the rGO-TiO_2 synthesized via hydrothermal method. The peaks of 36°, 42°, and 62° are assigned to TiO_xN_y crystal planes (111), (200), (220), demonstrated the successful nitridation of rGO-TiO_2 after ammonia annealing. The upshift of the characteristic peaks in the XRD patterns of the TiO_xN_y as opposed to TiN (JCPDS: 38-1420, **Figure A3-3**) indicated the presence of the oxynitride.[144, 145, 212] The XRD results prove the presence of various Ti species, including both the anatase-phase and rutile TiO_2 and the existence of TiO_xN_y crystal phase. Based on previous reports, both anatase and rutile phase TiO_2 can have a positive effect on increasing the ion adsorption by increasing the wettability and forming a more cohesive EDL.[52, 174, 213] The calculated average size of the TiO_xN_y nanoparticles was 43 nm. Such small size of nanoparticles can potentially provided more active sites for ion absorbing and forming the EDL on the surface of the nanoparticles.[213, 214]

The BET analysis (**Figure 6-2b**) shows a typical type IV isotherm curve, further confirmed the existence of the mesoporous structure with the pore distribution around 18 nm. Compare with the rGO-TiO_2 (**Table A3-1**). The nitrogen doping process dramatically increased the BET surface area and the pore volume. The increase of the BET surface area is attributed to the loaded TiO_xN_y nanoparticles with small crystal size and could be further explained by the surface vacancies generated during the ammonia heat treatment[163, 215] , which may result in a positive effect on ion absorbing.

The SEM images in **Figure A3-4** at 1 μm magnitude indicated the layered structure of the graphene nanosheet. The layered nanosheets provide a relatively large surface area for interaction between liquid and solid as well as enough space for the saline water to pass through and assisted the ion diffusion process. **Figure 6-2c** shows the TiO_xN_y nanoparticles attached to the graphene nanosheet layer. The TiO_xN_y nanoparticles provides the space for the formation of cohesive electrical double layer for ion absorbing. **Figure 6-2d** is the TEM image of the synthesized NG-TiO_xN_y, which indicates the layered nanosheets of the graphene. Furthermore, the TiO_xN_y nanoparticles embedded on graphene the layer further allows the absorption of saline water into the electrode structure, which extends the electrolyte-electrode interface into NG-TiO_xN_y and minimized the distance of ion diffusion between saline water and the electrode surface during the electrosoprtion process.

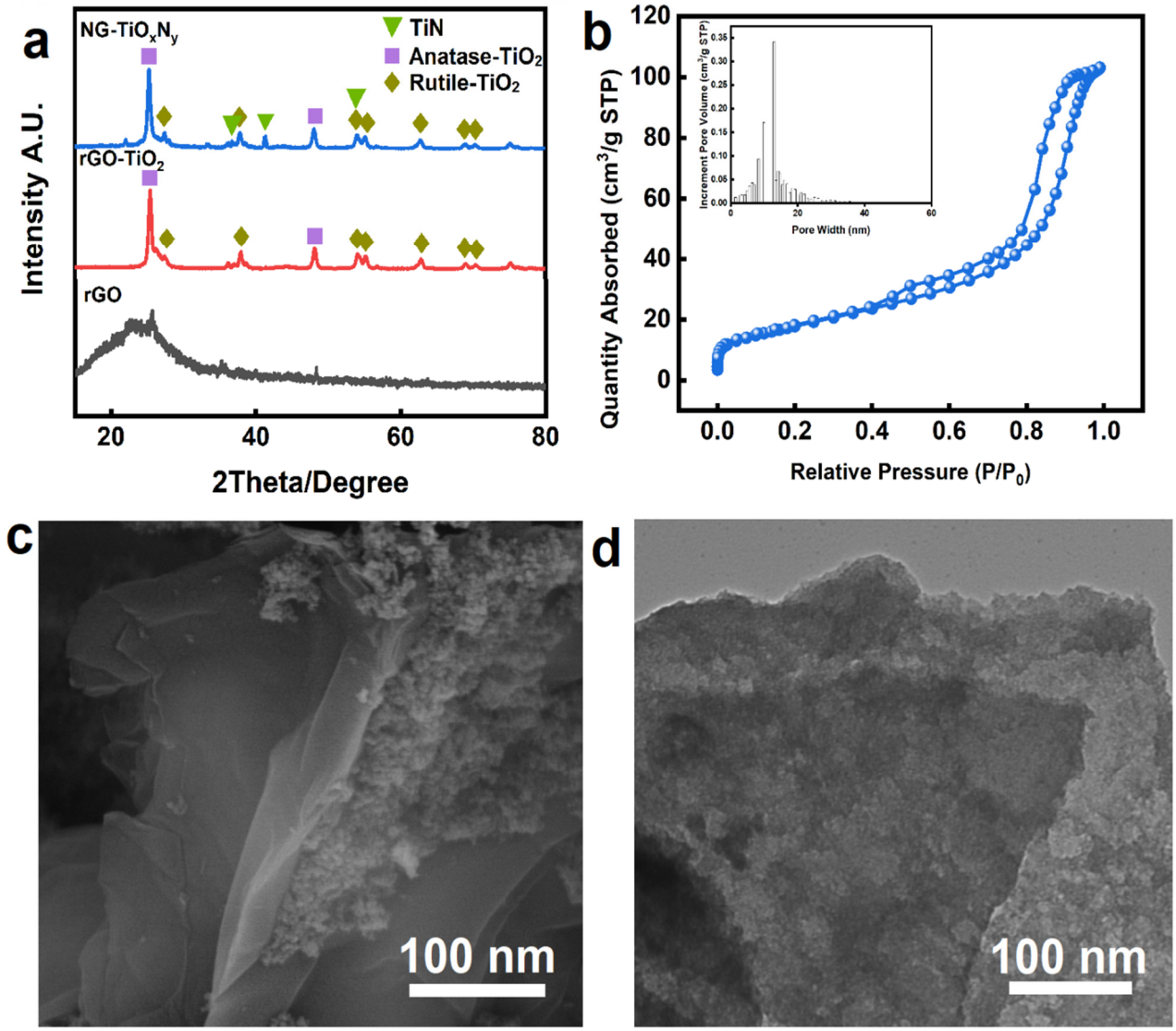

Figure 6-2 (a) XRD patterns of NG-TiO_xN_y, rGO-TiO_2 and rGO; (b) N_2 adsorption-desorption isotherm and associated pore size distribution of NG-TiO_xN_y; (c) SEM image and (d) TEM image of NG-TiO_xN_y.

Table 6-1 BET surface area and pore volume of NG-TiO_xN_y and rGO-TiO_2

	BET Surface Area $m^2\ g^{-1}$	BET Pore Volume $cm^3\ g^{-1}$
NG-TiO_xN_y	64.22	0.391
rGO-TiO_2	24.17	0.049

The elemental mapping (**Figure 6-3**) suggestes the homogenous distribution of the elements of the NG-TiO_xN_y at 5μm magnitude. The EDX mapping spectra reveales the mass ratio generally follows the rGO: TiO_2= 2:1 as initial. Nitrogen accounts for 13.40% atomic percentage (**Figure 6-3b**), demonstrating the nitrogen-enriched doped surface, which furthers the surface absorbing capacity.[215, 216] To to further study the chemical composition of the NG-TiO_xN_y electrode material.

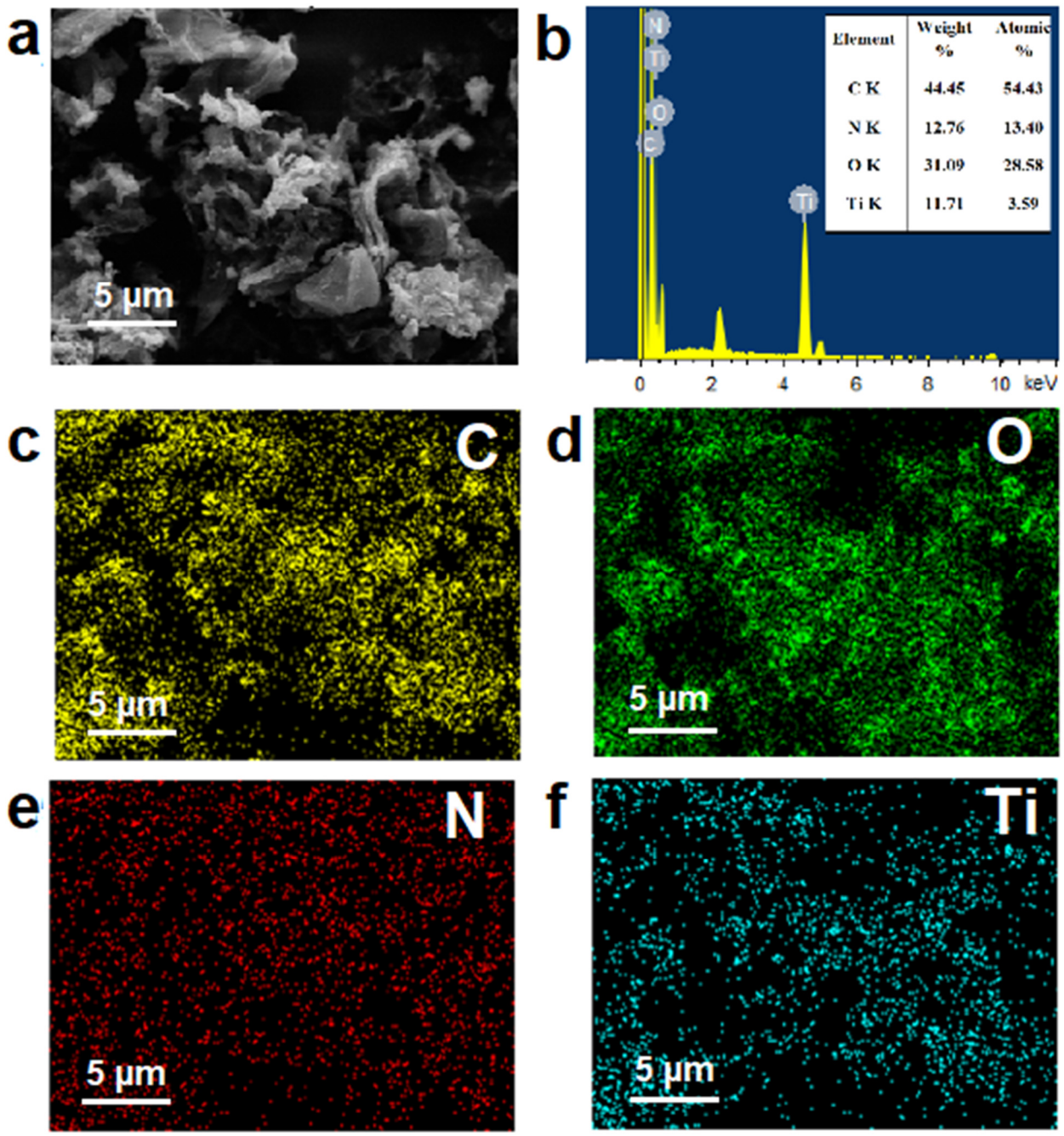

Figure 6-3 (a) SEM images of NG-TiO_xN_y; (b) EDX spectrum of the NG-TiO_xN_y associated with (a); elemental mapping of (c) C; (d) O; (e) N and (f) Ti.

X-ray photoelectron spectroscopy (XPS) was utilized, as shown in **Figure 6-4**. The wide survey of the NG-TiO_xN_y, as shown in **Figure A3-5**, exhibits several main peaks assigned as Ti 2s, O 1s, Ti 2p, N 1s, C 1s, Ti 3s, and Ti 3p, respectively. The high resolution XPS spectrum of O 1s in **Figure 6-4a** can be deconvoluted to Ti-O, C-O, -OH and O-C=O peaks, respectively. The formation of hydrogen bonds with water can further enhance the wettability of the electrode and has a positive effect on the ion storage process in the electrode material.[155, 156] The XPS spectrum of C 1s scan in **Figure 6-4b** is deconvoluted to the peaks of sp^2 C=C at 284.8 eV, sp^3 C-C peak at 286.8 eV, they are assigned to the C=C/C-C bond on the graphene aromatic ring. The peak at 287.4 eV and 289.2 eV are assigned to C=N and C-N bonds. Both demonstrate the successful nitrogen doping on the aromatic rings of graphene layer. The nitrogen configuration of the graphite layer can possibly result in a stronger binding energy with the ions in the electrolyte and enhancing the surface ion retention capacity.[217] Additionally, it is also reported the NG contributed to better wettability of the electrode material.[218] Thus, the presence of nitrogen doping graphene can be possible contributing to a higher salt adsorption capacity.[219] The carbon-oxygen peak at 291.3 eV is significantly diminished compared with the reported GO C1s spectra,[220] which can be attributed to the reduction of oxygen on the GO nanosheets during the hydrothermal treatment. The nitrogen-doped graphite potentially contributes extra salt adsorption capacity during the CDI process by

creating the surface vacancies.[154] The XPS spectrum of N 1s scan is presented in **Figure 6-4c**, where the main peak at 396.3 eV and the peak at 397.4 eV assigned to Ti-N and Ti-O-N confirm the successful nitridation process of the Ti species. Such formation of the Ti-N and Ti-O-N bonds resulted in various Ti species, providing possibility for cation intercalation within the chemistry bonds and increased its adsorption capacity.[221, 222] The peaks at 398.6 eV and 400.8 eV further confirm the pyridine and graphite nitrogen doping sites. **Figure 6-4d** illustrates the XPS spectrum of Ti 2p scan. The peaks at 458.5 eV and 456.8 eV are assigned to the N intercalation into TiO_2 lattice and the formation of TiO_xN_y.[223] The Ti $2p_{3/2}$ and Ti $2p_{1/2}$ peaks at 458 eV and 463 eV are mainly assigned to the Ti 2p peak of TiO_2, respectively.[224] The various Ti states of Ti potentially facilitate fast oxidation/reduction surface faradic reactions during the electrochemical charge and discharge process, which provide an opportunity to effectively improve the specific capacitance and ion adsorption capacity.[148, 149] Through the analysis of atomic percentages of different Ti species from the Ti 2p scan (Fig. S6), the value of O/Ti ratio (x) is calculated as 0.66 (Tab. S2). Thus, the composition of titanium compounds in this NG-TiO_xN_y nanocomposite (rGO: TiO_xN_y = 2:1 (w/w)) can be estimated as $TiO_{0.66}N_{0.61}$.

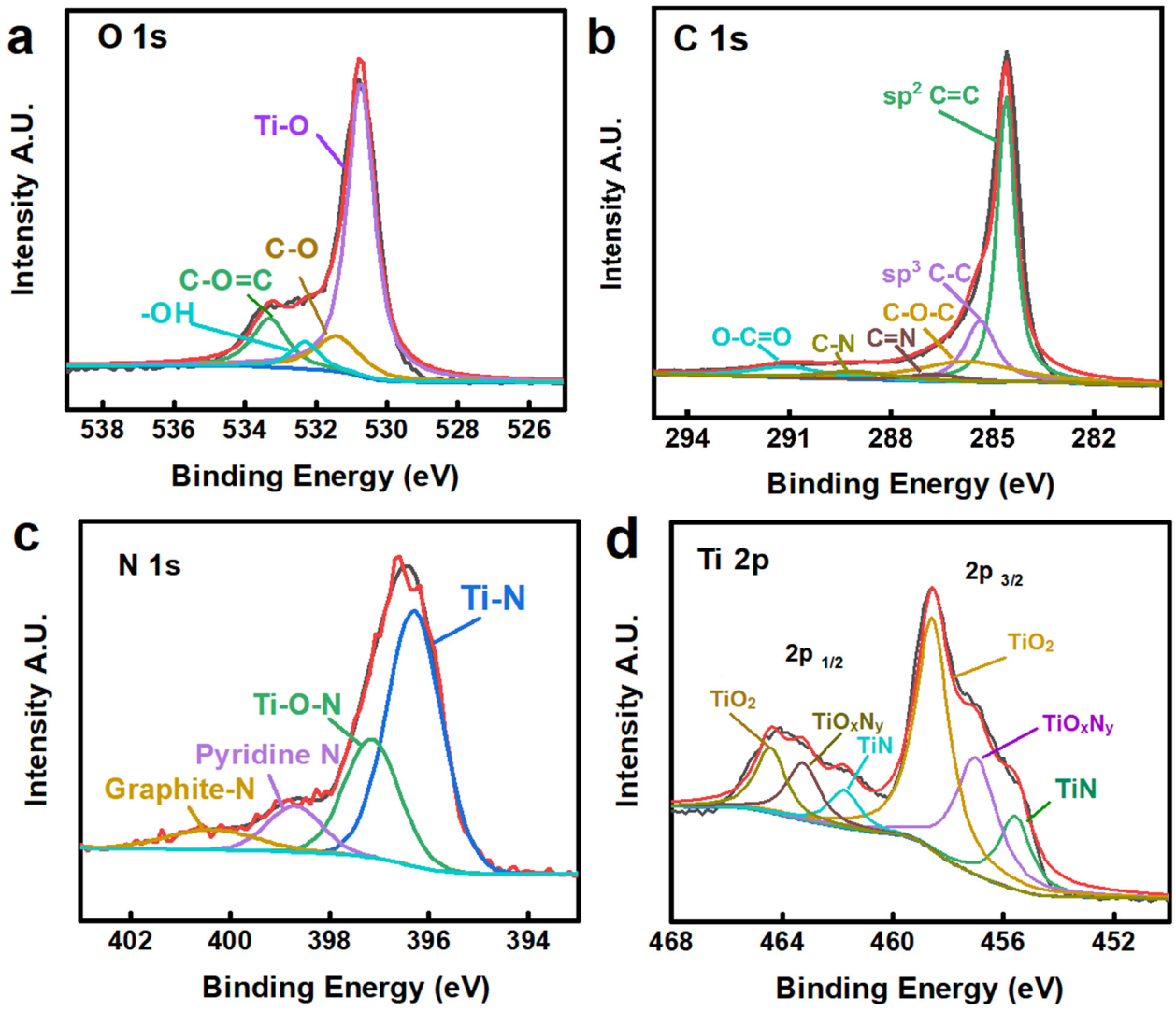

Figure 6-4 High resolution XPS spectra of NG-TiO_xN_y (a) C 1s scan; (b) O 1s scan; (c) N 1s scan; (d) Ti 2p scan.

6.3.2 Electrochemical Characterization

The CV curves were obtained at a wide range of scan rates (**Figure 6-5a**) and in NaCl electrolyte solution with 3 different concentrations (**Figure 6-5c**). All the CV curves of NG-TiO_xN_y are symmetric with respect to the x-axis and no significant oxidation/redox peaks were observed, indicating the reversibility of the EDL formation process dominated the electrosorption processes on the surface of the fabricated electrodes.[170] As calibrated in **Figure A3-1**, the symmetric CV curve shape of the CDI electrode is ranged from -0.5V~0.5V in actual, which indicates the electrode has the adsorption capacity for both Na^+ and Cl^-. To evaluate the electrochemical performance, the specific capacitance was calculated from the I–V plots, as shown in **Figure 6-5b**. The specific capacitance ranges from 84.3~66.5 F g^{-1} as the scan rate increased from 10 to 50 mV s^{-1}. The decrease in the specific capacitance is possibly due to the charge-resistive behavior when the scan rate increased.[225] The mass ratio of N-doped graphene: TiO_xN_y is approximately 2:1, which results in a significant decrease of specific area and electrochemical active area as opposed to sole N-doped graphene and a further decrease of specific capacitance.[215, 226, 227] **Figure 6-5c** shows the I–V curves for electrolyte solutions with concentrations of 0.1 mol L^{-1}, 0.5 mol L^{-1}, and 1 mol L^{-1}. Higher concentration of the electrolyte solution increased the mobility of the ions, while faciliatated the formation of EDL on the electrode surface more easily.[228] Thus, the specific

capacitance, ranging from 66.5~28.5 F g^{-1}, increased as the electrolyte concentration increased. In **Figure 6-5d** the NG-TiO_xN_y electrode kept 90% of its initial capacitance after 5000 CV cycles with at the scan rate of 50mV s^{-1}, demonstrating its excellent electrochemical stability. **Figure 6-5e** presents the comparison of NG-TiO_xN_y with commercial AC electrode, pure rGO, and rGO-TiO_2 (initial mass ratio 2:1). As can be seen from the figure, NG-TiO_xN_y showes higher specific capacitance at the scan rate of 50 mV s^{-1} than the AC, rGO and rGO-TiO_2 electrodes. The higher capacitance can be attributed to the nitrogen-doped sites on the graphene layer and the surface vacancies generated during the Ti species nitridation.[215, 229] Electrochemical Impedance Spectroscopy (EIS) analysis, which is usually used for evaluating the electrical conductivity of electrode materials, was performed to further investigate the electrochemical properties of the synthesized NG-TiO_xN_y. The Nyquist plots for the electrode material are shown in **Figure 6-5f**, where the typical semicircles can be observed, representing low resistance of the electrode/electrolyte interface and its high capacitance. The slope after the semicircle indicates the formation of the electrical double layer on the surface of the electrode material.[156] Compared with AC, rGO, and rGO-TiO_2 electrodes, the higher slope and smaller semicircle of NG-TiO_xN_y indicates its higher diffusion coefficient and smaller diffusion resistance for the adsorbed ions.[143] Such phenomena can be

explained by the formation of the surface oxygen vacancies and the capacitance from oxygen vacancies ion adsorption during ammonia heat treatment. [230]

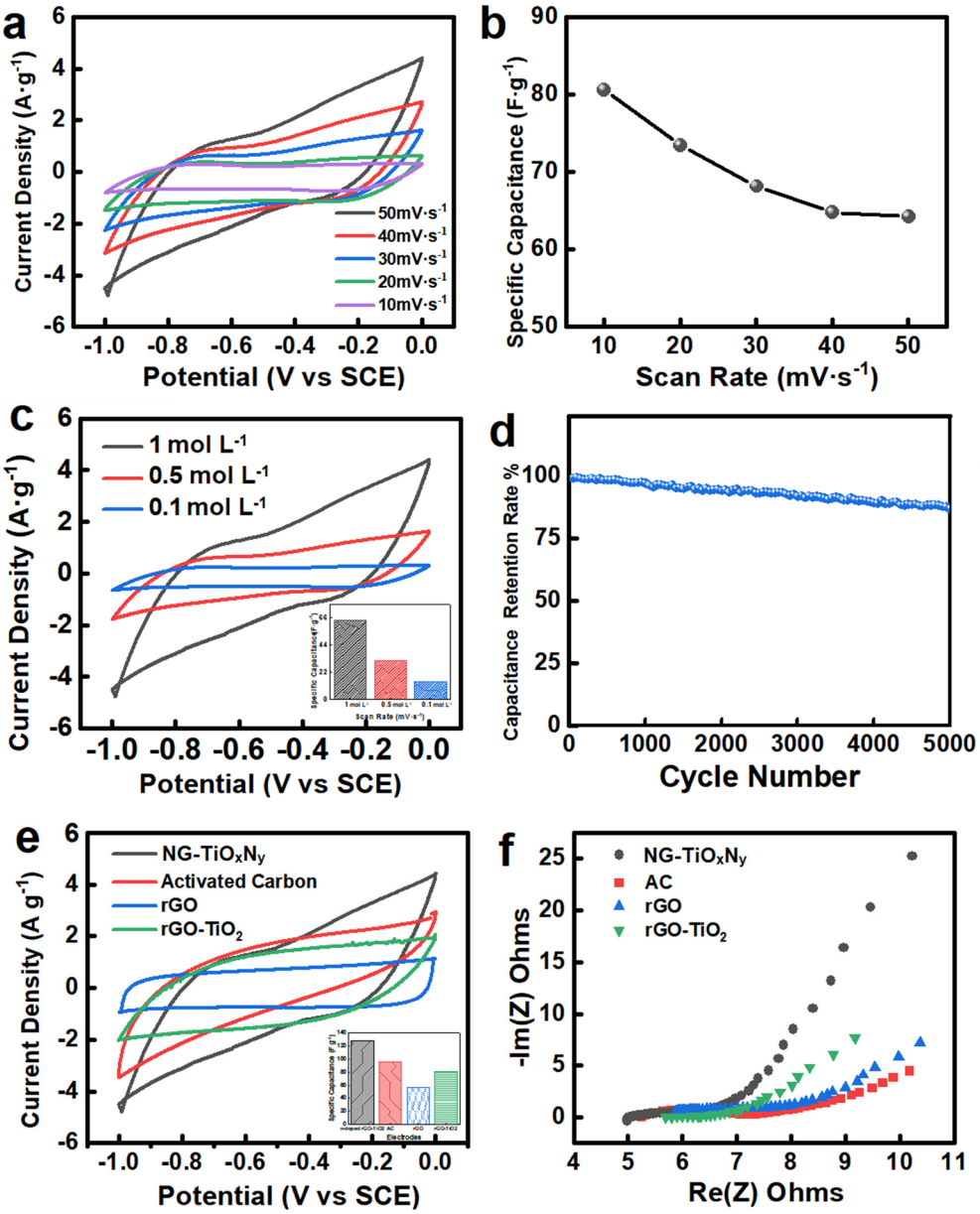

Figure 6-5 (a) CV curves of NG-TiO_xN_y electrode with scan rates of 10, 20, 30, 40, and 50 mV s^{-1}; (b) Specific Capacitance of NG-TiO_xN_y vs. scan rate. (c) CV curves of NG-TiO_xN_y with 0.1 mol L^{-1}, 0.5 mol L^{-1}, and 1 mol L^{-1} aqueous NaCl solutions; (d) Cycling stability test for 5000 cycles; (e) CV curves and specific capacitance of NG-TiO_xN_y, AC, rGO and rGO-TiO_2; (f) EIS Nyquist Plots of NG-TiO_xN_y, AC, rGO and rGO-TiO_2.

6.3.3 CDI Performance

The whole CDI process can be seen in **Figure A3-7**. The mass ratio graphite and Ti species were optimized by preliminary desalination experiments using different rGO: TiO_2 mass ratios, as shown in **Figure 6-6a**. Compared to the prstine rGO, rGO-TiO_2, and AC, the NG-TiO_xN_y material exhibited significantly lower salt retention rate, which is less than 50% at 25 min. The higher performance of NG-TiO_xN_y can be attributed to the enhanced ion absorbing capacity due to the nitrogen doping process with higher binding capacity between nitrogen doping sites and the ions,[215, 222] which is also corresponded with the better electrochemical performance. Furthermore, the higher CDI performance of the electrodes after nitrogen doping can be explained enhanced ions storage capacity in the surface vacancies formed during the ammonia heat treatment.[154] The optimized initial mass ratio of rGO: TiO_2 =2:1 was chosen for further study. Compared with rGO-TiO_2 (initial mass ratio 2:1), the n-doping and nitridation process significantly enhanced the salt adsorption capacity of the NG-TiO_xN_y CDI electrode material. The dramatically high salt efficiency of NG-TiO_xN_y can be attributed the multi-layered graphene nanosheets facilitated the rapid liquid diffusion; higher specific capacitance and the surface adsorption and ion intercalation within the Ti-O-N lattice.[148, 149]

Figure 6-6b-d shows the Ragone plots of SAC vs. SAR under different working conditions. [169] In all the three tests, the SAC increases rapidly during the

first 5 min and gradually reached saturated after 25 min, while the SAR follows the same pattern. **Figure 6-6b** shows the batch-mode CDI test was performed at 10 mL min^{-1} flow rate with 100 mg L^{-1} NaCl solution. The SACs reaches equilibrium approximately 8.1 mg g^{-1}, 9.6 mg g^{-1}, and 12.8 mg g^{-1} with cell voltages of 1.2 V~ 0.8 V at near saturated adsorption, respectively. Meanwhile, the SAR of each group at initial stage reached 0.7~0.95 mg g^{-1} min^{-}. The increase in the SACs and SARs indicated that the salt adsorption capacity was strongly depended on potential applied on the cell, which will result in a more cohesive electrical double layer and enhance the ion absorbing capacity.[141] In **Figure 6-6c**, the SACs were obtained with 10 mL min^{-1} flow rate and 1.2 V while the salinity of the pumped-in water concentrations ranges from 100 mg L^{-1}~500 mg L^{-1}. Despite the increase in saline water concentration, the electrode maintained its salt adsorption capacity, demonstrating the possibility of its application in high salt concentrations treatment. At the salt concentration of 500 mg L^{-1}, the salt adsorption capacity reached a breakthrough SAC of 26.1 mg g^{-1} at its near saturation adsorption. It is also worth to mention the SAR of 500 mg L^{-1} saline water group reached as high as 1.8 mg g^{-1} min^{-1}, which is considerable high SAR compared with previous reports.[169] **Figure 6-6d** shows the SACs for different flow rates (10~30 mL min^{-1}) at 1.2 V and salt concentration of 100 mg L^{-1}. The SAC curves have a similar trend as the previous experiments, and the SACs were 12.6 mg g^{-1}~7.0 mg g^{-1} while the SARs were

0.95~0.45 mg g^{-1} min^{-1} at near saturated adsorption, respectively. The relatively smaller SAC declines when performing the CDI test in higher flowrates enabled its potential in fast water desalination. **Figure 6-6e** shows the current-elapsed time curve, which directly corresponded to the conductivity and salt removal efficiency curve by measuring the current at the outflow stream. The potential applied to the CDI cell shifted from 1.0 V to -1.0 V at 25 minutes. The current curve quickly dropped in the first 10 minutes, and then reached the lowest current at 25 minutes. The conductivity of the outflow water recovered slightly and reached the saturation point of ions adsorption. The potential was shifted at 25 minutes, resulting in a rapid increase in reverse current, showing the release of ions from the porous electrode. The negative current then decreased after a few minutes, which indicated that the reverse adsorption process occurred. The rapid charge and discharge performance of the NG-TiO_xN_y electrode demonstrated its great potential in ad/desorption potential. In **Figure 6-6f**, the regeneration test was performed using NaCl saline water with 10 ml min^{-1} flow rate and 100 mg L^{-1} salt concentration and repeated charge-discharge cycles for 30 minutes. The salt removal efficiency remained at 90% of its original capacity for over 12 cycles which is superior than most reported titanium-based CDI electrodes.[51, 213] The stable cycling stability demonstrated that the synthesized NG-TiO_xN_y has an excellent potential for longtime-continuous desalination application. Compared with several reported porous carbon and titanium-carbon electrode

materials (**Table A3-2**), the NG-TiO_xN_y material in this work exhibites significantly higher salt adsorption capacity.

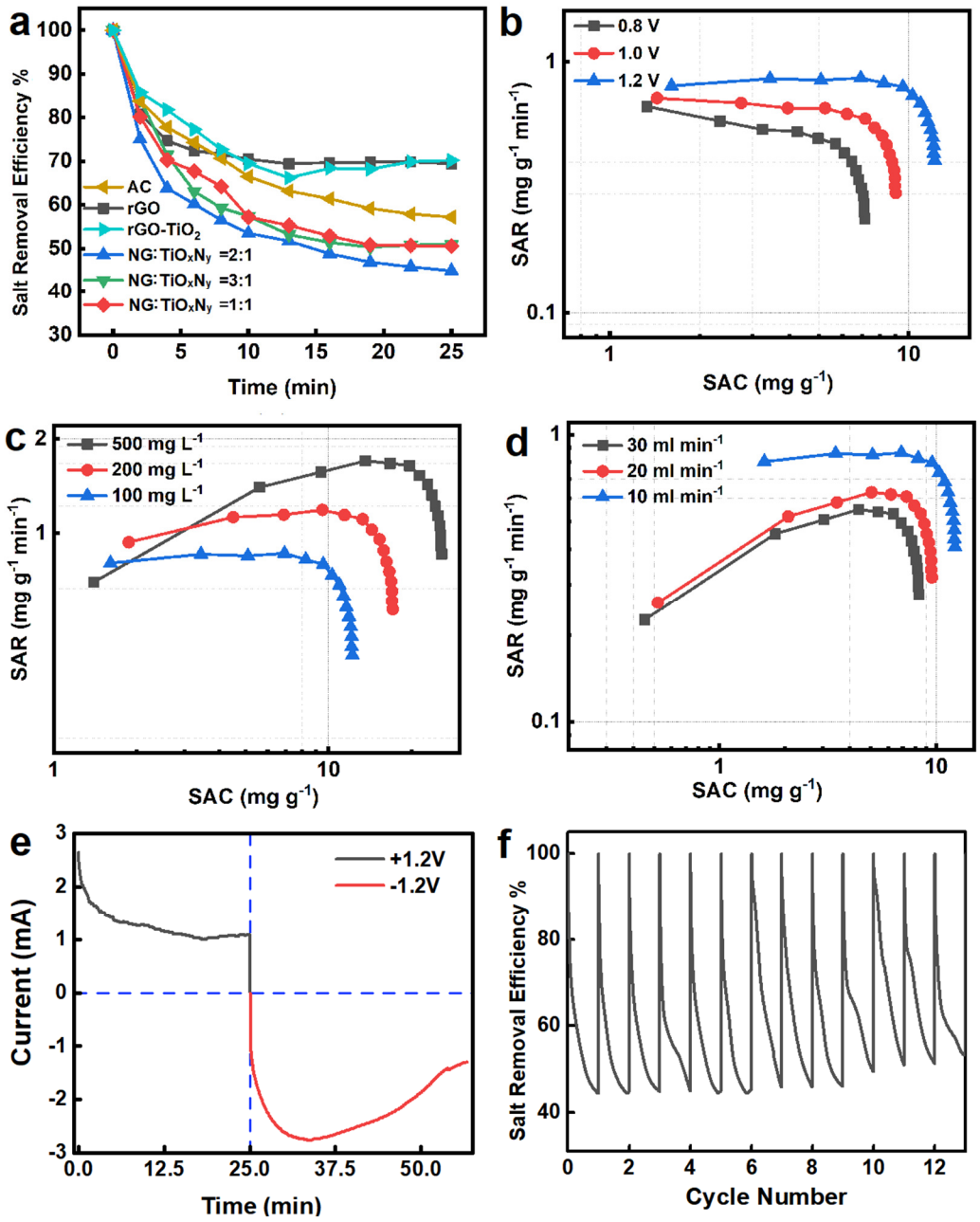

Figure 6-6 (a) Comparison of salt retention curves of electrodes NG:TiO_xN_y=1:1 to 3:1, rGO, and AC; Ragone Plots of NG-TiO_xN_y at: (b) potential of 0.8 V, 1.0 V and 1.2 V; (c) water salinity of 500 mg L^{-1}, 200 mg L^{-1}, and 100 mg L^{-1}; (d) flow rates of 30 ml min^{-1}, 20 ml min^{-1} and 10 ml min^{-1}; (e) current vs time plot; (f) cycling stability for over 12 cycles.

Table 6-2 SAC comparison of commercial AC, typical carbon electrodes, n-doped carbon and titanium-based CDI electrodes.

Electrode	Cell Voltage V	Salinity mg L^{-1}	SAC mg g^{-1}	References
Commercial AC	1.2	292-1170	10.9~13.0	[67]
Carbon Aerogel	1.2	100~1000	5~15	[231]
Graphene and derivatives	0.8~1.2	100~1000	5~20	[139]
rGO-TiO_2	1.2	300	9.2~13.2	[174]
CNT-TiO_2	1.2	500	~4.3	[232]
TiO_2-AC	1.2	500	~2.7	[175]
TiO_2 NPs/AC	1.2	100	~8.04	[51]
Ti_3C_2-Mxene	1.2	100	13	[176]
N-doped graphene	1.2	500	>17.8	[233]
N- sphere carbon	1.2	1000	14.91	[234]
N-doped TiO_2/ZrO_2	1.2	50	3.98	[172]
$Ti_3C_2T_x$ Mxene	1.2	500	20~24	[133]
3DOM-TiN	1.2	500	25.3	[207]
NG-TiO_xN_y	1.2	500	26.1	This work

6.4 Chapter Conclusions

In this work, we successfully synthesized a novel type of nitrogen-doped graphene-titanium oxynitride (NG-TiO_xN_y) nanocomposite electrode via hydrothermal reaction and high-temperature nitridation process and then tested for CDI). The physical and chemicalcharacterization revealed the nitrogen was successfully doped onto the graphite layer and formed various species of nitrogen-doped carbon. Additionally, the TiO_xN_y nanoparticles were also formed and embedded on the graphene nanosheets. Further study revealed the ammonia treatment and the loaded TiO_xN_y nanoparticles gave the electrode better electrochemical performance and extra ion absorbing capacity compared with graphene and TiO_2 based CDI electrodes. Consequently, the multi-layered graphene nanosheets allowed the saline water stream to pass through the electrodes and absorbing ions in both the surface of nitrogen-doped graphene and TiO_xN_y nanoparticles. In the batch mode CDI test, the NG-TiO_xN_y electrode-based CDI device exhibited a significantly high salt adsorption capacity of 26.1 mg g^{-1} at its near saturated adsorption using 500mg L^{-1} feed-in saline water. In the cycling stability test, the NG-TiO_xN_y electrode lasted for over 12 cycles while retaining over 90% of its original salt removal capacity, furthers its great potential in long-time continuous CDI application.

Chapter 7: Conclusions and Future Work

7.1 Summary and Conclusions

The main objectives of this thesis were to develop a novel nano-material for solid suspension removal and electrode materials for capacitive deionization desalination in water treatment.

In the first phase of this work, magnetic flocculant was developed and tested for solid suspensions removal. Magnetite nanoparticles synthesized *in-situ* significantly accelerated the settling down process in solid suspension removal in wastewater with the presence of an external magnetic field. This study enabled a fast and low-cost way in treating the solid suspensions in waste water. To achieve this, the flocculants were combined with the *in-situ* synthesized magnetite particles to improve the settling down performance in simulated solid suspension water. The research strategy of "cyclic-investigation" was adopted in further analysis and improvement of the studied materials. By using simple and low-cost synthesizing methods, the objective of the first phase research was successfully achieved. This preliminary research opens a door for further industrial and commercialized study on magnetic flocculants materials.

In the second phase, the objective of the thesis was to develop novel and unique nano-porous electrode materials for high capacity desalination in capacitive

desalination. To achieve this, several selected materials were synthesized, modified, and tested in simulated salty water. The “cyclic-investigation” process was also adopted during this phase of the research process. A simple, low-cost and environmentally friendly synthesis process was also an important objective in this work. All the developed materials proved to be effective electrode materials in capacitive deionization. Future research can be done on industrial and commercial development of the electrode material.

To investigate the morphology, physical and chemical properties of the developed materials, a number of characterization techniques including XRD, XPS, Raman spectroscopy, FT-IR, BET, TGA, SEM and TEM were used. The electrochemical performance was evaluated by using techniques including cyclic voltammetry, charge-discharge and electrochemical impedance spectroscopy. The performances of solid suspension removal and water desalination were examined by using the techniques of visible-ultraviolet light adsorption and conductivity test.

Three classes of materials were developed in this work. The developed materials were: 1) magnetic Fe_3O_4-GO nanoparticles for solid suspension removal; 2) 3DOM-Titanium Nitride for capacitive deionization; 3) and N-doped rGO-TiO_xN_y for capacitive deionization. The summary and conclusions for each one of the materials are discussed below.

7.2 Fe_3O_4-Graphene Oxide Magnetic Nanoparticles for Highly Efficient Solid Suspension Removal

This work reveals that the synthesized magnetic Fe_3O_4-GO can be used as a high-efficiency agent in rapidly removing and settling down the solid suspensions in treating wastewater with an external magnetic field. The synthesized magnetic Fe_3O_4-GO requires much smaller amount (0.1g magnetic flocculant per 40mL solid suspension solution) added into the solid suspension solution and can reach nearly 90% removal rate within 30 minutes, with little residue in the treated water. The characterization and adsorption experiment indicated that the magnetic Fe_3O_4 components interacted with the external magnetic field while the GO attracted the solid suspension particles in the solution, and finally accelerated the settling down process compared to the gravity settling process without an external magnetic field. The adsorption test demonstrated that the adsorption behavior followed both the Langmuir and Freundlich model, with an adsorption capacity of 58.46 mg mg^{-1}. The test also showed that the kinetics of the adsorption process followed a pseudo-second-order kinetic model with an initial rate V_0=0.0275 mg mg^{-1} min^{-1}. Overall, the results showed a small amount (0.1g magnetic flocculant per 40mL solid suspension solution) of Fe_3O_4-GO exhibited a potential application in treating polluted water containing solid suspended particles.

7.3 A 3D Ordered Titanium Nitride Electrode for Highly Efficient Capacitive Deionization

In this work, we successfully synthesized 3DOM-TiN using a PS template method. The 3DOM-TiN was characterized and fabricated into electrodes for batch mode capacitive deionization cells. The characterization results showed that 3DOM-TiN had a relatively hierarchically-ordered 3D hollowed structure, providing multiple tunnels for salt water diffusion and a relatively large surface area for ions to be absorbed and stored in the electrode. The synthesized material was demonstrated to be highly efficient, with stable regeneration for over 10 cycles, high salt adsorption capacity of 22.1 mg g^{-1} per unit mass, which is significantly higher than the current commercial porous carbon material and other previously reported titanium-based materials. (See in **Table A2-4, 5 & 6**) The study also revealed the relative stability of TiN electrodes after 10 cycles of the experiment, in which the electrode kept over 90% of its capacity for retaining the ions in the liquid. This work thus furthers the possibilities of using TiN as the electrode material for capacitive deionization, which may be further developed into a novel material for electrical desalination material with great industrial application potentials.

7.4 Nitrogen-Doped Graphene-TiO_xN_y Nanocomposite Electrode for Highly Efficient Capacitive Deionization

In this work, we successfully synthesized a novel type of nitrogen-doped graphene-titanium oxynitride (NG-TiO_xN_y) nanocomposite electrode via hydrothermal reaction and high-temperature nitridation process. The electrode was then used during CDI testing. The physical and chemical characterization revealed the nitrogen was successfully doped onto the graphite layer and formed various species of nitrogen-doped carbon. Additionally, the TiO_xN_y nanoparticles were also formed and embedded on the graphene nanosheets. Further study revealed the ammonia treatment and the loaded TiO_xN_y nanoparticles gave the electrode better electrochemical performance and extra ion-absorbing capacity compared with graphene and TiO_2-based CDI electrodes. Consequently, the multi-layered graphene nanosheets allowed the saline water stream to pass through the electrodes and absorbing ions in both the surface of nitrogen-doped graphene and TiO_xN_y nanoparticles. In the batch mode CDI test, the NG-TiO_xN_y electrode-based CDI device exhibited a significantly high salt adsorption capacity of 26.1 mg g^{-1} at its near saturated adsorption using 500 mg L^{-1} feed-in saline water. In the cycling stability test, the NG-TiO_xN_y electrode lasted for over 12 cycles while retaining over 90% of its original salt removal capacity, demonstrating its great potential in long-time continuous CDI application.

7.5 Recommendations for Future Work

The above studies and achievements in this thesis are the preliminary step in further studies in high performance nanomaterials for water treatment. Based on the above findings and studies in this thesis, it is suggested the future work should focus on the following directions:

7.5.1 Magnetite-GO and its Derivatives

The graphene oxide and its derivatives, such as reduced graphene oxide, are widely reported in the literature to exhibit excellent performance in removal waste components in the water. Thus, it is highly recommended that future research focus on developing magnetite-GO and its derivatives in highly efficient magnetic removal of solid suspensions. Other recommendation including i) optimizing and simplifying the synthesis procedure of the GO and its derivatives with magnetite; 2) tuning and controlling the morphology of the nano-graphene sheets for high surface area, higher solid suspension absorbing capacity and better wettability; 3) and tuning the magnetic core and *in-situ* synthesis method of the magnetic flocculant to achieve for higher efficient solid suspension removal.

7.5.2 Electrode Pairs for Anode and Cathode

For most CDI-like supercapacitor cells, the electrode materials of cathode and anode are different at each side for specific anion and cation absorption. It is highly recommended in future studies that cathode and anode electrode materials should be designed and fabricated separately. By using two different electrode materials in combination in the CDI cell the salt adsorption capacity could be significantly increased. In this thesis, the study revealed the dual-adsorption mechanism happened on the TiN electrode. However, through the external circuit and electron transferring, both the anode and cathode sides can benefit from the extra ion adsorption capacity gained by intercalation-controlled pseudo capacitance. However, it is reasonable to consider further improvement could be made on developing anode electrode materials paired with TiN cathode with higher salt adsorption capacity.

7.5.3 Further Investigation on Pseudo Capacitance of CDI Electrode Material

Research on 3D-ordered titanium nitride successfully revealed a possible dual adsorption model: the diffusion-controlled electrical double layer model and the intercalation-controlled adsorption model. It is suggested that besides the conventional porous carbon electrode, other research should focus on porous metal-based electrode materials. With the intercalation of ions into the electrode, pseudo capacitance has a great potential in contributing to extra adsorption capacity. Possible metal-based electrodes include titanium oxide/nitride, organic metal

framework, rare earth additives, MXene-based electrodes, etc. An in-depth study on pseudo-CDI electrodes could possibly open a door to a new research frontier in CDI electrode materials.

Appendix

Appendix A

XPS supplement information

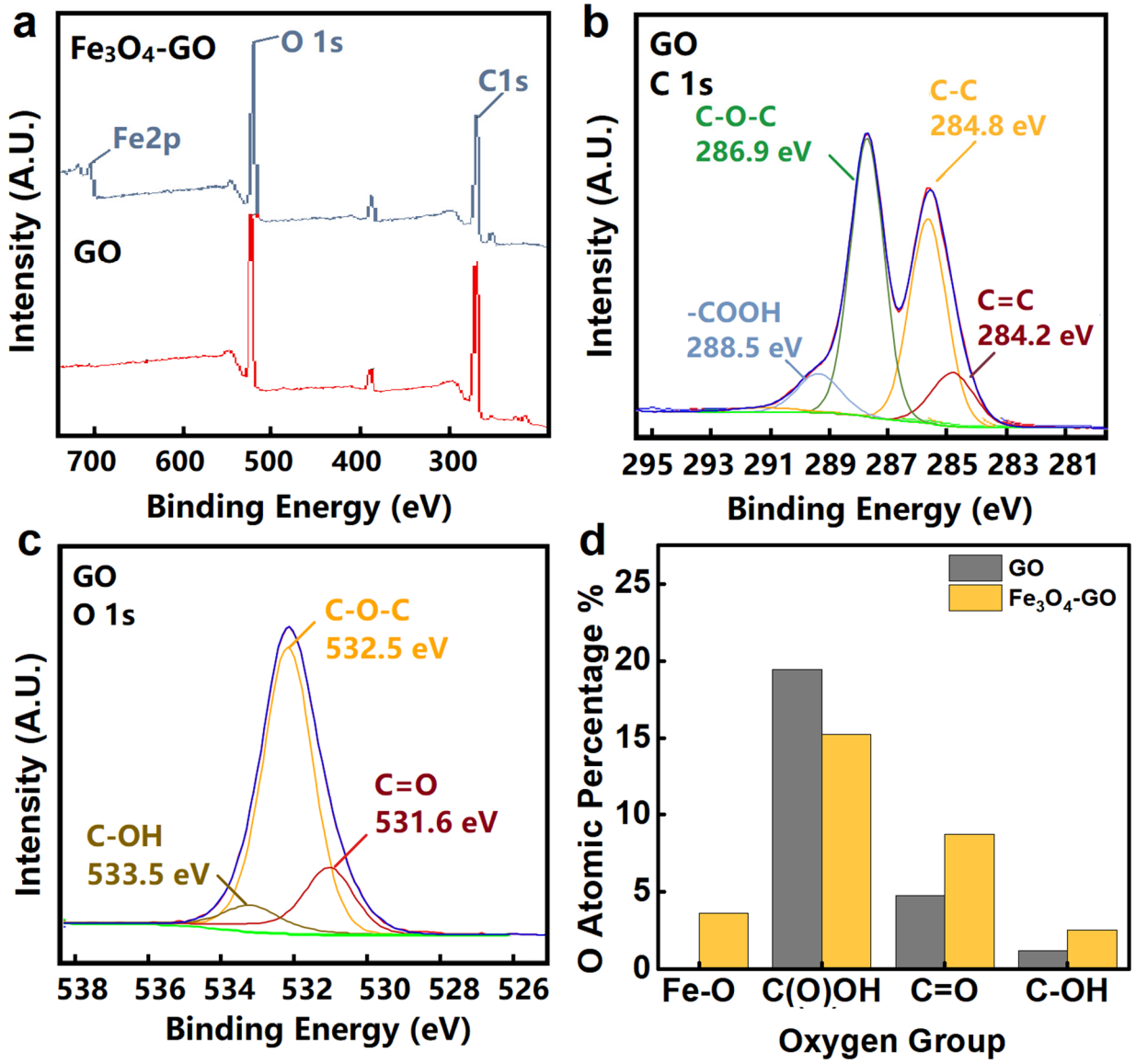

Figure A1-1(a) XPS survey of GO and Fe_3O_4-GO, high-resolution XPS spectra of (b) C 1s and (c) O 1s for GO powder and (d) associated atomic percentage of oxygen groups in GO and Fe_3O_4-GO.

Quantification of kaolinite concentration

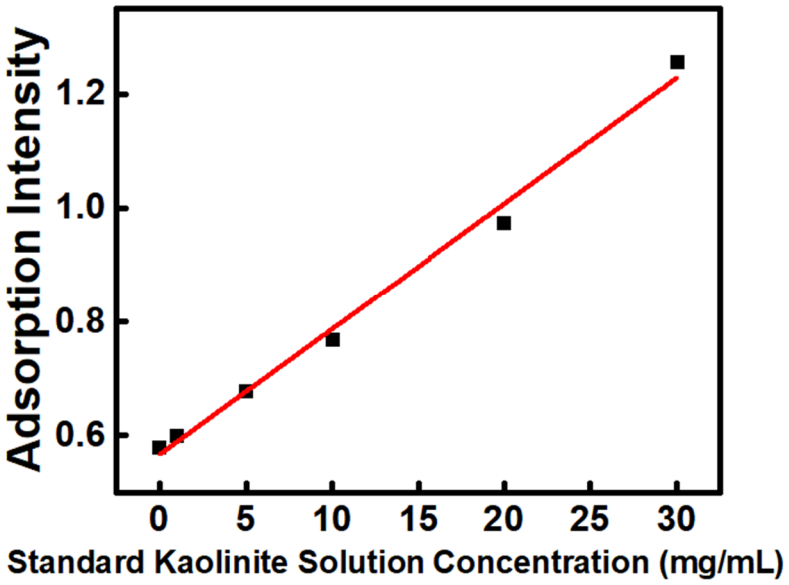

Figure A1-2 Standard curve of light adsorption as a function of the concentration of kaolinite

A series of kaolinite solutions with different concentrations were prepared and tested for the data of light adsorption, and was fitted into a linear **Equation A1-1** as **Figure A1-2**:

$$A = 0.0084 * C + 0.5733 \qquad (\mathbf{A1\text{-}1})$$

The equation can also be written as **Equation A1-2** for experimental data calibration:

$$C = -68.013 * A + 118.645 \qquad (\mathbf{A1\text{-}2})$$

Where $\boldsymbol{C}$ is the concentration of kaolinite (mg ml^{-1}), and $\boldsymbol{A}$ is the light adsorption intensity at 307 nm.

Optimization of Fe_3O_4/GO ratio

To obtain a suitable ratio of Fe_3O_4 to GO, a series of composite samples with the theoretical Fe_3O_4 mass ratio to 1 gram of GO as 1%, 5%, 10%, and 20% were synthesized and tested. The concentration of kaolinite suspension was tested after 5 min of settling down. The removal efficiency is calculated and listed in **Figure A1-3**. Generally, the more Fe_3O_4 nanoparticles were deposited, the more kaolinite particles were removed within 5 min. As depicted in **Figure A1-3**, the removal efficiency starts to plateau at 10% Fe_3O_4 nanoparticles. Thus, 10% mass ratio of Fe_3O_4-GO was selected as the optimal ratio for the synthesis of Fe_3O_4-GO.

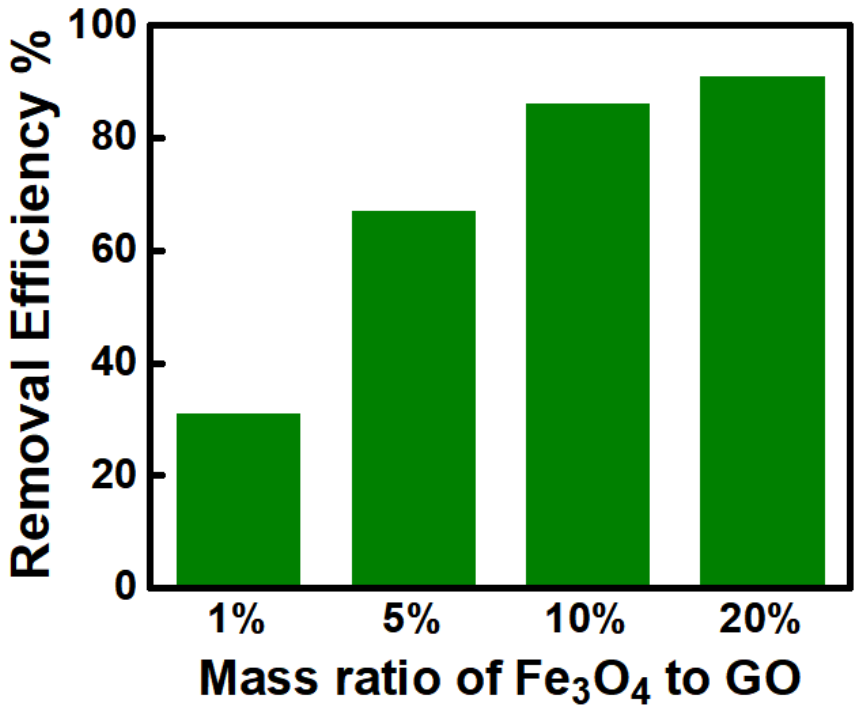

Figure A1-3 Kaolinite Removal Efficiency of Fe_3O_4-GO with different Fe_3O_4 mass ratio.

XRD Supplemental Information for Chapter 4

This figure contains a series of unpublished preliminary experiments and XRD characterizations.

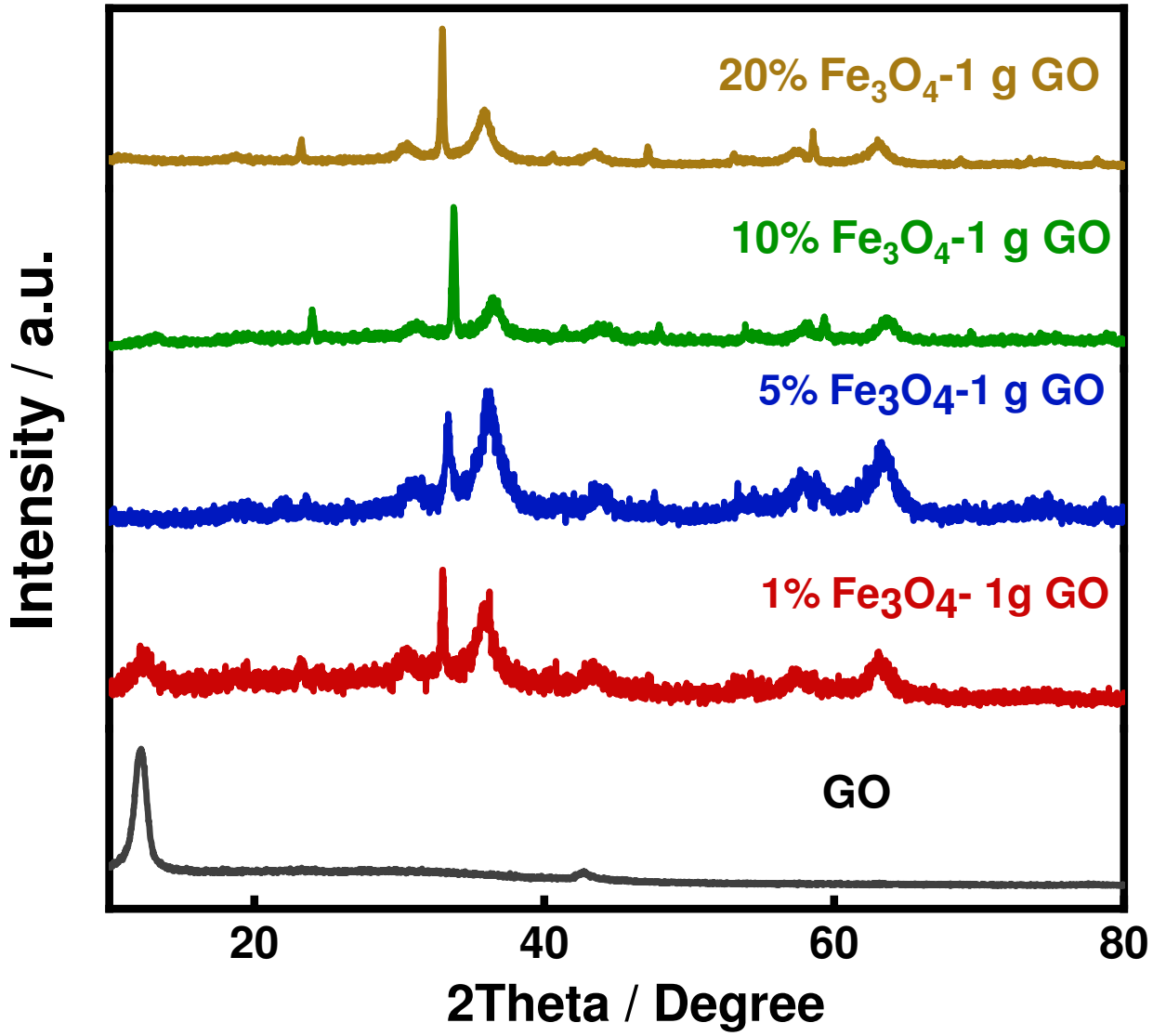

Figure A1-4 XRD characterization of Fe: GO with different mass ratio.

Removal efficiencies of several materials for magnetic flocculants when reaching 99% removal efficiency of Fe_3O_4-GO.

This figure is a comparison of several unpublished magnetic-flocculant tested in phase one research.

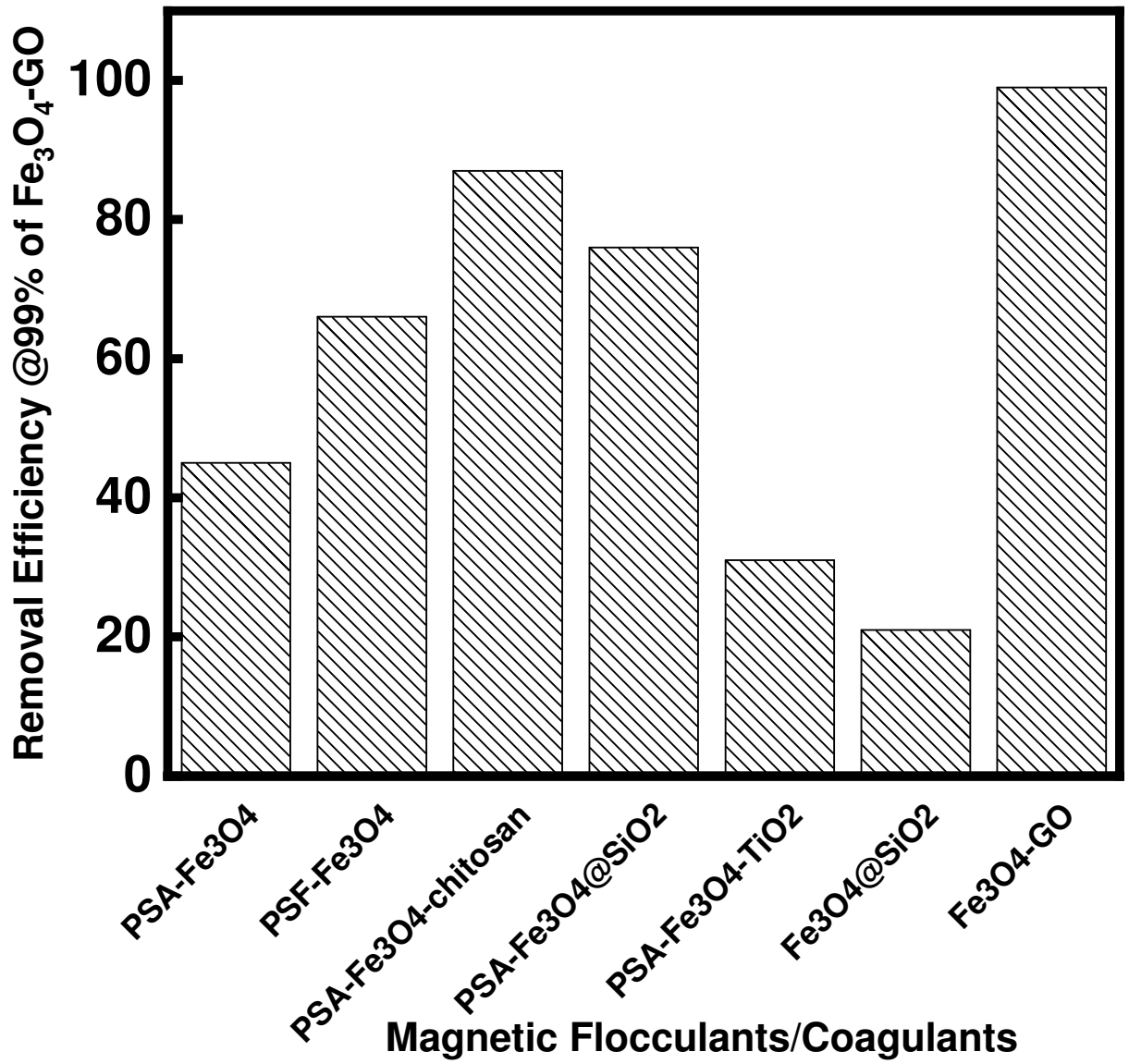

Figure A1-5 Removal efficiencies of several magnetic flocculants.

Comparison of magnetic flocculants in solid suspended wastewater treatment

Table A1-1 Comparison of Magnetic Flocculant in wastewater pollutants removal

Absorbent	Adsorbate/ Wastewater type	Initial Concentration	Removal Efficiency	refs
CPAM-Fe_3O_4 magnetic flocculant	C. ellipsoidea Microalgal	25~120mg/L	>95% at PH=7*	[7]
PAC-magnetite	Solid in biodiesel waste water	348mg/L	54%~97% at PH=7*	[235]
PAA-Fe_3O_4	Industrial waste water	752~2041mg/L	76% at over 24h	[236]
PAC-magnetite	Backside grinding wastewater	1.24~2.94g/L	83% at PH=6*	[237]
CS-Fe_3O_4	Urban life waste water	400mg/L COD	67.50% 2.5h	[238]
CS-Magnetite	Urban life waste water	400mg/L COD	49.38% 2.5h	
PAC-Fe_3O_4	Industrial waste water	>1000NTU (Turbidity)	85% in 30mins	[239]
PAC-Magnetite	Restaurant waste water	4300~5000mg/L	85.2%-92.5% over 2.5 hrs	[6]
PSFS-Magnetite	Urban rain water	318mg/L COD	52.0%-63.9% at PH=7*	[240]
Ammonium Chloride-Fe_3O_4, etc.	Kaolinite	~80mg/mL	>75% over 1~3 hrs	[241]
CS-Fe_3O_4	Kaolinite	245~255 NTU (Turbidity)	87% in 10 mins	[242]
Fe_3O_4-GO	Kaolinite	40mg/mL	90% in 30mins	This Work

*In these experiments, the removal efficiencies were measured at near neutral, (pH=6~7) of the solutions.

Economic and cost-effective analysis of Fe_3O_4-GO as the magnetic-flocculant

This part appeared on the respond to reviewers during peer-review.

The price of current commercial flocculants, (such as PAC, PFS etc.) usually ranges from U$ 200-1000/ ton. (Alibaba.com), the graphene oxide price is based on its grade. In this work, low grade graphene oxide will be enough in wastewater treatment, which costs around U$5 per 10gram (Alibaba.com). Since the synthesized nanocomposite can be stored as solid state and the dosage is significantly lower than the liquid solution state commercial flocculants. The overall cost can be highly competitive to the current commercial flocculants.

Appendix B

Supplemental Characterization Information

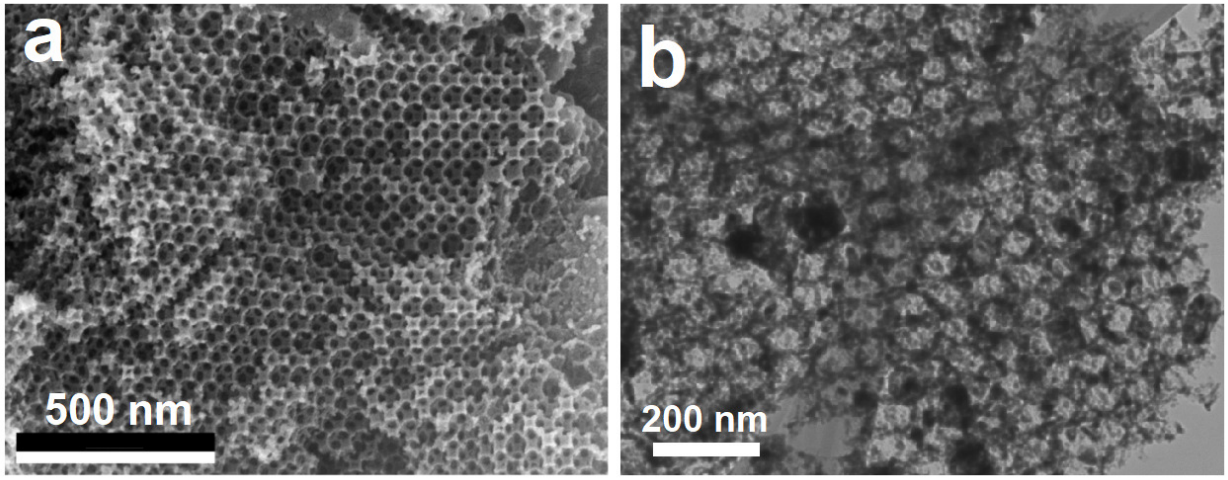

Figure A2-1 (a) SEM and (b) TEM images of 3DOM-TiN at low magnification.

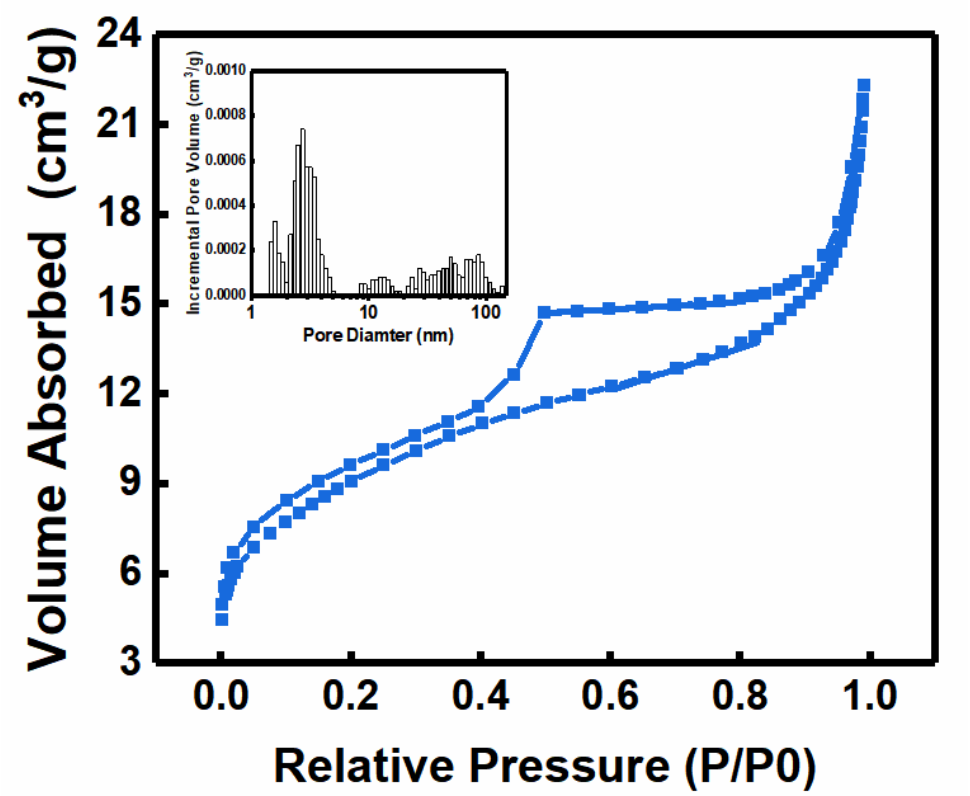

Figure A2-2 N_2 adsorption-desorption isotherm and associated pore volume distribution of bulk-TiN.

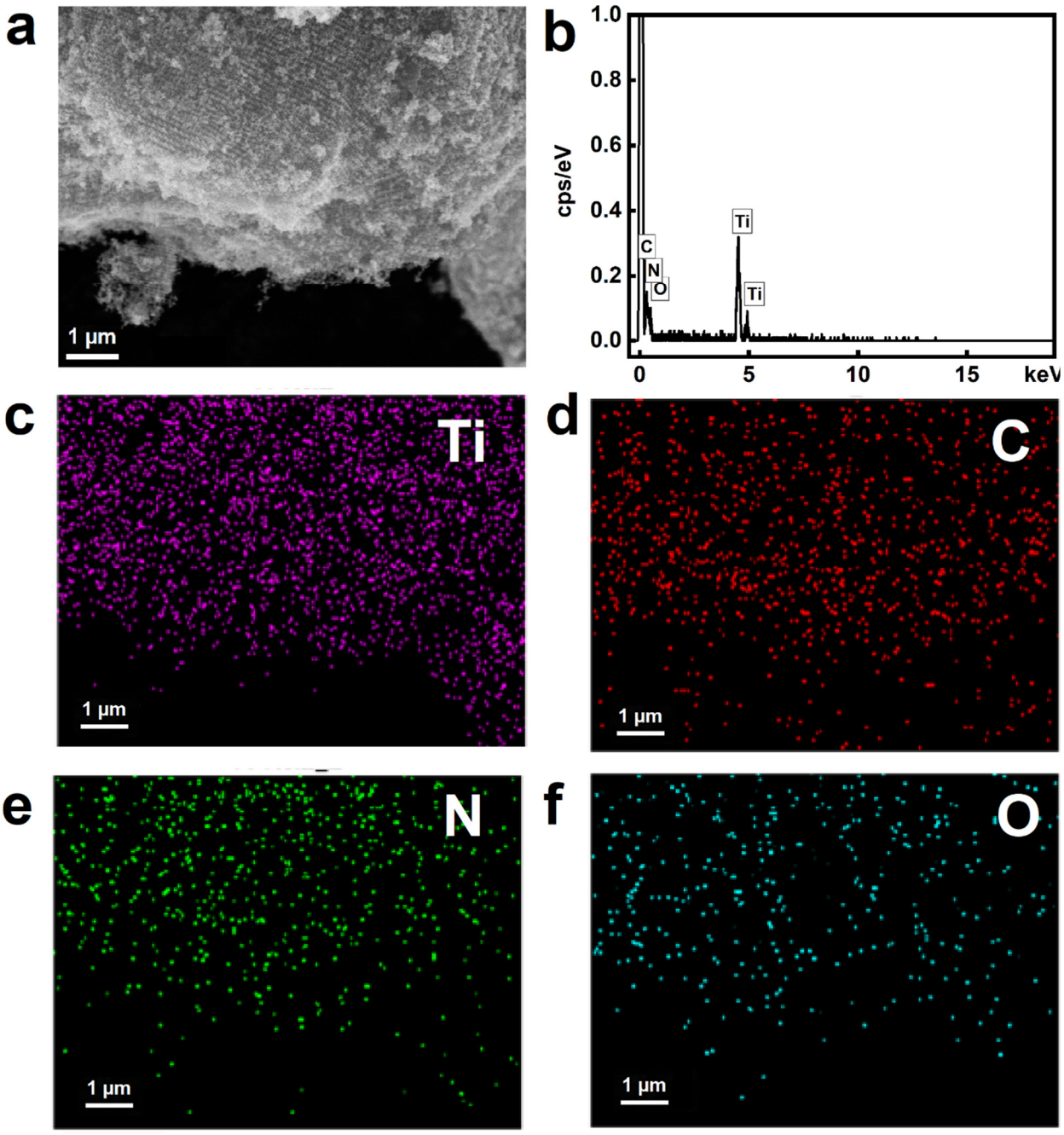

Figure A2-3 (a) SEM image and (b) EDX spectrum of 3DOM-TiN as well as associated elemental mapping: (c) Ti, (d) C, (e) N, and (f) O.

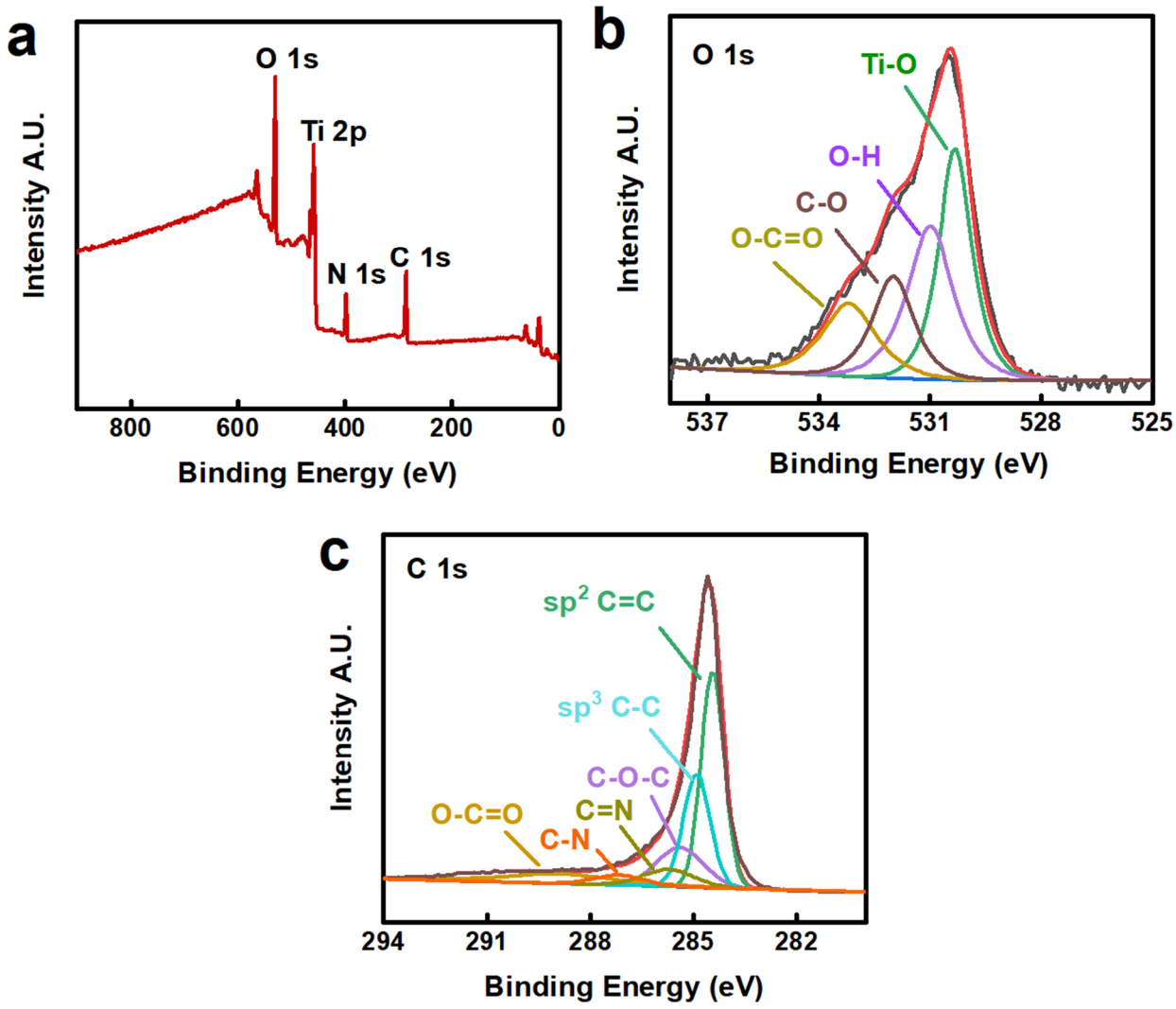

Figure A2-4 (a) XPS survey and HR-spectra of (b) O 1s and (c) C1 s for 3DOM-TiN.

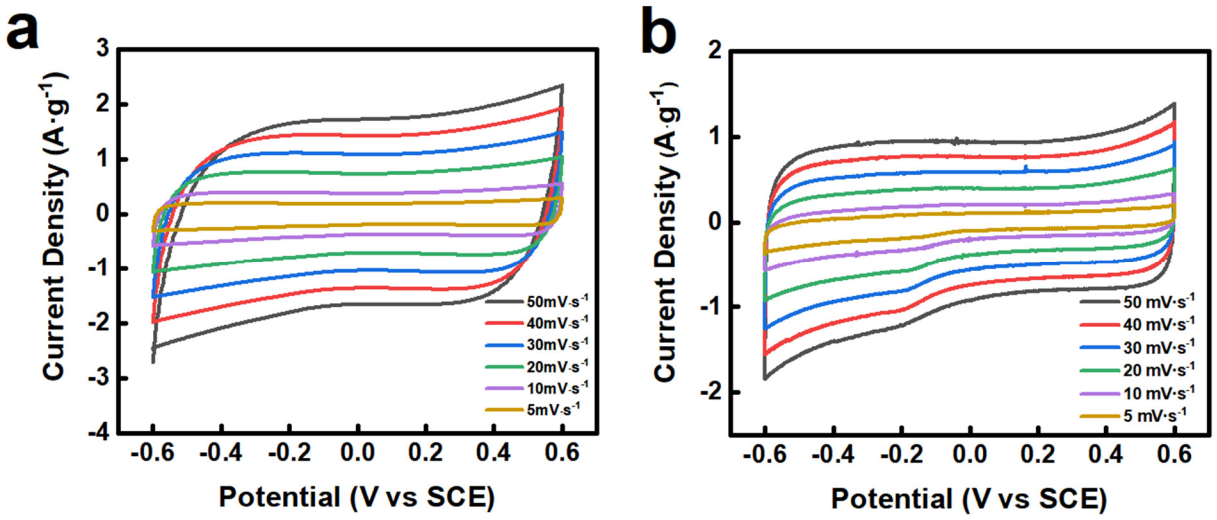

Figure A2-5 CV curves of (a) AC and (b) bulk-TiN electrode in 1 mol L^{-1} NaCl solution with scan rates of 50, 40, 30, 20, 10, and 5 mV s^{-1}.

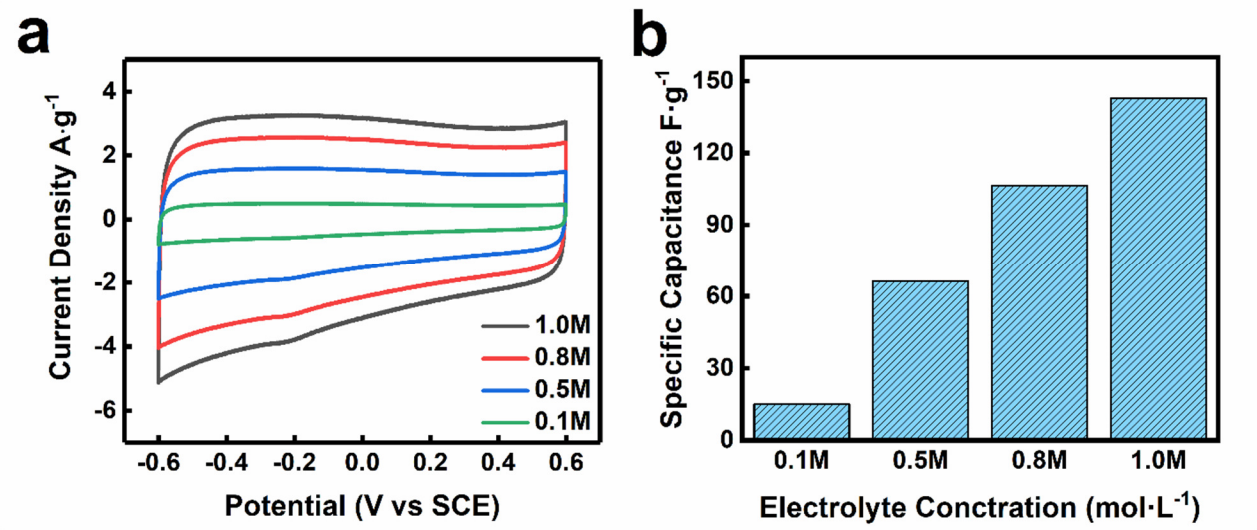

Figure A2-6 (a) CV curves and (b) associated specific capacitance of 3DOM-TiN in 1.0, 0.8, 0.5, and 0.1 mol L^{-1} NaCl aqueous solutions.

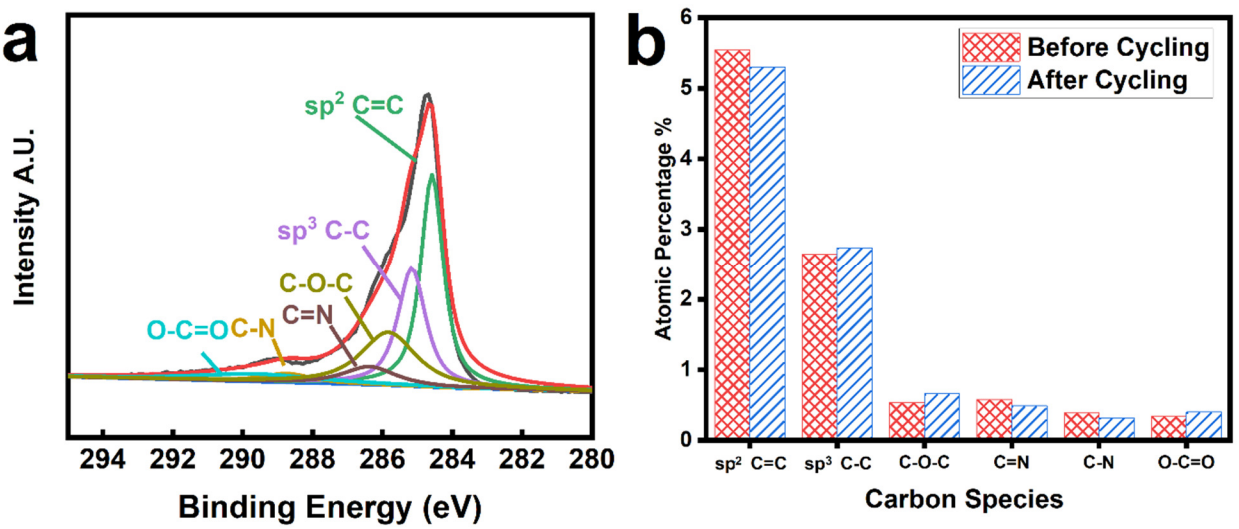

Figure A2-7 (a) high-resolution C1s XPS of 3DOM-TiN after 5000 cycles of stability test in half-cell and associated (b) comparison of the carbon species before and after cycling.

According to the high-resolution C 1s XPS after 5000 cycles of stability test in half-cell (**Figure A2-7a**), the sp^2 hybridized carbon still accounts the most in the 3DOM-TiN. Although the oxidization of NCR-coating was observed according to the increase in oxygenated carbon species and sp^3 hybridized carbon (**Figure A2-7b**), the insignificant decease of the sp^2 hybridized carbon (~ 4 %) shows sufficient stability and resistivity to oxidation of NCR-coating for CDI application.

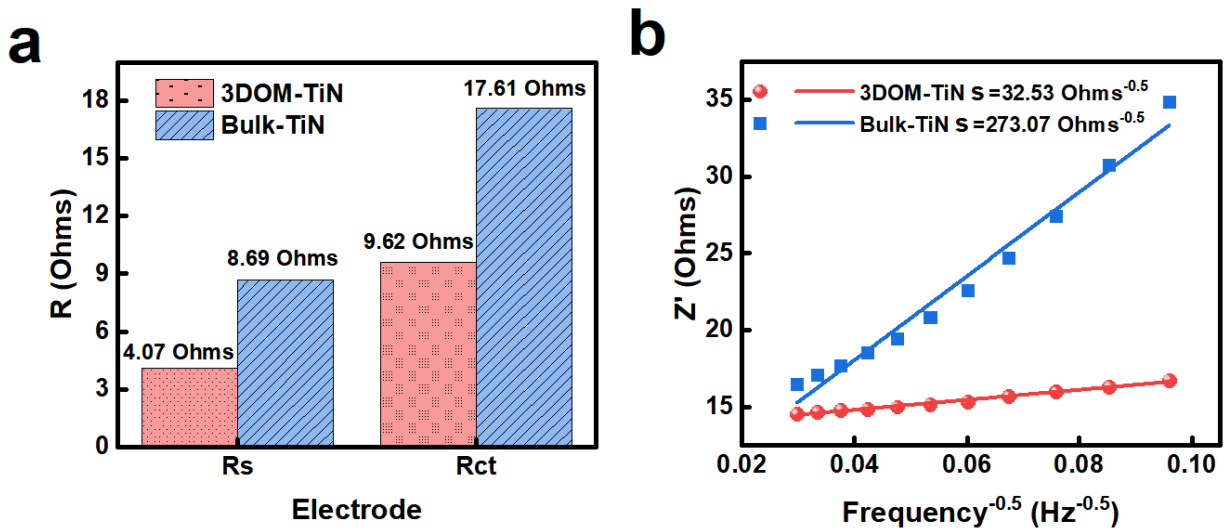

Figure A2-8 (a) System resistance (R_s) and charge transfer resistance (R_{ct}) of the 3DOM-TiN and bulk-TiN electrodes; (b) Linear fitting to the real part of impedance (Z') versus the −1/2 power of the angular frequency ($\omega^{-0.5}$) plots.

The Warburg coefficient σ (ohm $s^{-0.5}$) was extracted by fitting the real part of impedance (*Z'*) versus the -1/2 power of the angular frequency ($\omega^{-0.5}$) plots in a frequency range of 1 to 10 Hz. The steeper linear line and smaller diffusion Warburg coefficient σ indicated the higher efficiency of ion diffusion of 3DOM-TiN compared with bulk-TiN.[243, 244]

Calculation of the Pseudo-capacitance

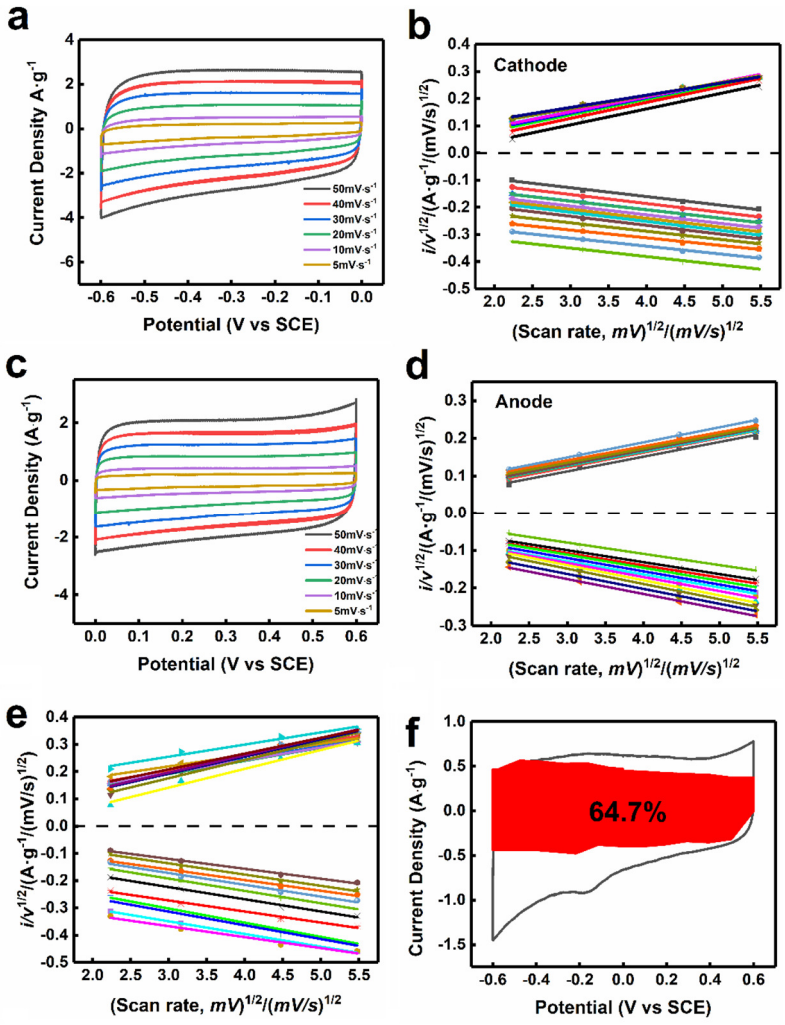

Figure A2-9 CV curves of 3DOM-TiN in 1M NaCl solution with varying scan rates and associated linear fitting of $i/v^{1/2}$ vs $v^{1/2}$ in (a, b) cathodic range (-0.6 ~ 0V) and (c, d) anodic range (0 – 0.6 V) ; (e) Linear fitting of $i/v^{1/2}$ vs $v^{1/2}$ of 3DOM-TiN in 1M NaCl solution with varying scan rates in the full range (-0.6 ~ 0.6V) and (f) associated Dunn method analysis of capacitance contribution of 3DOM-TiN at scan rate of 10 mV s^{-1} in the same potential range. The shaded regions show the current contributions from the electrical double-layer capacitive processes.

Dunn's method is generally described as follows. The quantity analysis of the capacitance contributions from the surface capacitive effects (C_{EDL}) and diffusion-controlled process (pseudo capacitance) is enabled by Dunn's method.[245] The current density (i) from the CVs can be expressed as the following two parts, k_1v and $k_2v^{0.5}$, at a fixed potential:

$$i = k_1 v + k_2 v^{0.5} \qquad \textbf{(A2-1)}$$

Where the first part, k_1v accounts for the current density contributed from the EDL capacitive, while $k_2v^{0.5}$ accounts for the current density contributed from the pseudo-capacitance. The equation can be rearranged by dividing the $v^{0.5}$ on both sides:

$$iv^{-0.5} = k_1 v^{0.5} + k_2 \qquad \textbf{(A2-2)}$$

Thus, by extracting the i from the CVs at each scan rates v and plotting the $iv^{-0.5}$ vs. $v^{0.5}$, a linear fitted line with the slope of k_1 and y-intercept of k_2 can be obtained. **Figure A2-9** displays the contributions of C_{EDL} and pseudo capacitance of the 3DOM-TiN electrode as cathode, anode and a full-scan CV from both cathode and anode, together with the $iv^{-0.5}$ vs. $v^{0.5}$ and their linear fitting process. Using the k_1 and k_2 obtained from the linear fitting, the contribution of C_{EDL} and pseudo capacitance can be calculated at specific potential V and scan rate, v.

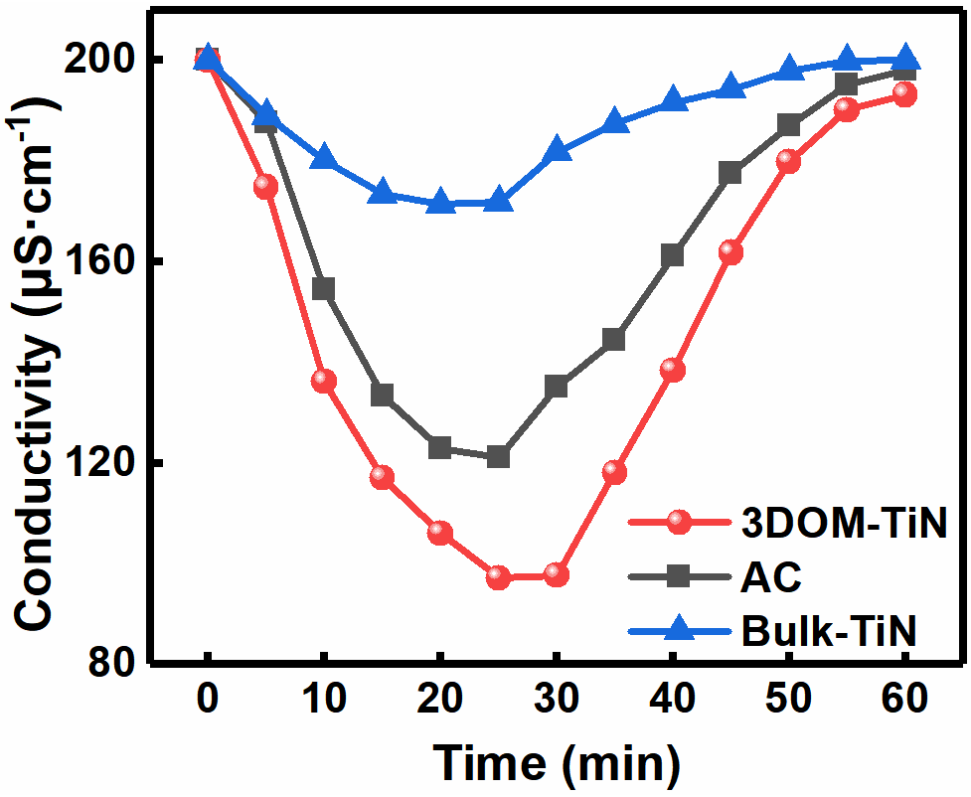

Figure A2-10 Conductivity profile of saline water during batch-mode CDI process using 3DOM-TiN, Bulk-TiN and AC electrodes with applied potential of 1.2 V and initial salinity of 100 mg L^{-1}.

All three electrodes reached their lowest conductivity at around 25 minutes, which is the maximum salt adsorption capacity moment. After 25 minutes, although the electrodes kept absorbing salt, the capacity declined rapidly, which is not energy and cost effective. Thus, the salt adsorption capacity of the electrode was determined at the lowest conductivity moment.

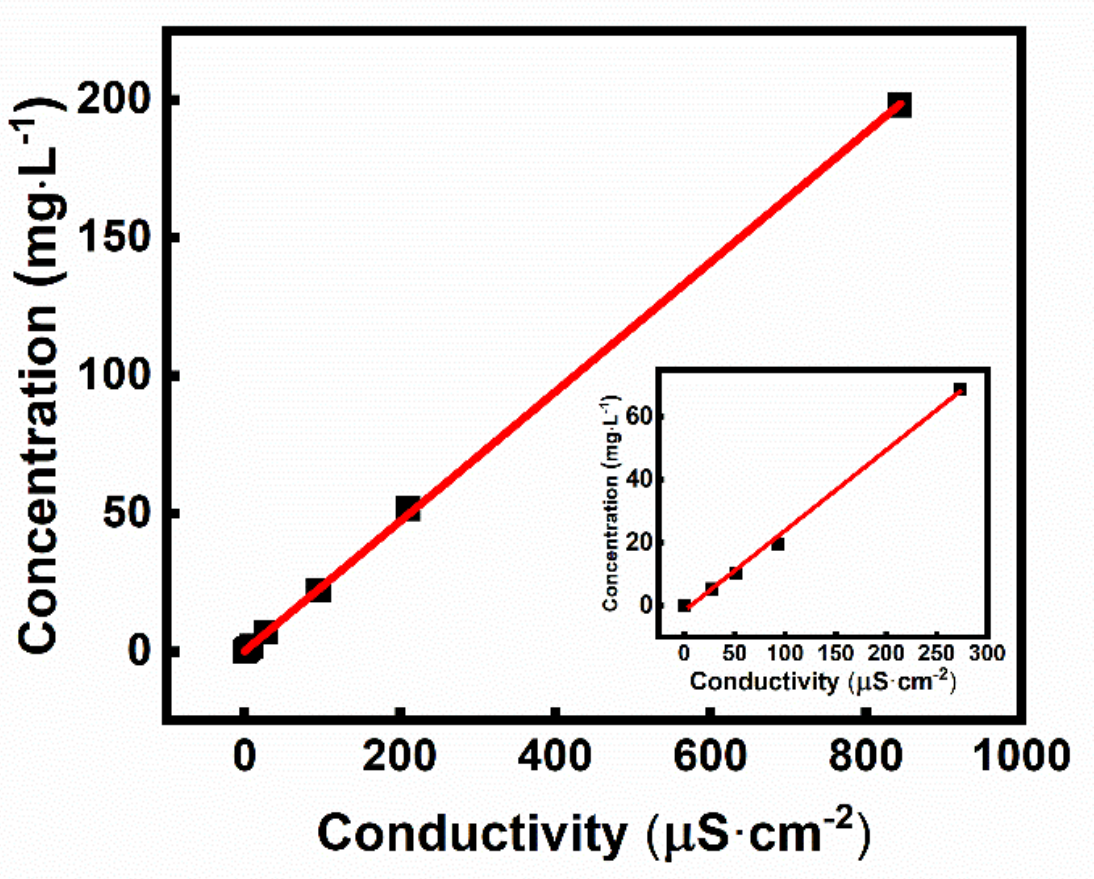

Figure A2-11 Calibration of the Conductivity to NaCl Concentration. The inserted graph is the enlarged part from 0-300 μS/cm^2.

The salinity of the water is based on a series calibration with a series of standard NaCl solutions. The calibrated equation of Conductivity-Concentration is:

$$\text{Concentration (mg/L)} = 0.04699 * \text{Conductivity}(\mu\text{S}) + 2.33873 \quad (\mathbf{A2\text{-}3})$$

Where R^2=0.99998, indicating that the salinity of the solution can be considered as linearly dependent on the conductivity.

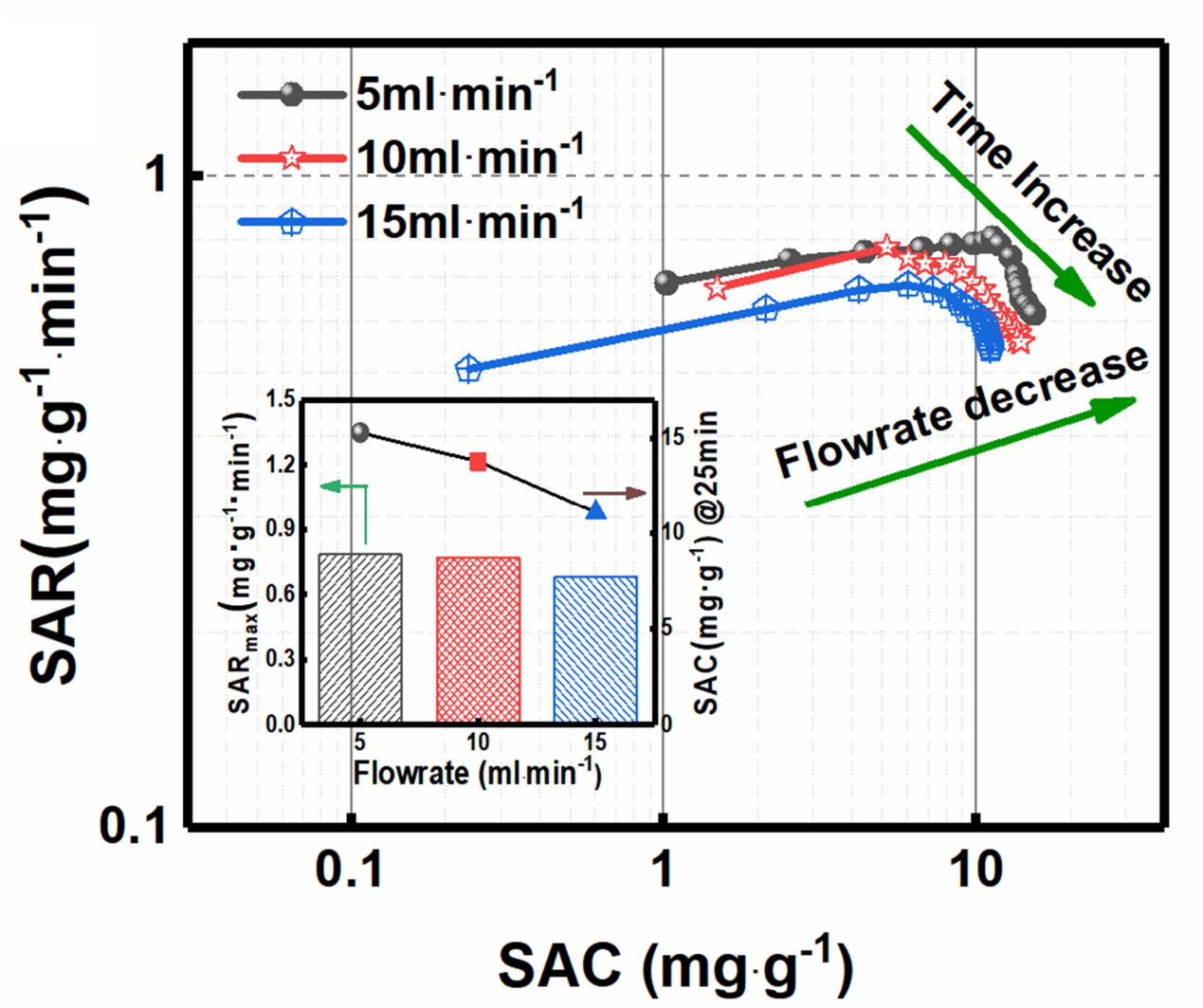

Figure A2-12 Ragone plots of SAR vs. SAC for 3DOM-TiN electrode in continuous symmetric CDI cell obtained under different flow rates; the inset plots illustrate the maximum SAR and SAC at 25 min.

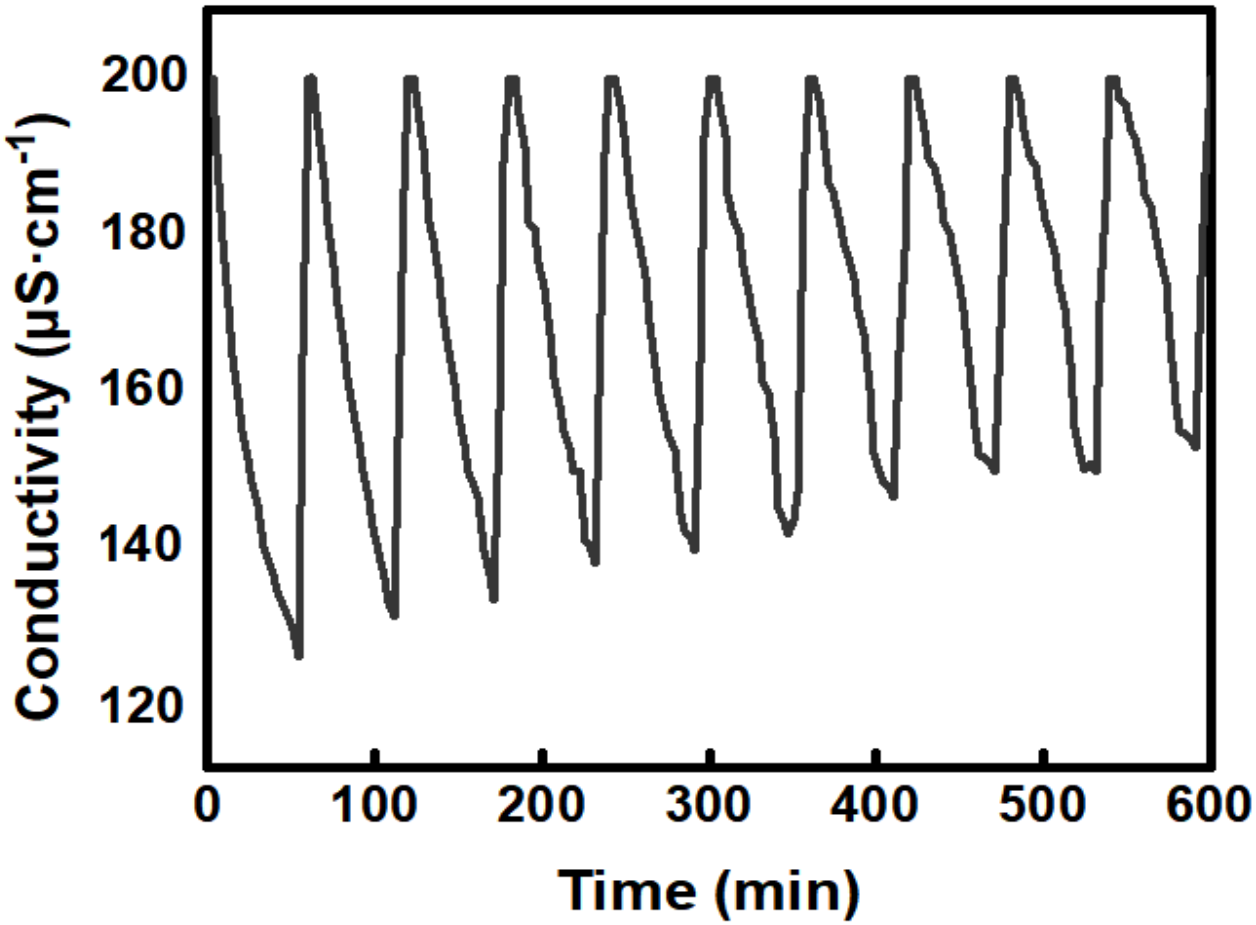

Figure A2-13 Regeneration cycling stability test of AC electrode in continuous symmetric CDI cell with saline water (100 mg L^{-1} NaCl) flow through at 5 ml min^{-1} at applied voltage of 1.2 V.

Supplemental XRD comparison

This figure contains a series of unpublished preliminary characterizations in studying the transformation temperature of N-doped TiO_2 to TiN.

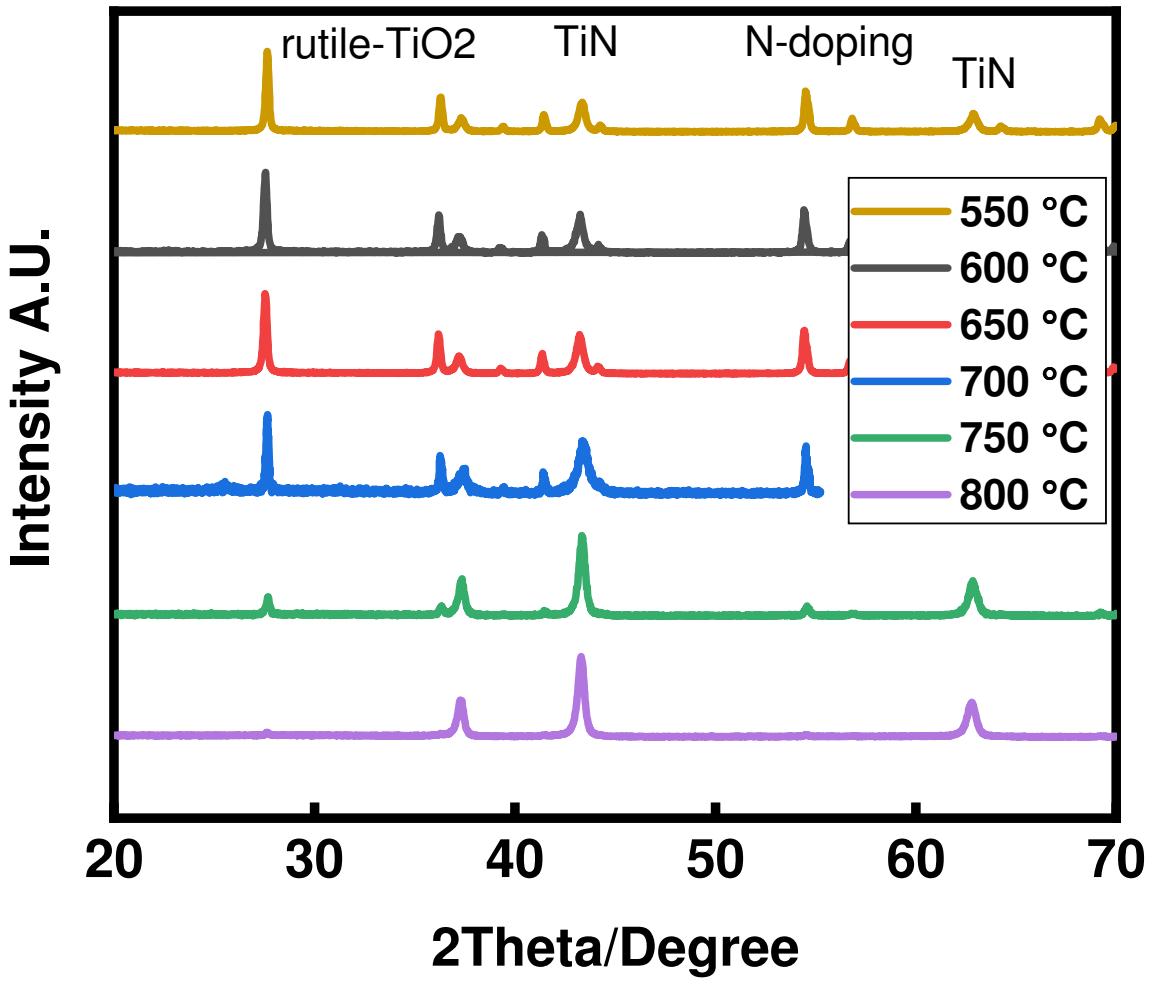

Figure A2-14 XRD patterns of TiO_2-TiN under different calcination temperature.

As temperature increased from 600°C to 800°C, the N-doped TiO_2 XRD patterns transformed into TiN pattern. Thus, the nitridation temperature is set as 800°C.

Supplemental Tables

Table A2- 1 BET surface area and pore volume of 3DOM-TiN and bulk-TiN.

	BET Surface Area $m^2\ g^{-1}$	BET Pore Volume $cm^3\ g^{-1}$
3DOM-TiN	141.61	0.291
Bulk-TiN	31.65	0.030

Table A2-2 Lattice constants and N/Ti ratio of 3DOM-TiN and bulk-TiN

	2θ °	d (220) Å	a Å	x (TiN_x)
3DOM-TiN	61.945	1.4986	4.2386	0.9872
Bulk-TiN	62.332	1.4931	4.2232	0.6574

The d_{220} is determined according to Bragg's law:

$$d_{220} = \frac{n\lambda}{2sin\theta} \qquad \textbf{(A2-4)}$$

TiN_x lattice parameter is then calculated:

$$a_{TiN_x} = d_{220}\sqrt{h^2 + k^2 + l^2} \qquad \textbf{(A2-5)}$$

From the obtained values of lattice parameters, the N/Ti ratio of 3DOM-TiN and bulk-TiN were calculated[246]:

$$a_{TiN_x} = 4.1925 + 0.0467x \qquad \textbf{(A2-6)}$$

Table A2-3 Elemental composition of 3DOM-TiN via XPS survey and EDX spectrum.

	Ti	C	N	O
XPS survey (wt%)	65.95	9.96	12.87	11.22
EDX spectrum (wt%)	64.35	10.80	11.32	13.53

Table A2-4 Salt adsorption capacity comparison of several commercial and titanium-based CDI electrodes

Electrode	Cell Voltage V	Salinity mg l^{-1}	SAC mg g^{-1}	References
Commercial Activated Carbon	1.2	292-1170	10.9~13.0	[67]
Commercial Carbon Aerogel	1.2	50~500	1.4~2.9	[45]
Commercial Activated Carbon	1.2	292	10.5	[179]
rGO-Ti	1.2	300	9.2~13.2	[174]
CNT-Ti	1.2	500	~4.3	[232]
Ti-AC	1.2	500	~2.7	[175]
Ti NPs/AC	1.2	100	~8.04	[51]
3D-GA/TiO_2	1.2	100	~23	[139]
Ti_3C_2-Mxene	1.2	100	13	[176]
Activated Carbon	1.2	100	~13.7	This Work
Bulk-TiN	1.2	100	~4.5	This Work
3DOM-TiN	1.2	100	~22.1	This Work
3DOM-TiN	1.2	500	23.6	This work

Table A2-5 Comparison of salt adsorption rate of this work with several carbon-based electrode materials for capacitive deionization

Electrode	Working Condition			SAR_{max} mg g^{-1} min^{-1}	References
	Voltage V	Flow rate ml min^{-1}	Salinity mg L^{-1}		
3DOM-TiN	1.2	5	500	~3.2	This work
Bulk-TiN	1.2	5	100	0.09	This work
Activated Carbon	1.2	5	100	0.4	This work
N-doped mesoporous Carbon	1.2	5	500	0.2~1.2	[247]
Porous Carbon membrane	1.2	60	1000	0.2~0.3	[179]
N, P, S co-doped hollow carbon polyhedra	1.2	50	500	0.5	[141]
Surface-treated carbon	1.2~1.4	8.6	500	1.2	[248]
High-performance activated carbon	1.2~1.4	26	600	0.2	[249]
Macro/Micropore Carbon	1.2	50~500	500	1.2	[184]
Graphene sheet	1.2	20~80	500	0.8	[250]
Nitrogen-doped graphene composites	1.4	N/A	300	~2.0	[251]
Porous carbon nanosheet	1.2	66.9	1000	1.0	[252]
$Na_3V_2(PO_4)_3$@C	1.0	15	585	2.4	[253]

Table A2-6 Comparison of salt adsorption rate of this work with several metal-based electrode materials for capacitive deionization

Electrode	Working Condition			SAR_{max} mg g^{-1} min^{-1}	References
	Voltage V	Flow rate ml min^{-1}	Salinity mg L^{-1}		
3DOM-TiN	1.2	5	500	~3.2	This work
Bulk-TiN	1.2	5	100	0.09	This work
Activated Carbon	1.2	5	100	0.4	This work
$Na_4Mn_9O_{18}$	1.2	10	500	~0.4	[254]
$Na_2FeP_2O_7$	0.9~1.5	2	584.4	0.48	[177]
MnO_2 electroless deposition	1.2	5	100	3.0	[251]
Ti_3C_2-Mexene	1.2	22	500	1.0	[176]
TiO_2-coated AC	1.0	N/A	500~1000	2~3	[178]

Appendix C

Calibration of SCE electrode

The SCE electrode was calibrated in NaCl solution using SCE to Reversible Hydrogen Electrode (RHE) in an open circuit as shown in **Figure A3-1**. The result was adding +0.5V to the potential of SCE in NaCl solution, which means the -1V to 0V was -0.5V to 0.5V in actual.

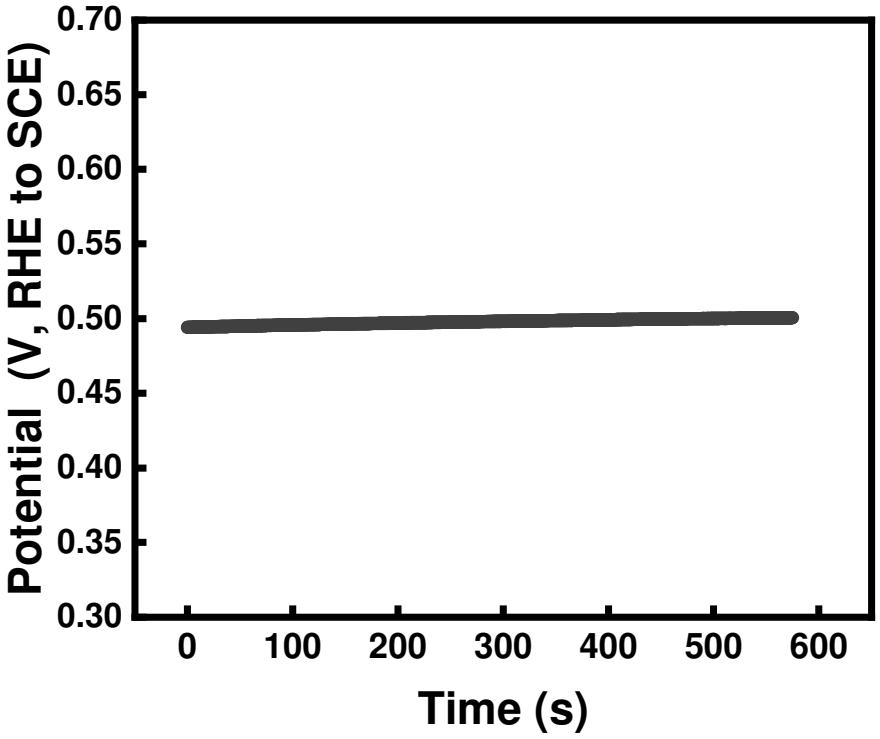

Figure A3-1 Open circuit plot of SCE to RHE vs time.

Calibration of conductivity-salinity

The salinity of the water is based on a series calibration with a series of standard NaCl solution.

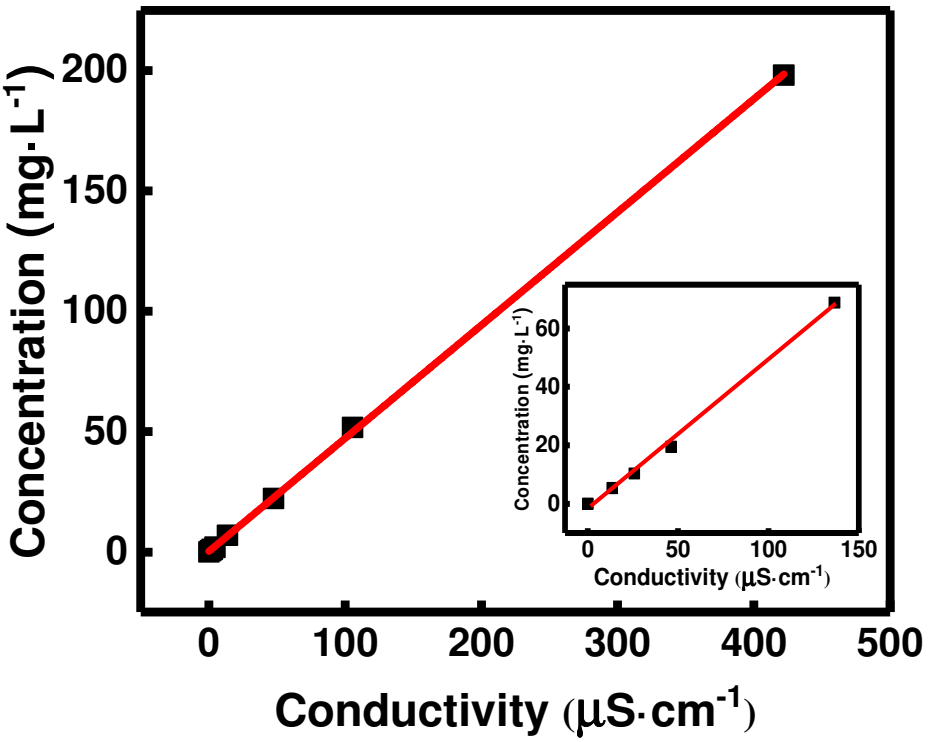

Figure A3-2 Calibration of the Conductivity to NaCl Concentration. The inserted graph is the enlarged part from 0-300 µS/cm^2.

The calibrated **Equation A3-1** of Conductivity-Concentration is:

$$C = 2.33873 * \text{Conductivity}(\mu S) + 3.60607 \qquad (\mathbf{A3\text{-}1})$$

Where the R^2=0.99993, indicating that the salinity of the solution can be considered as a linear dependent to the conductivity.

Supporting XRD information

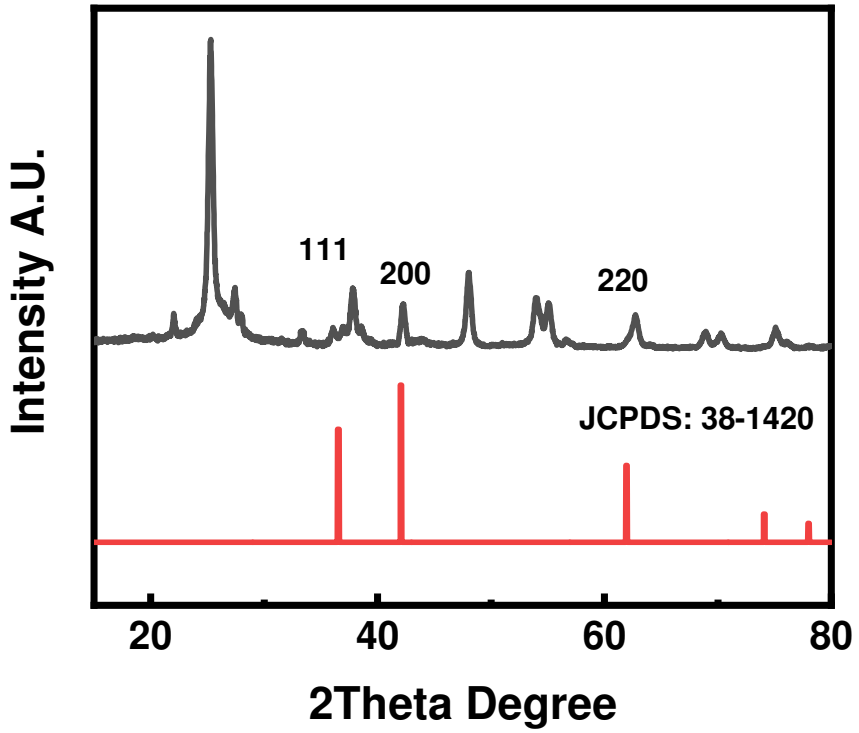

Figure A3-3 XRD Patterns of NG-TiO_xN_y and JCPDS card of TiN

Supplemental SEM information

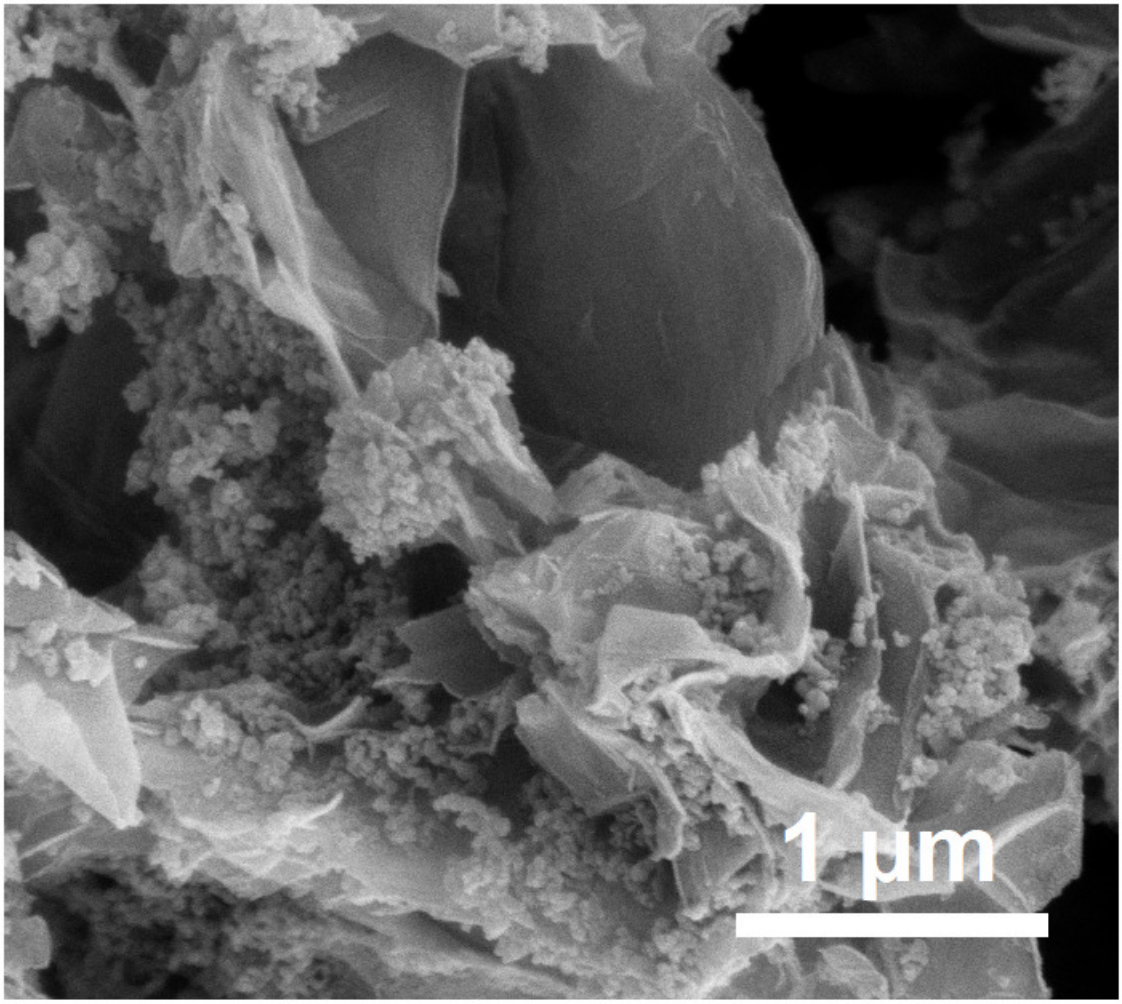

Figure A3-4 Low magnification SEM image of the NG-TiO_xN_y .

Supplemental XPS wide survey

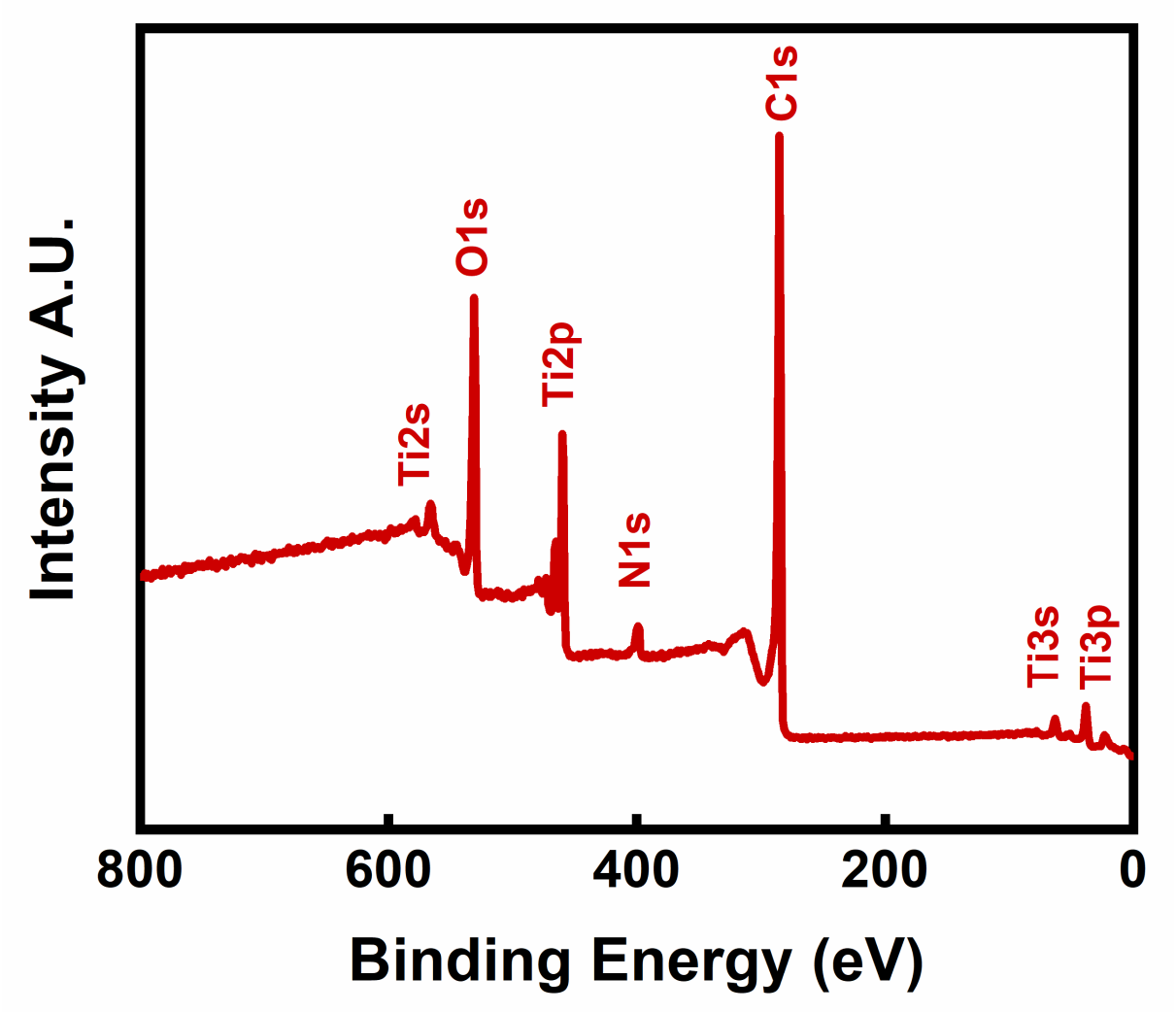

Figure A3-5 XPS survey of the NG-TiO_xN_y.

Supplemental Ti 2p scan information

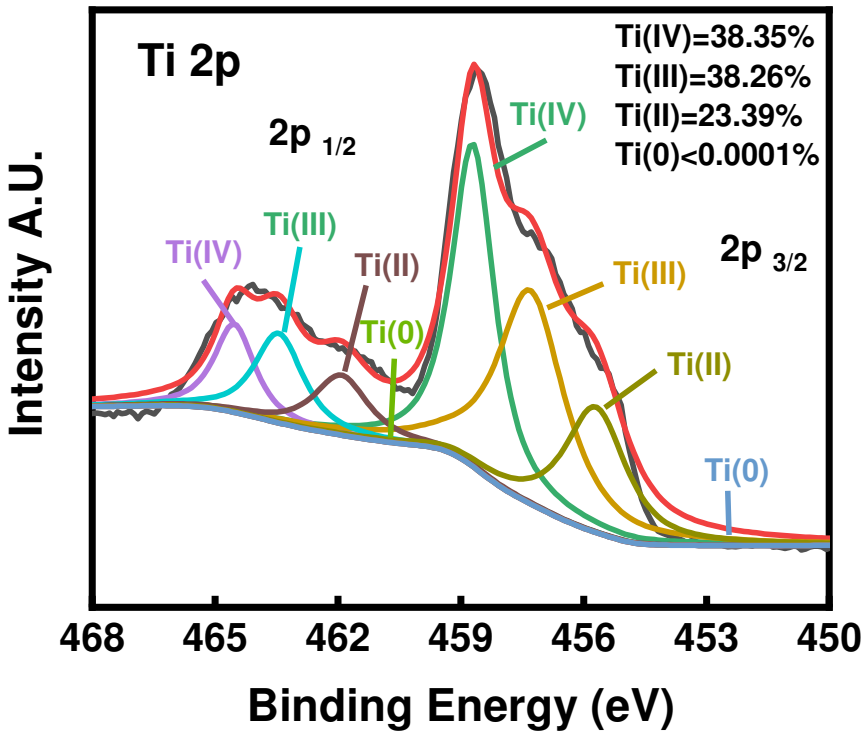

Figure A3-6 Ti 2p XPS analysis of various Ti states.

Schematic of a flow-by CDI process

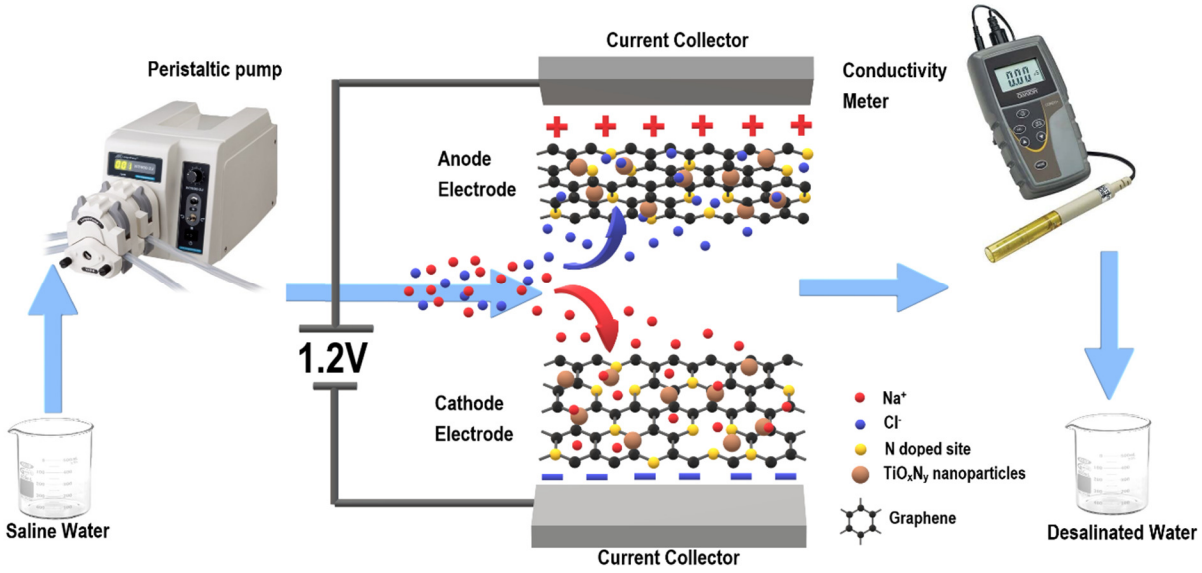

Figure A3-7 Schematic of a flow-by CDI process.

Comparison of several CDI electrode materials for CDI in phase two preliminary research.

This figure is a comparison for several unpublished CDI electrode materials tested in phase two study, it contains experimental data related to Chapter 5. The red, blue and green dots are the raw SAC experimental data of a single-batch mode CDI test. The columns are the average SAC of each electrodes. The CDI cells and working conditions are the same to Chapter 5 & 6 with feed in 500mg L^{-1} saline water.

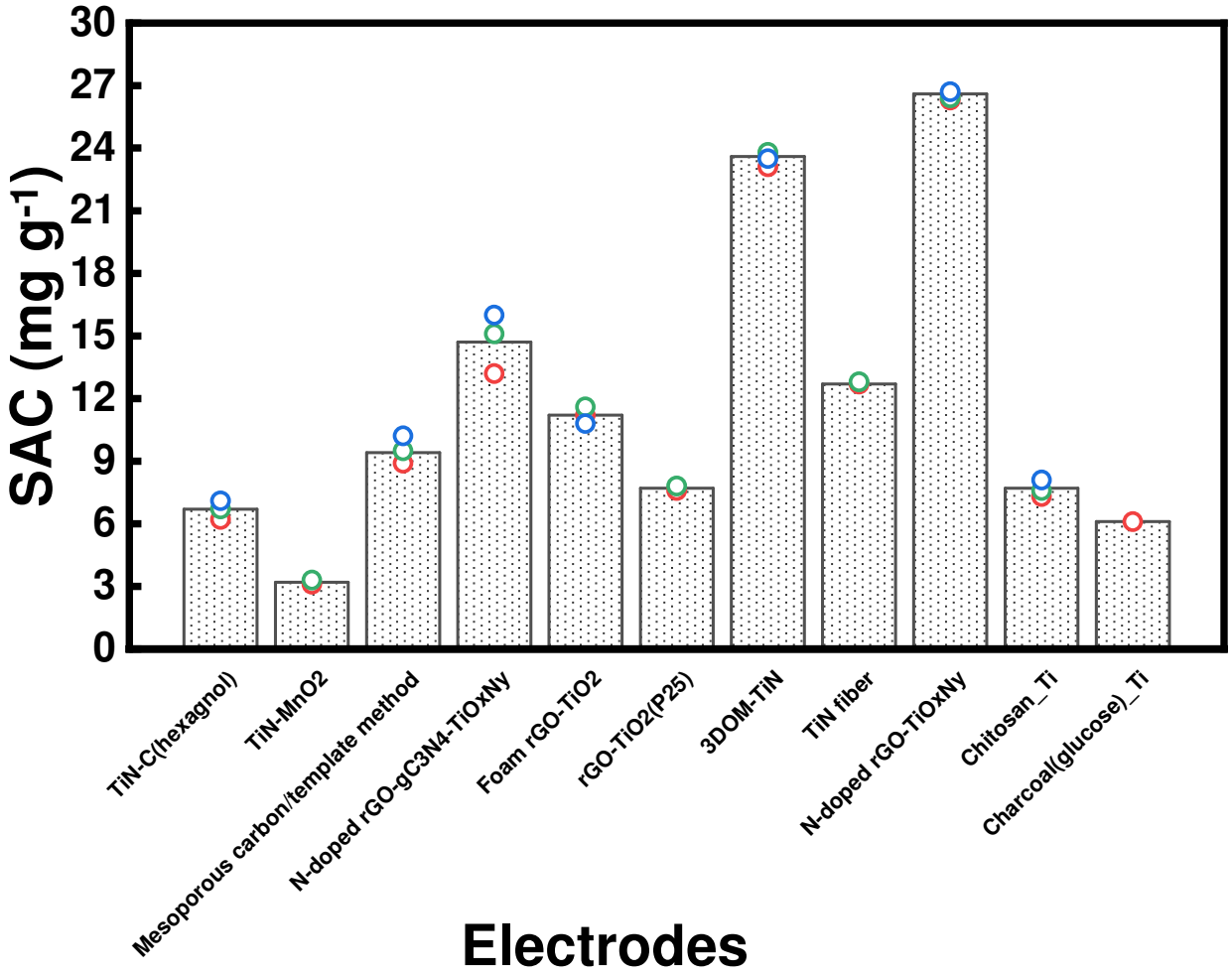

Figure A3-8 Comparsion of several CDI electrode materials for CDI.

Supplemental Tables

Table A3-1 Lattice constants and N/Ti ratio of NG-TiO_xN_y.

	2θ/°	$d_{(220)}$ / Å	a/ Å	y
NG-TiO_xN_y	62.371	1.490	4.2211	0.6122

In this study, we conducted the nitridation process by the ammonia treatment of solid rGO-TiO_2 rather than the gaseous titanium precursor such as titanium tetrachloride. Thus, the nitridation is insufficient and the degree of nitridation is relatively low. Here, we made an attempt to calculate N/Ti ratio (*y*) using the reported method and XRD data listed in **Table A3-1**.[246]

The d_{220} is determined according to Bragg's law:

$$d_{220} = \frac{n\lambda}{2\sin\theta} \qquad (\mathbf{A3\text{-}2})$$

TiN lattice parameter is then calculated:

$$a_{TiN_y} = d_{220}\sqrt{h^2 + k^2 + l^2} \qquad (\mathbf{A3\text{-}3})$$

From the obtained values of lattice parameters, the N/Ti ratio of TiO_xN_y in NG-TiO_xN_y is calculated:

$$a_{TiN_y} = 4.1925 + 0.0467y \qquad (\mathbf{A3\text{-}4})$$

Thus, the value of *y* is roughly 0.61 in the NG-TiO_xN_y nanocomposite. However, there is no fixed stoichiometry between nitrogen and titanium in titanium nitride. The N/Ti ratio varies from 0.6 to 1.2 and depends on the degree of nitridation.[255] In our design, the mass ratio of GO to TiO_2, the mass of rGO-TiO_2 charged in the ceramic boat, the porosity and morphology of rGO-TiO_2 as well as other experimental factors may affect the degree of nitridation. Thus, the value of *y* varies from sample to sample and from batch to batch.

Table A3-2 Oxidization states and atom percentage of Ti species in NG-TiO_xN_y.

i	Ti (IV)	Ti (III)	Ti (II)	Ti (0)
$O_{Ti(i)}$	+4	+3	+2	0
$P_{Ti(i)}$/%	38.35	38.26	23.39	~0

According to Fig. R1, four different oxidation states were observed for Ti in NG-TiO_xN_y, namely Ti(IV), Ti(III), Ti(II) and Ti(0).[256, 257] The average oxidation state of titanium is calculated via the following equation:

$$Ti_{average} = \sum \left(O_{Ti(i)} \times P_{Ti(i)} \right) \quad \textbf{(A3-5)}$$

Where the $O_{Ti(i)}$ and $P_{Ti(i)}$ are the oxidation state and corresponding atom percentage of each Ti species. The values are listed in the above **Table A3-5**.

Thus, the calculated average oxidation state of Ti is +3.1497.

It is assumed that the oxidation states of all the nitrogen (O_N) and oxygen (O_O) that were bonded with Ti in the NG-TiO_xN_y composite are -3 and -2, respectively. Then, with the N/Ti ratio (y) calculated as 0.6122, the value of x can be calculated as follows:

$$x = -\frac{Ti_{average} + y * O_N}{O_O} \quad \textbf{(A3-6)}$$

Then, we obtained the value of x as 0.6565， roughly 0.66.

References

1. Catley-Carlson, M., Environment: Water, water everywhere. *Nature* **2011,** *473*, 27.
2. Ang, W. L.; Mohammad, A. W.; Hilal, N.; Leo, C. P., A review on the applicability of integrated/hybrid membrane processes in water treatment and desalination plants. *Desalination* **2015,** *363*, 2-18.
3. López-Maldonado, E.; Oropeza-Guzman, M.; Jurado-Baizaval, J.; Ochoa-Terán, A., Coagulation–flocculation mechanisms in wastewater treatment plants through zeta potential measurements. *Journal of hazardous materials* **2014,** *279*, 1-10.
4. Rahman, M. F.; Peldszus, S.; Anderson, W. B., Behaviour and fate of perfluoroalkyl and polyfluoroalkyl substances (PFASs) in drinking water treatment: a review. *Water research* **2014,** *50*, 318-340.
5. Park, H.; Lim, S.-i.; Lee, H.; Woo, D.-S., Water blending effects on coagulation-flocculation using aluminum sulfate (alum), polyaluminum chloride (PAC), and ferric chloride (FeCl3) using multiple water sources. *Desalination and Water Treatment* **2016,** *57* (16), 7511-7521.
6. Sun, H.; Shi, S.; Wang, P., Research on the application of several complex magnetic flocculants to restaurant wastewater. *Industrial Water Treatment* **2006,** *26* (8), 55-58.

7. Wang, S.-K.; Wang, F.; Hu, Y.-R.; Stiles, A. R.; Guo, C.; Liu, C.-Z., Magnetic flocculant for high efficiency harvesting of microalgal cells. *ACS applied materials & interfaces* **2013,** *6* (1), 109-115.

8. AlMarzooqi, F. A.; Al Ghaferi, A. A.; Saadat, I.; Hilal, N., Application of Capacitive Deionisation in water desalination: A review. *Desalination* **2014,** *342*, 3-15.

9. Ghaffour, N.; Missimer, T. M.; Amy, G. L., Technical review and evaluation of the economics of water desalination: current and future challenges for better water supply sustainability. *Desalination* **2013,** *309*, 197-207.

10. Oren, Y., Capacitive deionization (CDI) for desalination and water treatment—past, present and future (a review). *Desalination* **2008,** *228* (1), 10-29.

11. Arnold, B. B.; Murphy, G. W., Studies on the electrochemistry of carbon and chemically-modified carbon surfaces. *The Journal of Physical Chemistry* **1961,** *65* (1), 135-138.

12. Johnson, A.; Venolia, A.; Newman, J.; Wilbourne, R.; Wong, C.; Gillam, W., Electrosorb process for desalting water, Office of Saline Water Research and Development. In *Progress Report No 516, US Department of the Interior, Publication 200 056*, 1970.

13. Soffer, A.; Folman, M., The electrical double layer of high surface porous carbon electrode. *Journal of Electroanalytical Chemistry and Interfacial Electrochemistry* **1972,** *38* (1), 25-43.

14. Farmer, J. C.; Fix, D. V.; Mack, G. V.; Pekala, R. W.; Poco, J. F. In *The use of capacitive deionization with carbon aerogel electrodes to remove inorganic contaminants from water*, Low level waste conference, Orlando, 1995.

15. Jia, B.; Zhang, W., Preparation and Application of Electrodes in Capacitive Deionization (CDI): a State-of-Art Review. *Nanoscale research letters* **2016,** *11* (1), 1.

16. Chabot, V.; Higgins, D.; Yu, A.; Xiao, X.; Chen, Z.; Zhang, J., A review of graphene and graphene oxide sponge: material synthesis and applications to energy and the environment. *Energy & Environmental Science* **2014,** *7* (5), 1564-1596.

17. Hummers Jr, W. S.; Offeman, R. E., Preparation of graphitic oxide. *Journal of the American Chemical Society* **1958,** *80* (6), 1339-1339.

18. Kyzas, G. Z.; Deliyanni, E. A.; Matis, K. A., Graphene oxide and its application as an adsorbent for wastewater treatment. *Journal of Chemical Technology and Biotechnology* **2014,** *89* (2), 196-205.

19. Zhao, G.; Ren, X.; Gao, X.; Tan, X.; Li, J.; Chen, C.; Huang, Y.; Wang, X., Removal of Pb (II) ions from aqueous solutions on few-layered graphene oxide nanosheets. *Dalton Transactions* **2011,** *40* (41), 10945-10952.

20. Mi, X.; Huang, G.; Xie, W.; Wang, W.; Liu, Y.; Gao, J., Preparation of graphene oxide aerogel and its adsorption for Cu 2+ ions. *Carbon* **2012,** *50* (13), 4856-4864.

21. Liu, M.; Chen, C.; Hu, J.; Wu, X.; Wang, X., Synthesis of magnetite/graphene oxide composite and application for cobalt (II) removal. *The Journal of Physical Chemistry C* **2011,** *115* (51), 25234-25240.

22. Yang, X.; Zhang, F.; Zhang, L.; Zhang, T.; Huang, Y.; Chen, Y., A High‐Performance Graphene Oxide‐Doped Ion Gel as Gel Polymer Electrolyte for All‐Solid‐State Supercapacitor Applications. *Advanced Functional Materials* **2013,** *23* (26), 3353-3360.

23. O'Hern, S. C.; Boutilier, M. S. H.; Idrobo, J.-C.; Song, Y.; Kong, J.; Laoui, T.; Atieh, M.; Karnik, R., Selective Ionic Transport through Tunable Subnanometer Pores in Single-Layer Graphene Membranes. *Nano Letters* **2014,** *14* (3), 1234-1241.

24. Montes-Navajas, P.; Asenjo, N. G.; Santamaría, R.; Menéndez, R.; Corma, A.; García, H., Surface Area Measurement of Graphene Oxide in Aqueous Solutions. *Langmuir* **2013,** *29* (44), 13443-13448.

25. Ramesha, G.; Kumara, A. V.; Muralidhara, H.; Sampath, S., Graphene and graphene oxide as effective adsorbents toward anionic and cationic dyes. *Journal of colloid and interface science* **2011,** *361* (1), 270-277.

26. He, G.; Liu, W.; Sun, X.; Chen, Q.; Wang, X.; Chen, H., Fe3O4@graphene oxide composite: A magnetically separable and efficient catalyst for the reduction of nitroarenes. *Materials Research Bulletin* **2013,** *48* (5), 1885-1890.

27. Zhang, D.; Liu, Z.; Han, S.; Li, C.; Lei, B.; Stewart, M. P.; Tour, J. M.; Zhou, C., Magnetite (Fe3O4) Core−Shell Nanowires: Synthesis and Magnetoresistance. *Nano Letters* **2004,** *4* (11), 2151-2155.

28. Sun, H.; Cao, L.; Lu, L., Magnetite/reduced graphene oxide nanocomposites: one step solvothermal synthesis and use as a novel platform for removal of dye pollutants. *Nano Research* **2011,** *4* (6), 550-562.

29. Chandra, V.; Park, J.; Chun, Y.; Lee, J. W.; Hwang, I.-C.; Kim, K. S., Water-Dispersible Magnetite-Reduced Graphene Oxide Composites for Arsenic Removal. *ACS Nano* **2010,** *4* (7), 3979-3986.

30. Chen, H.; Deng, C.; Zhang, X., Synthesis of Fe3O4@ SiO2@ PMMA Core–Shell–Shell Magnetic Microspheres for Highly Efficient Enrichment of Peptides and Proteins for MALDI-ToF MS Analysis. *Angewandte Chemie International Edition* **2010,** *49* (3), 607-611.

31. Kumar, A.; Kumar, A.; Sharma, G.; Al-Muhtaseb, A. a. H.; Naushad, M.; Ghfar, A. A.; Stadler, F. J., Quaternary magnetic BiOCl/g-C3N4/Cu2O/Fe3O4 nano-junction for visible light and solar powered degradation of sulfamethoxazole from aqueous environment. *Chemical Engineering Journal* **2018,** *334*, 462-478.

32. Wang, R.; Wang, X.; Xi, X.; Hu, R.; Jiang, G., Preparation and photocatalytic activity of magnetic Fe3O4/SiO2/TiO2 composites. *Advances in Materials Science and Engineering* **2012,** *2012*.

33. Delahay, P.; Susbielles, G. G., Double-layer impedance of electrodes with charge-transfer reaction. *The Journal of Physical Chemistry* **1966,** *70* (10), 3150-3157.

34. Johnson, A.; Newman, J., Desalting by means of porous carbon electrodes. *Journal of the Electrochemical Society* **1971,** *118* (3), 510-517.

35. Bockris, J. O. M.; Reddy, A. K., *Modern Electrochemistry 2B: Electrodics in Chemistry, Engineering, Biology and Environmental Science*. Springer Science & Business Media: 2001; Vol. 2.

36. Whitney, R. B.; Grahame, D. C., A modified theory of the electrical double layer. *The Journal of Chemical Physics* **1941,** *9* (11), 827-828.

37. Gouy, G., J. de Phys. 9, 457 (1910); DL Chapman. *Phil. Mag* **1913,** *25*, 475.

38. Bolt, G., Analysis of the validity of the Gouy-Chapman theory of the electric double layer. *Journal of Colloid Science* **1955,** *10* (2), 206-218.

39. Biesheuvel, P., Thermodynamic cycle analysis for capacitive deionization. *Journal of colloid and interface science* **2009,** *332* (1), 258-264.

40. Biesheuvel, P. M.; van Limpt, B.; van der Wal, A., Dynamic Adsorption/Desorption Process Model for Capacitive Deionization. *The Journal of Physical Chemistry C* **2009,** *113* (14), 5636-5640.

41. Biesheuvel, P.; Porada, S.; Levi, M.; Bazant, M. Z., Attractive forces in microporous carbon electrodes for capacitive deionization. *Journal of solid state electrochemistry* **2014,** *18* (5), 1365-1376.

42. Shocron, A. N.; Suss, M. E., The effect of surface transport on water desalination by porous electrodes undergoing capacitive charging. *arXiv preprint arXiv:1607.06350* **2016**.

43. Appel, J., Freundlich's adsorption isotherm. *Surface Science* **1973,** *39* (1), 237-244.

44. Gabelich, C. J.; Tran, T. D.; Suffet, I. M., Electrosorption of inorganic salts from aqueous solution using carbon aerogels. *Environmental science & technology* **2002,** *36* (13), 3010-3019.

45. Dermentzis, K., Brackish Water Desalination by Capacitive Deionization using Nanoporous Carbon Aerogel Electrodes. *Journal of Engineering Science and Technology Review* **2016,** *9* (3), 130-133.

46. Bansal, R. C.; Goyal, M., *Activated carbon adsorption*. CRC press: 2005.

47. Teng, H.; Yeh, T.-S.; Hsu, L.-Y., Preparation of activated carbon from bituminous coal with phosphoric acid activation. *Carbon* **1998,** *36* (9), 1387-1395.

48. Murphy, G. W., Activated carbon used as electrodes in electrochemical demineralization of saline water. **1969**.

49. Liao, J.-Y.; Higgins, D.; Lui, G.; Chabot, V.; Xiao, X.; Chen, Z., Multifunctional TiO2–C/MnO2 core–double-shell nanowire arrays as high-performance 3D electrodes for lithium ion batteries. *Nano letters* **2013,** *13* (11), 5467-5473.

50. Ryoo, M.-W.; Seo, G., Improvement in capacitive deionization function of activated carbon cloth by titania modification. *Water Research* **2003,** *37* (7), 1527-1534.

51. Liu, P.-I.; Chung, L.-C.; Shao, H.; Liang, T.-M.; Horng, R.-Y.; Ma, C.-C. M.; Chang, M.-C., Microwave-assisted ionothermal synthesis of nanostructured anatase titanium dioxide/activated carbon composite as electrode material for capacitive deionization. *Electrochimica Acta* **2013,** *96*, 173-179.

52. Kim, C.; Lee, J.; Kim, S.; Yoon, J., TiO2 sol–gel spray method for carbon electrode fabrication to enhance desalination efficiency of capacitive deionization. *Desalination* **2014,** *342*, 70-74.

53. Si, Y.; Samulski, E. T., Synthesis of water soluble graphene. *Nano letters* **2008,** *8* (6), 1679-1682.

54. Kim, F.; Cote, L. J.; Huang, J., Graphene Oxide: Surface Activity and Two-Dimensional Assembly. *Advanced Materials* **2010,** *22* (17), 1954-1958.

55. Stoller, M. D.; Park, S.; Zhu, Y.; An, J.; Ruoff, R. S., Graphene-based ultracapacitors. *Nano letters* **2008,** *8* (10), 3498-3502.

56. Wang, Z.; Wu, S.; Zhang, J.; Chen, P.; Yang, G.; Zhou, X.; Zhang, Q.; Yan, Q.; Zhang, H., Comparative studies on single-layer reduced graphene

oxide films obtained by electrochemical reduction and hydrazine vapor reduction. *Nanoscale Research Letters* **2012,** *7* (1), 161-161.

57. Zhu, X.; Zhu, Y.; Murali, S.; Stoller, M. D.; Ruoff, R. S., Nanostructured reduced graphene oxide/Fe2O3 composite as a high-performance anode material for lithium ion batteries. *Acs Nano* **2011,** *5* (4), 3333-3338.

58. Shao, Y.; Zhang, S.; Engelhard, M. H.; Li, G.; Shao, G.; Wang, Y.; Liu, J.; Aksay, I. A.; Lin, Y., Nitrogen-doped graphene and its electrochemical applications. *Journal of Materials Chemistry* **2010,** *20* (35), 7491-7496.

59. Jung, I.; Dikin, D. A.; Piner, R. D.; Ruoff, R. S., Tunable electrical conductivity of individual graphene oxide sheets reduced at "low" temperatures. *Nano Letters* **2008,** *8* (12), 4283-4287.

60. Farmer, J. C.; Fix, D. V.; Mack, G. V.; Pekala, R. W.; Poco, J. F., Capacitive deionization of NaCl and NaNO3 solutions with carbon aerogel electrodes. *Journal of the Electrochemical Society* **1996,** *143* (1), 159-169.

61. Chen, Z.; Song, C.; Sun, X.; Guo, H.; Zhu, G., Kinetic and isotherm studies on the electrosorption of NaCl from aqueous solutions by activated carbon electrodes. *Desalination* **2011,** *267* (2), 239-243.

62. Dai, K.; Shi, L.; Fang, J.; Zhang, D.; Yu, B., NaCl adsorption in multi-walled carbon nanotubes. *Materials Letters* **2005,** *59* (16), 1989-1992.

63. Wang, X.; Li, M.; Chen, Y.; Cheng, R.; Huang, S.; Pan, L.; Sun, Z., Electrosorption of NaCl solutions with carbon nanotubes and nanofibers composite film electrodes. *Electrochemical and solid-state letters* **2006,** *9* (9), E23-E26.

64. Zou, L.; Li, L.; Song, H.; Morris, G., Using mesoporous carbon electrodes for brackish water desalination. *Water research* **2008,** *42* (8), 2340-2348.

65. Li, H.; Lu, T.; Pan, L.; Zhang, Y.; Sun, Z., Electrosorption behavior of graphene in NaCl solutions. *Journal of Materials Chemistry* **2009,** *19* (37), 6773-6779.

66. Kim, Y.-J.; Choi, J.-H., Enhanced desalination efficiency in capacitive deionization with an ion-selective membrane. *Separation and Purification Technology* **2010,** *71* (1), 70-75.

67. Zhao, R.; Biesheuvel, P. M.; Miedema, H.; Bruning, H.; van der Wal, A., Charge Efficiency: A Functional Tool to Probe the Double-Layer Structure Inside of Porous Electrodes and Application in the Modeling of Capacitive Deionization. *The Journal of Physical Chemistry Letters* **2010,** *1* (1), 205-210.

68. Li, H.; Zou, L.; Pan, L.; Sun, Z., Novel graphene-like electrodes for capacitive deionization. *Environmental science & technology* **2010,** *44* (22), 8692-8697.

69. Li, H.; Pan, L.; Lu, T.; Zhan, Y.; Nie, C.; Sun, Z., A comparative study on electrosorptive behavior of carbon nanotubes and graphene for capacitive deionization. *Journal of Electroanalytical Chemistry* **2011,** *653* (1), 40-44.

70. Biesheuvel, P.; Zhao, R.; Porada, S.; Van der Wal, A., Theory of membrane capacitive deionization including the effect of the electrode pore space. *Journal of Colloid and Interface Science* **2011,** *360* (1), 239-248.

71. Yang, J.; Zou, L.; Song, H.; Hao, Z., Development of novel MnO 2/nanoporous carbon composite electrodes in capacitive deionization technology. *Desalination* **2011,** *276* (1), 199-206.

72. Wang, G.; Pan, C.; Wang, L.; Dong, Q.; Yu, C.; Zhao, Z.; Qiu, J., Activated carbon nanofiber webs made by electrospinning for capacitive deionization. *Electrochimica Acta* **2012,** *69*, 65-70.

73. Jia, B.; Zou, L., Wettability and its influence on graphene nansoheets as electrode material for capacitive deionization. *Chemical Physics Letters* **2012,** *548*, 23-28.

74. Wang, Z.; Dou, B.; Zheng, L.; Zhang, G.; Liu, Z.; Hao, Z., Effective desalination by capacitive deionization with functional graphene nanocomposite as novel electrode material. *Desalination* **2012,** *299*, 96-102.

75. Porada, S.; Bryjak, M.; Van Der Wal, A.; Biesheuvel, P., Effect of electrode thickness variation on operation of capacitive deionization. *Electrochimica Acta* **2012,** *75*, 148-156.

76. Villar, I.; Roldan, S.; Ruiz, V.; Granda, M.; Blanco, C.; Menéndez, R.; Santamaría, R., Capacitive deionization of NaCl solutions with modified activated carbon electrodes†. *Energy & Fuels* **2010,** *24* (6), 3329-3333.

77. Lee, J.-B.; Park, K.-K.; Yoon, S.-W.; Park, P.-Y.; Park, K.-I.; Lee, C.-W., Desalination performance of a carbon-based composite electrode. *Desalination* **2009,** *237* (1), 155-161.

78. Liu, Q.; Wang, Y.; Zhang, Y.; Xu, S.; Wang, J., Effect of dopants on the adsorbing performance of polypyrrole/graphite electrodes for capacitive deionization process. *Synthetic Metals* **2012,** *162* (7), 655-661.

79. Myint, M. T. Z.; Al-Harthi, S. H.; Dutta, J., Brackish water desalination by capacitive deionization using zinc oxide micro/nanostructures grafted on activated carbon cloth electrodes. *Desalination* **2014,** *344*, 236-242.

80. Wen, X.; Zhang, D.; Shi, L.; Yan, T.; Wang, H.; Zhang, J., Three-dimensional hierarchical porous carbon with a bimodal pore arrangement for capacitive deionization. *Journal of Materials Chemistry* **2012,** *22* (45), 23835-23844.

81. Bouhadana, Y.; Avraham, E.; Soffer, A.; Aurbach, D., Several basic and practical aspects related to electrochemical deionization of water. *AIChE journal* **2010,** *56* (3), 779-789.

82. Wang, L.; Wang, M.; Huang, Z.-H.; Cui, T.; Gui, X.; Kang, F.; Wang, K.; Wu, D., Capacitive deionization of NaCl solutions using carbon nanotube sponge electrodes. *Journal of Materials Chemistry* **2011,** *21* (45), 18295-18299.

83. Nie, C.; Pan, L.; Li, H.; Chen, T.; Lu, T.; Sun, Z., Electrophoretic deposition of carbon nanotubes film electrodes for capacitive deionization. *Journal of Electroanalytical Chemistry* **2012,** *666*, 85-88.

84. Shahriary, L.; Athawale, A. A., Graphene oxide synthesized by using modified hummers approach. *Int J Renew Energy Environ Eng* **2014,** *2*, 58-63.

85. Higgins, D.; Chen, Z.; Lee, D. U.; Chen, Z., Activated and nitrogen-doped exfoliated graphene as air electrodes for metal–air battery applications. *Journal of Materials Chemistry A* **2013,** *1* (7), 2639-2645.

86. Liu, Z.; Jin, Z.; Liu, X.; Fu, Y.; Liu, G., Fabrication of ordered TiO2 porous thin films by sol-dipping PS template method. *Journal of sol-gel science and technology* **2006,** *38* (1), 73-78.

87. Liu, Z.; Jin, Z.; Li, W.; Liu, X.; Qiu, J.; Wu, W., Preparation of porous ZnO plate crystal thin films by electrochemical deposition using PS template assistant. *Materials Letters* **2006,** *60* (6), 810-814.

88. Keeler, B. L.; Wood, S. A.; Polasky, S.; Kling, C.; Filstrup, C. T.; Downing, J. A., Recreational demand for clean water: evidence from geotagged photographs by visitors to lakes. *Frontiers in Ecology and the Environment* **2015,** *13* (2), 76-81.

89. Callahan, M. A., *Water-related environmental fate of 129 priority pollutants*. Office of Water Planning and Standards, Office of Water and Waste Management, US Environmental Protection Agency: 1979; Vol. 1.

90. Svoboda, J., A theoretical approach to the magnetic flocculation of weakly magnetic minerals. *International Journal of Mineral Processing* **1981,** *8* (4), 377-390.

91. Yadollahpour, A.; Rashidi, S.; Ghotbeddin, Z.; Jalilifar, M.; Rezaee, Z., Electromagnetic fields for the treatments of wastewater: a review of applications and future opportunities. *Journal of Pure & Applied Microbiology* **2014,** *8* (5), 3711-9.

92. Shen, Y. F.; Tang, J.; Nie, Z. H.; Wang, Y. D.; Ren, Y.; Zuo, L., Preparation and application of magnetic Fe3O4 nanoparticles for wastewater purification. *Separation and Purification Technology* **2009,** *68* (3), 312-319.

93. Edzwald, J., Coagulation in drinking water treatment: particles, organics and coagulants. *Water Science and Technology* **1993,** *27* (11), 21-35.

94. Zhu, Y.; Murali, S.; Cai, W.; Li, X.; Suk, J. W.; Potts, J. R.; Ruoff, R. S., Graphene and graphene oxide: synthesis, properties, and applications. *Advanced materials* **2010,** *22* (35), 3906-3924.

95. Chen, Y.; Chen, L.; Bai, H.; Li, L., Graphene oxide–chitosan composite hydrogels as broad-spectrum adsorbents for water purification. *Journal of Materials Chemistry A* **2013,** *1* (6), 1992-2001.

96. Zhao, G.; Li, J.; Ren, X.; Chen, C.; Wang, X., Few-layered graphene oxide nanosheets as superior sorbents for heavy metal ion pollution management. *Environmental science & technology* **2011,** *45* (24), 10454-10462.

97. Peng, G.; Zhang, M.; Deng, S.; Shan, D.; He, Q.; Yu, G., Adsorption and catalytic oxidation of pharmaceuticals by nitrogen-doped reduced graphene oxide/Fe3O4 nanocomposite. *Chemical Engineering Journal* **2018,** *341*, 361-370.

98. Benjwal, P.; Kumar, M.; Chamoli, P.; Kar, K. K., Enhanced photocatalytic degradation of methylene blue and adsorption of arsenic (iii) by reduced graphene oxide (rGO)–metal oxide (TiO 2/Fe 3 O 4) based nanocomposites. *Rsc Advances* **2015,** *5* (89), 73249-73260.

99. Sun, J.; Liang, Q.; Han, Q.; Zhang, X.; Ding, M., One-step synthesis of magnetic graphene oxide nanocomposite and its application in magnetic solid phase extraction of heavy metal ions from biological samples. *Talanta* **2015,** *132*, 557-563.

100. Peng, X.; An, J.; Xu, S.; Chen, W.; Xu, Z., Hydroiodic Acid Reduced Graphene Hybrid with δ-MnO2 for Electrode Material in Supercapacitors. *ECS Journal of Solid State Science and Technology* **2016,** *5* (6), M51-M57.

101. Luo, Y.; Balogun, M.-S.; Qiu, W.; Zhao, R.; Liu, P.; Tong, Y., Sulfurization of FeOOH nanorods on a carbon cloth and their conversion into Fe 2 O 3/Fe 3 O 4–S core– shell nanorods for lithium storage. *Chemical Communications* **2015,** *51* (65), 13016-13019.

102. Yamashita, T.; Hayes, P., Analysis of XPS spectra of Fe2+ and Fe3+ ions in oxide materials. *Applied Surface Science* **2008,** *254* (8), 2441-2449.

103. Yang, X.; Zhang, X.; Ma, Y.; Huang, Y.; Wang, Y.; Chen, Y., Superparamagnetic graphene oxide–Fe 3 O 4 nanoparticles hybrid for controlled targeted drug carriers. *Journal of Materials Chemistry* **2009,** *19* (18), 2710-2714.

104. Gu, F.; Liang, M.; Han, D.; Wang, Z., Multifunctional sandwich-like mesoporous silica–Fe 3 O 4–graphene oxide nanocomposites for removal of methylene blue from water. *RSC Advances* **2015,** *5* (50), 39964-39972.

105. Geng, Z.; Lin, Y.; Yu, X.; Shen, Q.; Ma, L.; Li, Z.; Pan, N.; Wang, X., Highly efficient dye adsorption and removal: a functional hybrid of reduced graphene oxide–Fe 3 O 4 nanoparticles as an easily regenerative adsorbent. *Journal of Materials Chemistry* **2012,** *22* (8), 3527-3535.

106. Wang, C.; Zhang, Q.; Wu, Q.-H.; Ng, T.-W.; Wong, T.; Ren, J.; Shi, Z.; Lee, C.-S.; Lee, S.-T.; Zhang, W., Facile synthesis of laminate-structured graphene sheet–Fe 3 O 4 nanocomposites with superior high reversible specific capacity and cyclic stability for lithium-ion batteries. *RSC Advances* **2012,** *2* (28), 10680-10688.

107. Aliofkhazraei, M.; Ali, N.; Milne, W. I.; Ozkan, C. S.; Mitura, S.; Gervasoni, J. L., *Graphene Science Handbook: Electrical and Optical Properties*. CRC Press: 2016.

108. Jasim, D. A.; Lozano, N.; Kostarelos, K., Synthesis of few-layered, high-purity graphene oxide sheets from different graphite sources for biology. *2D Materials* **2016,** *3* (1), 014006.

109. Zhao, Y.; Qiu, Z.; Huang, J., Preparation and Analysis of Fe3O4 Magnetic Nanoparticles Used as Targeted-drug Carriers*. *Chinese Journal of Chemical Engineering* **2008,** *16* (3), 451-455.

110. Yanase, A.; Siratori, K., Band structure in the high temperature phase of Fe3O4. *Journal of the Physical Society of Japan* **1984,** *53* (1), 312-317.

111. Hassan, F. M.; Chabot, V.; Li, J.; Kim, B. K.; Ricardez-Sandoval, L.; Yu, A., Pyrrolic-structure enriched nitrogen doped graphene for highly efficient next generation supercapacitors. *Journal of Materials Chemistry A* **2013,** *1* (8), 2904-2912.

112. Kudin, K. N.; Ozbas, B.; Schniepp, H. C.; Prud'Homme, R. K.; Aksay, I. A.; Car, R., Raman spectra of graphite oxide and functionalized graphene sheets. *Nano letters* **2008,** *8* (1), 36-41.

113. Ramesha, G. K.; Sampath, S., Electrochemical reduction of oriented graphene oxide films: an in situ Raman spectroelectrochemical study. *Journal of Physical Chemistry C* **2009,** *113* (19), 7985-7989.

114. Stankovich, S.; Dikin, D. A.; Piner, R. D.; Kohlhaas, K. A.; Kleinhammes, A.; Jia, Y.; Wu, Y.; Nguyen, S. T.; Ruoff, R. S., Synthesis of graphene-based nanosheets via chemical reduction of exfoliated graphite oxide. *carbon* **2007,** *45* (7), 1558-1565.

115. Tung, V. C.; Allen, M. J.; Yang, Y.; Kaner, R. B., High-throughput solution processing of large-scale graphene. *Nat Nanotechnol* **2009,** *4* (1), 25-29.

116. Cui, P.; Lee, J.; Hwang, E.; Lee, H., One-pot reduction of graphene oxide at subzero temperatures. *Chemical Communications* **2011,** *47* (45), 12370-12372.

117. King, A. A.; Davies, B. R.; Noorbehesht, N.; Newman, P.; Church, T. L.; Harris, A. T.; Razal, J. M.; Minett, A. I., A new Raman metric for the characterisation of graphene oxide and its derivatives. *Scientific reports* **2016,** *6*, 19491.

118. Jiang, Y.; Jiang, Z.-J.; Yang, L.; Cheng, S.; Liu, M., A high-performance anode for lithium ion batteries: Fe 3 O 4 microspheres encapsulated in hollow graphene shells. *Journal of Materials Chemistry A* **2015,** *3* (22), 11847-11856.

119. Dong, X.; Li, L.; Zhao, C.; Liu, H.-K.; Guo, Z., Controllable synthesis of RGO/Fe x O y nanocomposites as high-performance anode materials for lithium ion batteries. *Journal of Materials Chemistry A* **2014,** *2* (25), 9844-9850.

120. Langmuir, I., The adsorption of gases on plane surfaces of glass, mica and platinum. *Journal of the American Chemical society* **1918,** *40* (9), 1361-1403.

121. Mittal, A.; Kurup, L.; Mittal, J., Freundlich and Langmuir adsorption isotherms and kinetics for the removal of Tartrazine from aqueous solutions using hen feathers. *Journal of hazardous materials* **2007,** *146* (1-2), 243-248.

122. Ho, Y.-S.; McKay, G., Pseudo-second order model for sorption processes. *Process biochemistry* **1999,** *34* (5), 451-465.

123. Li, Y.; Du, Q.; Liu, T.; Peng, X.; Wang, J.; Sun, J.; Wang, Y.; Wu, S.; Wang, Z.; Xia, Y., Comparative study of methylene blue dye adsorption onto

activated carbon, graphene oxide, and carbon nanotubes. *Chemical Engineering Research and Design* **2013,** *91* (2), 361-368.

124. Qiu, H.; Lv, L.; Pan, B.-c.; Zhang, Q.-j.; Zhang, W.-m.; Zhang, Q.-x., Critical review in adsorption kinetic models. *Journal of Zhejiang University-SCIENCE A* **2009,** *10* (5), 716-724.

125. Azizian, S.; Bashiri, H., Adsorption kinetics at the solid/solution interface: statistical rate theory at initial times of adsorption and close to equilibrium. *Langmuir* **2008,** *24* (20), 11669-11676.

126. Subramani, A.; Jacangelo, J. G., Emerging desalination technologies for water treatment: a critical review. *Water research* **2015,** *75*, 164-187.

127. Choi, J.; Dorji, P.; Shon, H. K.; Hong, S., Applications of capacitive deionization: Desalination, softening, selective removal, and energy efficiency. *Desalination* **2019,** *449*, 118-130.

128. Teow, Y. H.; Mohammad, A. W., New generation nanomaterials for water desalination: a review. *Desalination* **2019,** *451*, 2-17.

129. Andelman, M., Flow through capacitor basics. *Separation and purification technology* **2011,** *80* (2), 262-269.

130. Singh, K.; Porada, S.; de Gier, H.; Biesheuvel, P.; de Smet, L., Timeline on the application of intercalation materials in Capacitive Deionization. *Desalination* **2019,** *455*, 115-134.

131. Zhao, Y.; Wang, Y.; Wang, R.; Wu, Y.; Xu, S.; Wang, J., Performance comparison and energy consumption analysis of capacitive deionization and membrane capacitive deionization processes. *Desalination* **2013,** *324*, 127-133.

132. Qin, M.; Deshmukh, A.; Epsztein, R.; Patel, S. K.; Owoseni, O. M.; Walker, W. S.; Elimelech, M., Comparison of energy consumption in desalination by capacitive deionization and reverse osmosis. *Desalination* **2019,** *455*, 100-114.

133. Bao, W.; Tang, X.; Guo, X.; Choi, S.; Wang, C.; Gogotsi, Y.; Wang, G., Porous cryo-dried MXene for efficient capacitive deionization. *Joule* **2018,** *2* (4), 778-787.

134. Lim, L.; Liu, Y.; Liu, W.; Tjandra, R.; Rasenthiram, L.; Chen, Z.; Yu, A., All-in-one graphene based composite fiber: toward wearable supercapacitor. *ACS applied materials & interfaces* **2017,** *9* (45), 39576-39583.

135. Luo, G.; Wang, Y.; Gao, L.; Zhang, D.; Lin, T., Graphene bonded carbon nanofiber aerogels with high capacitive deionization capability. *Electrochimica Acta* **2018,** *260*, 656-663.

136. Li, Y.; Liu, Y.; Wang, M.; Xu, X.; Lu, T.; Sun, C. Q.; Pan, L., Phosphorus-doped 3D carbon nanofiber aerogels derived from bacterial-cellulose for highly-efficient capacitive deionization. *carbon* **2018,** *130*, 377-383.

137. Wimalasiri, Y.; Zou, L., Carbon nanotube/graphene composite for enhanced capacitive deionization performance. *Carbon* **2013,** *59*, 464-471.

138. Gao, T.; Zhou, F.; Ma, W.; Li, H., Metal-organic-framework derived carbon polyhedron and carbon nanotube hybrids as electrode for electrochemical supercapacitor and capacitive deionization. *Electrochimica Acta* **2018,** *263*, 85-93.

139. Yin, H.; Zhao, S.; Wan, J.; Tang, H.; Chang, L.; He, L.; Zhao, H.; Gao, Y.; Tang, Z., Three‐dimensional graphene/metal oxide nanoparticle hybrids for high‐performance capacitive deionization of saline water. *Advanced materials* **2013,** *25* (43), 6270-6276.

140. Wang, H.; Shi, L.; Yan, T.; Zhang, J.; Zhong, Q.; Zhang, D., Design of graphene-coated hollow mesoporous carbon spheres as high performance electrodes for capacitive deionization. *Journal of Materials Chemistry A* **2014,** *2* (13), 4739-4750.

141. Zhang, J.; Fang, J.; Han, J.; Yan, T.; Shi, L.; Zhang, D., N, P, S co-doped hollow carbon polyhedra derived from MOF-based core–shell nanocomposites for capacitive deionization. *Journal of Materials Chemistry A* **2018,** *6* (31), 15245-15252.

142. Higgins, D. C.; Choi, J.-Y.; Wu, J.; Lopez, A.; Chen, Z., Titanium nitride–carbon nanotube core–shell composites as effective electrocatalyst supports for low temperature fuel cells. *Journal of Materials Chemistry* **2012,** *22* (9), 3727-3732.

143. Xing, Z.; Li, G.; Sy, S.; Chen, Z., Recessed deposition of TiN into N-doped carbon as a cathode host for superior Li-S batteries performance. *Nano Energy* **2018,** *54*, 1-9.

144. Morozov, I. G.; Belousova, O.; Belyakov, O.; Parkin, I.; Sathasivam, S.; Kuznetcov, M., Titanium nitride room-temperature ferromagnetic nanoparticles. *Journal of Alloys and Compounds* **2016,** *675*, 266-276.

145. Sait, R. A.; Cross, R. B. M., Synthesis and characterization of sputtered titanium nitride as a nucleation layer for novel neural electrode coatings. *Applied Surface Science* **2017,** *424*, 290-298.

146. Lui, G.; Li, G.; Wang, X.; Jiang, G.; Lin, E.; Fowler, M.; Yu, A.; Chen, Z., Flexible, three-dimensional ordered macroporous TiO2 electrode with enhanced electrode–electrolyte interaction in high-power Li-ion batteries. *Nano Energy* **2016,** *24*, 72-77.

147. Gray, B. M.; Hector, A. L.; Jura, M.; Owen, J. R.; Whittam, J., Effect of oxidative surface treatments on charge storage at titanium nitride surfaces for

supercapacitor applications. *Journal of Materials Chemistry A* **2017,** *5* (9), 4550-4559.

148. Zhu, C.; Yang, P.; Chao, D.; Wang, X.; Zhang, X.; Chen, S.; Tay, B. K.; Huang, H.; Zhang, H.; Mai, W., All Metal Nitrides Solid‐State Asymmetric Supercapacitors. *Advanced Materials* **2015,** *27* (31), 4566-4571.

149. Hasegawa, G.; Kitada, A.; Kawasaki, S.; Kanamori, K.; Nakanishi, K.; Kobayashi, Y.; Kageyama, H.; Abe, T., Impact of electrolyte on pseudocapacitance and stability of porous titanium nitride (TiN) monolithic electrode. *Journal of The Electrochemical Society* **2015,** *162* (1), A77-A85.

150. Lu, X.; Wang, G.; Zhai, T.; Yu, M.; Xie, S.; Ling, Y.; Liang, C.; Tong, Y.; Li, Y., Stabilized TiN nanowire arrays for high-performance and flexible supercapacitors. *Nano letters* **2012,** *12* (10), 5376-5381.

151. Dong, J.; Jiang, Y.; Li, Q.; Wei, Q.; Yang, W.; Tan, S.; Xu, X.; An, Q.; Mai, L., Pseudocapacitive titanium oxynitride mesoporous nanowires with iso-oriented nanocrystals for ultrahigh-rate sodium ion hybrid capacitors. *Journal of Materials Chemistry A* **2017,** *5* (22), 10827-10835.

152. Le, Z.; Liu, F.; Nie, P.; Li, X.; Liu, X.; Bian, Z.; Chen, G.; Wu, H. B.; Lu, Y., Pseudocapacitive sodium storage in mesoporous single-crystal-like TiO2–graphene nanocomposite enables high-performance sodium-ion capacitors. *ACS nano* **2017,** *11* (3), 2952-2960.

153. Tjandra, R.; Liu, W.; Lim, L.; Yu, A., Melamine based, n-doped carbon/reduced graphene oxide composite foam for Li-ion Hybrid Supercapacitors. *Carbon* **2018,** *129*, 152-158.

154. Lei, W.; Xiao, W.; Li, J.; Li, G.; Wu, Z.; Xuan, C.; Luo, D.; Deng, Y.-P.; Wang, D.; Chen, Z., Highly nitrogen-doped three-dimensional carbon fibers network with superior sodium storage capacity. *ACS applied materials & interfaces* **2017,** *9* (34), 28604-28611.

155. Hashemi, M.; Rahmanifar, M. S.; El-Kady, M. F.; Noori, A.; Mousavi, M. F.; Kaner, R. B., The use of an electrocatalytic redox electrolyte for pushing the energy density boundary of a flexible polyaniline electrode to a new limit. *Nano energy* **2018,** *44*, 489-498.

156. Yasin, A. S.; Mohamed, H. O.; Mohamed, I. M.; Mousa, H. M.; Barakat, N. A., Enhanced desalination performance of capacitive deionization using zirconium oxide nanoparticles-doped graphene oxide as a novel and effective electrode. *Separation and Purification Technology* **2016,** *171*, 34-43.

157. Achour, A.; Ducros, J. B.; Porto, R. L.; Boujtita, M.; Gautron, E.; Le Brizoual, L.; Djouadi, M. A.; Brousse, T., Hierarchical nanocomposite electrodes based on titanium nitride and carbon nanotubes for micro-supercapacitors. *Nano Energy* **2014,** *7*, 104-113.

158. Zhou, X.; Shang, C.; Gu, L.; Dong, S.; Chen, X.; Han, P.; Li, L.; Yao, J.; Liu, Z.; Xu, H.; Zhu, Y.; Cui, G., Mesoporous Coaxial Titanium Nitride-Vanadium Nitride Fibers of Core–shell Structures for High-Performance Supercapacitors. *ACS Applied Materials & Interfaces* **2011,** *3* (8), 3058-3063.

159. Zhou, Z.; Liu, T.; Khan, A. U.; Liu, G., Block copolymer–based porous carbon fibers. *Science Advances* **2019,** *5* (2), eaau6852.

160. Zhang, F.; Liu, T.; Li, M.; Yu, M.; Luo, Y.; Tong, Y.; Li, Y., Multiscale Pore Network Boosts Capacitance of Carbon Electrodes for Ultrafast Charging. *Nano Letters* **2017,** *17* (5), 3097-3104.

161. Costentin, C.; Porter, T. R.; Savéant, J.-M., How Do Pseudocapacitors Store Energy? Theoretical Analysis and Experimental Illustration. *ACS Applied Materials & Interfaces* **2017,** *9* (10), 8649-8658.

162. Brousse, T.; Bélanger, D.; Long, J. W., To be or not to be pseudocapacitive? *Journal of The Electrochemical Society* **2015,** *162* (5), A5185-A5189.

163. Liu, G.; Li, J.; Fu, J.; Jiang, G.; Lui, G.; Luo, D.; Deng, Y. P.; Zhang, J.; Cano, Z. P.; Yu, A., An Oxygen‐Vacancy‐Rich Semiconductor‐Supported Bifunctional Catalyst for Efficient and Stable Zinc–Air Batteries. *Advanced Materials* **2018**, 1806761.

164. Achour, A.; Porto, R. L.; Soussou, M.-A.; Islam, M.; Boujtita, M.; Aissa, K. A.; Le Brizoual, L.; Djouadi, A.; Brousse, T., Titanium nitride films for micro-supercapacitors: Effect of surface chemistry and film morphology on the capacitance. *Journal of Power Sources* **2015,** *300*, 525-532.

165. Achour, A.; Ducros, J.; Porto, R. L.; Boujtita, M.; Gautron, E.; Le Brizoual, L.; Djouadi, M.; Brousse, T., Hierarchical nanocomposite electrodes based on titanium nitride and carbon nanotubes for micro-supercapacitors. *Nano Energy* **2014,** *7*, 104-113.

166. Lu, X.; Wang, G.; Zhai, T.; Yu, M.; Gan, J.; Tong, Y.; Li, Y., Hydrogenated TiO2 nanotube arrays for supercapacitors. *Nano letters* **2012,** *12* (3), 1690-1696.

167. Ding, J.; Li, Z.; Cui, K.; Boyer, S.; Karpuzov, D.; Mitlin, D., Heteroatom enhanced sodium ion capacity and rate capability in a hydrogel derived carbon give record performance in a hybrid ion capacitor. *Nano Energy* **2016,** *23*, 129-137.

168. Xia, Q.; Yang, H.; Wang, M.; Yang, M.; Guo, Q.; Wan, L.; Xia, H.; Yu, Y., High Energy and High Power Lithium-Ion Capacitors Based on Boron and Nitrogen Dual-Doped 3D Carbon Nanofibers as Both Cathode and Anode. *Advanced Energy Materials* **2017,** *7* (22), 1701336.

169. Kim, T.; Yoon, J., CDI ragone plot as a functional tool to evaluate desalination performance in capacitive deionization. *RSC Advances* **2015,** *5* (2), 1456-1461.

170. Trefalt, G.; Behrens, S. H.; Borkovec, M., Charge regulation in the electrical double layer: ion adsorption and surface interactions. *Langmuir* **2015,** *32* (2), 380-400.

171. Hatlo, M. M.; Van Roij, R.; Lue, L., The electric double layer at high surface potentials: The influence of excess ion polarizability. *EPL (Europhysics Letters)* **2012,** *97* (2), 28010.

172. Yasin, A. S.; Mohamed, I. M.; Mousa, H. M.; Park, C. H.; Kim, C. S., Facile synthesis of TiO 2/ZrO 2 nanofibers/nitrogen co-doped activated carbon to enhance the desalination and bacterial inactivation via capacitive deionization. *Scientific reports* **2018,** *8* (1), 541.

173. S. Yasin, A.; Obaid, M.; Mohamed, I.; Yousef, A.; Barakat, N., *ZrO 2 nanofibers/activated carbon composite as a novel and effective electrode material for the enhancement of capacitive deionization performance*. 2017; Vol. 7, p 4616-4626.

174. El-Deen, A. G.; Choi, J.-H.; Kim, C. S.; Khalil, K. A.; Almajid, A. A.; Barakat, N. A., TiO2 nanorod-intercalated reduced graphene oxide as high

performance electrode material for membrane capacitive deionization. *Desalination* **2015,** *361*, 53-64.

175. Srimuk, P.; Zeiger, M.; Jäckel, N.; Tolosa, A.; Krüner, B.; Fleischmann, S.; Grobelsek, I.; Aslan, M.; Shvartsev, B.; Suss, M. E., Enhanced performance stability of carbon/titania hybrid electrodes during capacitive deionization of oxygen saturated saline water. *Electrochimica Acta* **2017,** *224*, 314-328.

176. Srimuk, P.; Kaasik, F.; Krüner, B.; Tolosa, A.; Fleischmann, S.; Jäckel, N.; Tekeli, M. C.; Aslan, M.; Suss, M. E.; Presser, V., MXene as a novel intercalation-type pseudocapacitive cathode and anode for capacitive deionization. *Journal of Materials Chemistry A* **2016,** *4* (47), 18265-18271.

177. Kim, S.; Lee, J.; Kim, C.; Yoon, J., Na2FeP2O7 as a Novel Material for Hybrid Capacitive Deionization. *Electrochimica Acta* **2016,** *203*, 265-271.

178. Min, B. H.; Choi, J.-H.; Jung, K. Y., Improved capacitive deionization of sulfonated carbon/titania hybrid electrode. *Electrochimica Acta* **2018,** *270*, 543-551.

179. Zhao, R.; Satpradit, O.; Rijnaarts, H.; Biesheuvel, P.; Van der Wal, A., Optimization of salt adsorption rate in membrane capacitive deionization. *Water research* **2013,** *47* (5), 1941-1952.

180. Santangelo, S., Electrospun Nanomaterials for Energy Applications: Recent Advances. *Applied Sciences* **2019,** *9* (6), 1049.

181. Oladunni, J.; Zain, J. H.; Hai, A.; Banat, F.; Bharath, G.; Alhseinat, E., A comprehensive review on recently developed carbon based nanocomposites for capacitive deionization: from theory to practice. *Separation and Purification Technology* **2018,** *207*, 291-320.

182. Porada, S.; Zhao, R.; van der Wal, A.; Presser, V.; Biesheuvel, P. M., Review on the science and technology of water desalination by capacitive deionization. *Progress in Materials Science* **2013,** *58* (8), 1388-1442.

183. Shi, K.; Zhitomirsky, I., Asymmetric Supercapacitors Based on Activated-Carbon-Coated Carbon Nanotubes. *ChemElectroChem* **2015,** *2* (3), 396-403.

184. Tang, K.; Chang, J.; Cao, H.; Su, C.; Li, Y.; Zhang, Z.; Zhang, Y., Macropore-and micropore-dominated carbon derived from poly (vinyl alcohol) and polyvinylpyrrolidone for supercapacitor and capacitive deionization. *ACS Sustainable Chemistry & Engineering* **2017,** *5* (12), 11324-11333.

185. Duan, F.; Du, X.; Li, Y.; Cao, H.; Zhang, Y., Desalination stability of capacitive deionization using ordered mesoporous carbon: Effect of oxygen-containing surface groups and pore properties. *Desalination* **2015,** *376*, 17-24.

186. Shi, K.; Yang, X.; Cranston, E. D.; Zhitomirsky, I., Efficient Lightweight Supercapacitor with Compression Stability. *Advanced Functional Materials* **2016,** *26* (35), 6437-6445.

187. Divyapriya, G.; Vijayakumar, K. K.; Nambi, I., Development of a novel graphene/Co3O4 composite for hybrid capacitive deionization system. *Desalination* **2019,** *451*, 102-110.

188. Khan, Z. U.; Yan, T.; Shi, L.; Zhang, D., Improved capacitive deionization by using 3D intercalated graphene sheet–sphere nanocomposite architectures. *Environmental Science: Nano* **2018,** *5* (4), 980-991.

189. Han, J.; Shi, L.; Yan, T.; Zhang, J.; Zhang, D., Removal of ions from saline water using N, P co-doped 3D hierarchical carbon architectures via capacitive deionization. *Environmental Science: Nano* **2018,** *5* (10), 2337-2345.

190. Choi, H.-J.; Jung, S.-M.; Seo, J.-M.; Chang, D. W.; Dai, L.; Baek, J.-B., Graphene for energy conversion and storage in fuel cells and supercapacitors. *Nano Energy* **2012,** *1* (4), 534-551.

191. Chang, J. H.; Huzayyin, A.; Lian, K.; Dawson, F., Quantum capacitance of graphene in contact with metal. *Applied Physics Letters* **2015,** *107* (19), 193902.

192. Luan, Z.; Tian, Y.; Gai, L.; Jiang, H.; Guo, X.; Yang, Y., Environment-benign synthesis of rGO/MnOx nanocomposites with superior

electrochemical performance for supercapacitors. *Journal of Alloys and Compounds* **2017,** *729*, 9-18.

193. He, Y.; Chen, W.; Li, X.; Zhang, Z.; Fu, J.; Zhao, C.; Xie, E., Freestanding Three-Dimensional Graphene/MnO2 Composite Networks As Ultralight and Flexible Supercapacitor Electrodes. *ACS Nano* **2013,** *7* (1), 174-182.

194. Abdelkader, A.; Fray, D., Controlled electrochemical doping of graphene-based 3D nanoarchitecture electrodes for supercapacitors and capacitive deionisation. *Nanoscale* **2017,** *9* (38), 14548-14557.

195. Dianbudiyanto, W.; Liu, S.-H., Outstanding performance of capacitive deionization by a hierarchically porous 3D architectural graphene. *Desalination* **2019,** *468*, 114069.

196. Tian, H.; Wang, N.; Xu, F.; Zhang, P.; Hou, D.; Mai, Y.; Feng, X., Nitrogen-doped carbon nanosheets and nanoflowers with holey mesopores for efficient oxygen reduction catalysis. *Journal of Materials Chemistry A* **2018,** *6* (22), 10354-10360.

197. Gao, H.; Li, J.; Lian, K., Alkaline quaternary ammonium hydroxides and their polymer electrolytes for electrochemical capacitors. *RSC Advances* **2014,** *4* (41), 21332-21339.

198. Xu, X.; Sun, Z.; Chua, D. H.; Pan, L., Novel nitrogen doped graphene sponge with ultrahigh capacitive deionization performance. *Scientific reports* **2015,** *5*, 1-19.

199. Niu, W.; Yang, Y., Graphitic Carbon Nitride for Electrochemical Energy Conversion and Storage. *ACS Energy Letters* **2018,** *3* (11), 2796-2815.

200. Niu, W.; Yang, Y., Amorphous MOF Introduced N-Doped Graphene: An Efficient and Versatile Electrocatalyst for Zinc–Air Battery and Water Splitting. *ACS Applied Energy Materials* **2018,** *1* (6), 2440-2445.

201. Lei, W.; Guo, J.; Wu, Z.; Xuan, C.; Xiao, W.; Wang, D., Highly nitrogen and sulfur dual-doped carbon microspheres for supercapacitors. *Science Bulletin* **2017,** *62* (14), 1011-1017.

202. Lei, W.; Han, L.; Xuan, C.; Lin, R.; Liu, H.; Xin, H. L.; Wang, D., Nitrogen-doped carbon nanofibers derived from polypyrrole coated bacterial cellulose as high-performance electrode materials for supercapacitors and Li-ion batteries. *Electrochimica Acta* **2016,** *210*, 130-137.

203. Cao, X.; Tian, G.; Chen, Y.; Zhou, J.; Zhou, W.; Tian, C.; Fu, H., Hierarchical composites of TiO 2 nanowire arrays on reduced graphene oxide nanosheets with enhanced photocatalytic hydrogen evolution performance. *Journal of Materials Chemistry A* **2014,** *2* (12), 4366-4374.

204. Kim, J.; Khoh, W.-H.; Wee, B.-H.; Hong, J.-D., Fabrication of flexible reduced graphene oxide–TiO 2 freestanding films for supercapacitor application. *Rsc Advances* **2015,** *5* (13), 9904-9911.

205. Ting, Y.-J. B.; Lian, K.; Kherani, N., Fabrication of titanium nitride and molybdenum nitride for supercapacitor electrode application. *ECS Transactions* **2011,** *35* (32), 133-139.

206. Chen, L.; Dai, H.; Zhou, Y.; Hu, Y.; Yu, T.; Liu, J.; Zou, Z., Porous, single crystalline titanium nitride nanoplates grown on carbon fibers: excellent counter electrodes for low-cost, high performance, fiber-shaped dye-sensitized solar cells. *Chemical Communications* **2014,** *50* (92), 14321-14324.

207. Wu, Y.; Jiang, G.; Liu, G.; Lui, G.; Cano, Z.; Li, Q.; Zhang, Z.; Yu, A.; zhang, j.; Chen, Z., 3D Ordered Hierarchical Porous Non-Carbon Electrode for Highly Effective and Efficient Capacitive Deionization. *Journal of Material Chemistry A* **2019,** *7*, 15633-15639.

208. Sung, S.; Park, S.; Lee, W.-J.; Son, J.; Kim, C.-H.; Kim, Y.; Noh, D. Y.; Yoon, M.-H., Low-voltage flexible organic electronics based on high-performance sol–gel titanium dioxide dielectric. *ACS applied materials & interfaces* **2015,** *7* (14), 7456-7461.

209. Wiranwetchayan, O.; Promnopas, S.; Thongtem, T.; Chaipanich, A.; Thongtem, S., Effect of alcohol solvents on TiO2 films prepared by sol–gel method. *Surface and Coatings Technology* **2017,** *326*, 310-315.

210. Anwar, A. W.; Majeed, A.; Iqbal, N.; Ullah, W.; Shuaib, A.; Ilyas, U.; Bibi, F.; Rafique, H. M., Specific Capacitance and Cyclic Stability of Graphene Based Metal/Metal Oxide Nanocomposites: A Review. *Journal of Materials Science & Technology* **2015,** *31* (7), 699-707.

211. Pei, S.; Cheng, H.-M., The reduction of graphene oxide. *Carbon* **2012,** *50* (9), 3210-3228.

212. Lee, C.-L.; Kim, C.; Kim, I.-D., Ultrasmall titanium oxide/titanium oxynitride composite nanoparticle-embedded carbon nanofiber mats as high-capacity and free-standing electrodes for lithium sulfur batteries. *RSC Advances* **2017,** *7* (71), 44804-44808.

213. Ding, M.; Fan, S.; Huang, S.; Pam, M. E.; Guo, L.; Shi, Y.; Yang, H. Y., Tunable Pseudocapacitive Behavior in Metal-Organic Framework Derived TiO2@ Porous Carbon Enabling High-Performance Membrane Capacitive Deionization. *ACS Applied Energy Materials* **2019,** *2* (2), 1812-1822.

214. Guo, D.; Shibuya, R.; Akiba, C.; Saji, S.; Kondo, T.; Nakamura, J., Active sites of nitrogen-doped carbon materials for oxygen reduction reaction clarified using model catalysts. *Science* **2016,** *351* (6271), 361-365.

215. Bharathidasan, P.; Sridhar, S.; Vardhan, P. V.; Sivakkumar, S.; Kim, D.-W.; Devaraj, S., High capacitance and long cycle-life of nitrogen doped reduced graphene oxide. *Journal of Materials Science: Materials in Electronics* **2018,** *29* (9), 7661-7667.

216. Liu, Y.; Chen, T.; Lu, T.; Sun, Z.; Chua, D. H. C.; Pan, L., Nitrogen-doped porous carbon spheres for highly efficient capacitive deionization. *Electrochimica Acta* **2015,** *158*, 403-409.

217. Chen, L.-F.; Zhang, X.-D.; Liang, H.-W.; Kong, M.; Guan, Q.-F.; Chen, P.; Wu, Z.-Y.; Yu, S.-H., Synthesis of nitrogen-doped porous carbon nanofibers as an efficient electrode material for supercapacitors. *ACS nano* **2012,** *6* (8), 7092-7102.

218. Xiong, W.; Liu, M.; Gan, L.; Lv, Y.; Xu, Z.; Hao, Z.; Chen, L., Preparation of nitrogen-doped macro-/mesoporous carbon foams as electrode material for supercapacitors. *Colloids and Surfaces A: Physicochemical and Engineering Aspects* **2012,** *411*, 34-39.

219. Wang, K.; Li, L.; Zhang, T.; Liu, Z., Nitrogen-doped graphene for supercapacitor with long-term electrochemical stability. *Energy* **2014,** *70*, 612-617.

220. Yu, B.; Wang, X.; Qian, X.; Xing, W.; Yang, H.; Ma, L.; Lin, Y.; Jiang, S.; Song, L.; Hu, Y., Functionalized graphene oxide/phosphoramide oligomer

hybrids flame retardant prepared via in situ polymerization for improving the fire safety of polypropylene. *Rsc Advances* **2014,** *4* (60), 31782-31794.

221. Lei, Z.; Christov, N.; Zhao, X., Intercalation of mesoporous carbon spheres between reduced graphene oxide sheets for preparing high-rate supercapacitor electrodes. *Energy & Environmental Science* **2011,** *4* (5), 1866-1873.

222. Achour, A.; Chaker, M.; Achour, H.; Arman, A.; Islam, M.; Mardani, M.; Boujtita, M.; Le Brizoual, L.; Djouadi, M.; Brousse, T., Role of nitrogen doping at the surface of titanium nitride thin films towards capacitive charge storage enhancement. *Journal of Power Sources* **2017,** *359*, 349-354.

223. Kusano, D.; Emori, M.; Sakama, H., Influence of electronic structure on visible light photocatalytic activity of nitrogen-doped TiO 2. *RSC Advances* **2017,** *7* (4), 1887-1898.

224. Akple, M. S.; Low, J.; Qin, Z.; Wageh, S.; Al-Ghamdi, A. A.; Yu, J.; Liu, S., Nitrogen-doped TiO2 microsheets with enhanced visible light photocatalytic activity for CO2 reduction. *Chinese Journal of Catalysis* **2015,** *36* (12), 2127-2134.

225. Karade, S.; Dubal, D.; Sankapal, B., *MoS2 ultrathin nanoflakes for high performance supercapacitors: Room temperature chemical bath deposition (CBD)*. 2016; Vol. 6.

226. Xiang, C.; Li, M.; Zhi, M.; Manivannan, A.; Wu, N., Reduced graphene oxide/titanium dioxide composites for supercapacitor electrodes: shape and coupling effects. *Journal of Materials Chemistry* **2012,** *22* (36), 19161-19167.

227. Lazarte, J.; Dipasupil, R.; Pasco, G.; Eusebio, R.; Orbecido, A.; Doong, R.-a.; Bautista-Patacsil, L., Synthesis of reduced graphene oxide/titanium dioxide nanotubes (rGO/TNT) composites as an electrical double layer capacitor. *Nanomaterials* **2018,** *8* (11), 934.

228. Tsay, K.-C.; Zhang, L.; Zhang, J., Effects of electrode layer composition/thickness and electrolyte concentration on both specific capacitance and energy density of supercapacitor. *Electrochimica Acta* **2012,** *60*, 428-436.

229. Achour, A.; Ducros, J.; Porto, R.; Boujtita, M.; Gautron, E.; Le Brizoual, L.; Djouadi, M.; Brousse, T., Hierarchical nanocomposite electrodes based on titanium nitride and carbon nanotubes for micro-supercapacitors. *Nano Energy* **2014,** *7*, 104-113.

230. Inagaki, M.; Toyoda, M.; Soneda, Y.; Morishita, T., Nitrogen-doped carbon materials. *Carbon* **2018,** *132*, 104-140.

231. Thamilselvan, A.; Nesaraj, A.; Noel, M., Review on carbon-based electrode materials for application in capacitive deionization process. *International Journal of Environmental Science and Technology* **2016,** *13* (12), 2961-2976.

232. Li, H.; Ma, Y.; Niu, R., Improved Capacitive Deionization Performance by Coupling TiO 2 Nanoparticles with Carbon Nanotubes. *Separation and Purification Technology* **2016**.

233. Mi, M.; Liu, X.; Kong, W.; Ge, Y.; Dang, W.; Hu, J., Hierarchical composite of N-doped carbon sphere and holey graphene hydrogel for high-performance capacitive deionization. *Desalination* **2019,** *464*, 18-24.

234. Liu, Y.; Chen, T.; Lu, T.; Sun, Z.; Chua, D. H.; Pan, L., Nitrogen-doped porous carbon spheres for highly efficient capacitive deionization. *Electrochimica Acta* **2015,** *158*, 403-409.

235. Daud, Z.; Awang, H.; Latif, A. A. A.; Nasir, N.; Ridzuan, M. B.; Ahmad, Z., Suspended Solid, Color, COD and Oil and Grease Removal from Biodiesel Wastewater by Coagulation and Flocculation Processes. *Procedia - Social and Behavioral Sciences* **2015,** *195*, 2407-2411.

236. Zhang, H.; Zhao, Z.; Xu, X.; Li, L., Study on industrial wastewater treatment using superconducting magnetic separation. *Cryogenics* **2011,** *51* (6), 225-228.

237. Wan, T.-J.; Shen, S.-M.; Siao, S.-H.; Huang, C.-F.; Cheng, C.-Y., Using magnetic seeds to improve the aggregation and precipitation of nanoparticles from backside grinding wastewater. *Water Research* **2011,** *45* (19), 6301-6307.

238. Luo, Y.; Pan, F.; Wei, Y., Preparation and Properties of Four Kinds of Magnetic Flocculants. *Metal Mine* **2014**.

239. Yi-Yan, S. U.; Duan, S. E., Preparation of Fe_3O_4-PAC magnetic flocculants and study of flocculation performance. *Applied Chemical Industry* **2014**.

240. Liu, X., Primary Study on Treatment of Municipal Rainwater Overflow by Magnetic Coagulation. *Industrial Safety & Environmental Protection* **2011**.

241. Zhou, Z.; Shan, A.; Zhao, Y., Synthesis of a Novel Cationic Magnetic Flocculant and its Application. *Industrial Safety & Environmental Protection* **2017**.

242. Zhang, C.; Hou, X.; Lun, X.; Xia, H., Study on the preparation and capabilities of magnetic chitosan flocculant via in-situ precipitation. *Industrial Water Treatment* **2013,** *33* (2), 63-66.

243. Yuan, Y.; Zhan, C.; He, K.; Chen, H.; Yao, W.; Sharifi-Asl, S.; Song, B.; Yang, Z.; Nie, A.; Luo, X., The influence of large cations on the electrochemical properties of tunnel-structured metal oxides. *Nature communications* **2016,** *7*, 13374.

244. Xu, Y.; Lin, Z.; Zhong, X.; Huang, X.; Weiss, N. O.; Huang, Y.; Duan, X., Holey graphene frameworks for highly efficient capacitive energy storage. *Nature communications* **2014,** *5*, 4554.

245. Wang, J.; Polleux, J.; Lim, J.; Dunn, B., Pseudocapacitive contributions to electrochemical energy storage in TiO2 (anatase) nanoparticles. *The Journal of Physical Chemistry C* **2007,** *111* (40), 14925-14931.

246. Valvoda, V.; Černý, R.; Kužel, R.; Musil, J.; Poulek, V., Dependence of microstructure of TiN coatings on their thickness. *Thin Solid Films* **1988,** *158* (2), 225-232.

247. Zhao, S.; Yan, T.; Wang, H.; Chen, G.; Huang, L.; Zhang, J.; Shi, L.; Zhang, D., High capacity and high rate capability of nitrogen-doped porous hollow carbon spheres for capacitive deionization. *Applied Surface Science* **2016,** *369*, 460-469.

248. Wu, T.; Wang, G.; Zhan, F.; Dong, Q.; Ren, Q.; Wang, J.; Qiu, J., Surface-treated carbon electrodes with modified potential of zero charge for capacitive deionization. *Water research* **2016,** *93*, 30-37.

249. Zornitta, R. L.; García-Mateos, F. J.; Lado, J. J.; Rodríguez-Mirasol, J.; Cordero, T.; Hammer, P.; Ruotolo, L. A. M., High-performance activated carbon from polyaniline for capacitive deionization. *Carbon* **2017,** *123*, 318-333.

250. Liu, P.; Wang, H.; Yan, T.; Zhang, J.; Shi, L.; Zhang, D., Grafting sulfonic and amine functional groups on 3D graphene for improved capacitive deionization. *Journal of Materials Chemistry A* **2016,** *4* (14), 5303-5313.

251. Yan, T.; Liu, J.; Lei, H.; Shi, L.; An, Z.; Park, H. S.; Zhang, D., Capacitive deionization of saline water using sandwich-like nitrogen-doped graphene composites via a self-assembling strategy. *Environmental Science: Nano* **2018,** *5* (11), 2722-2730.

252. Wu, T.; Wang, G.; Dong, Q.; Zhan, F.; Zhang, X.; Li, S.; Qiao, H.; Qiu, J., Starch Derived Porous Carbon Nanosheets for High-Performance Photovoltaic Capacitive Deionization. *Environmental Science & Technology* **2017,** *51* (16), 9244-9251.

253. Cao, J.; Wang, Y.; Wang, L.; Yu, F.; Ma, J., Na3V2(PO4)3@C as Faradaic Electrodes in Capacitive Deionization for High-Performance Desalination. *Nano Letters* **2019,** *19* (2), 823-828.

254. Lee, J.; Kim, S.; Kim, C.; Yoon, J., Hybrid capacitive deionization to enhance the desalination performance of capacitive techniques. *Energy & Environmental Science* **2014,** *7* (11), 3683-3689.

255. Toth, L., *Transition metal carbides and nitrides*. Elsevier: 2014.

256. Biesinger, M. C.; Payne, B. P.; Hart, B. R.; Grosvenor, A. P.; McIntryre, N. S.; Lau, L. W.; Smart, R. S. In *Quantitative chemical state XPS analysis of first row transition metals, oxides and hydroxides*, Journal of Physics: Conference Series, IOP Publishing: 2008; p 012025.

257. Biesinger, M. C.; Payne, B. P.; Grosvenor, A. P.; Lau, L. W.; Gerson, A. R.; Smart, R. S. C., Resolving surface chemical states in XPS analysis of first row transition metals, oxides and hydroxides: Cr, Mn, Fe, Co and Ni. *Applied Surface Science* **2011,** *257* (7), 2717-2730.